UiT The Arctic University of Norway

Faculty of Science and Technology

Department of Physics and Technology

Predicting the Auroral Oval Boundaries by Means of Polar Operational Environmental Satellite Particle Precipitation Data

Mikkel J. Breedveld

Master's Thesis in Space Physics, FYS-3931, June 2020

UNIS

The University Centre in Svalbard

Predicting the Auroral Oval Boundaries by Means of Polar Operational Environmental Satellite Particle Precipitation Data

Mikkel J. Breedveld

FYS-3931 Master's Thesis in Space Physics

Department of Physics and Technology
Faculty of Science and Technology
UiT The Arctic University of Norway

In cooperation with

Department of Arctic Geophysics
The University Centre in Svalbard

June 2020

Abstract

New empirical K_p-based models for the equatorward and poleward boundaries of the auroral oval in the Northern and Southern Hemispheres were developed, with the purpose of reviewing the auroral ovals predicted by well-established Feldstein auroral oval model. The new models were derived from particle and energy flux measurements from six low-altitude (800 – 900 km) POES/MetOp satellites. All six satellites (NOAA-15 through NOAA-19 and MetOp-A) carried identical TED and MEPED instruments, measuring the flux of precipitating electrons and protons over different energy ranges. The data was collected throughout 2012, with two or more satellites being operational simultaneously for most of the year. The auroral oval boundary detection events for four different particle species and energy range combinations were used as the basis for the auroral oval models: electrons < 20 keV (TED), protons < 20 keV (TED), electrons > 30 keV (MEPED) and protons 30 – 80 keV (MEPED).

For each of these four particle types, the equatorward and poleward boundaries of the auroral oval were defined. The location of the precipitation zones of the four particles types corresponded well with the general precipitation regions described in the literature. For most K_p values, the precipitation zones were comparable in the Northern and Southern Hemispheres. However, for electrons with energies < 20 keV (the visible auroral oval), a consistent asymmetry between the hemispheres was found on the dayside. Furthermore, using MEPED measurements, the location of the electron and proton isotropic boundaries were found to be located around the poleward boundary and just poleward of the equatorward boundary, respectively.

Three different fitting methods were used to express the detected auroral oval boundaries as a function of K_p: a fourth-order polynomial fit, a direct least-squares ellipse fit and a second-order Fourier series fit. All three methods had major caveats and could only provide rough estimates for the auroral oval boundary locations. However, the Fourier series fit was chosen as the most suitable method, since it incorporated the observed asymmetry between the hemispheres for the TED electron boundaries.

The models based on the three methods were compared to the Feldstein model,

derived from ground-based optical observations. The poleward boundaries of the new models and the Feldstein model were found to be located within 5° ILAT of each other. The equatorward boundaries could be more than 10° ILAT equatorwards of the Feldstein equatorward boundary. Consequently, the new models estimated much larger auroral ovals than does the Feldstein model. The new models had the advantage of providing more information about the various auroral particle precipitation zones in both hemispheres. However, the models did not provide any indication about the location of the parts of the auroral oval that are visible from the ground. This is important knowledge when incorporating these types of models into aurora forecasting software such as Aurora Forecast 3D. To further elaborate on these models, it will be necessary to take into account the difference in altitude between the spacecraft orbits and the visible aurora, in order to accurately estimate the region where aurora may be observed from the ground.

Preface

This master's thesis came about after a visit to Svalbard in June 2018. While visiting my father who was in Longyearbyen at the time, I happened to come across a copy of the local newspaper Svalbardposten (No. 15, April 19, 2018, Volume 71). On the very last page was an interview with Fred Sigernes, an optics and space physics professor at the Department of Arctic Geophysics at UNIS. At this point, I did not know who he was or what he did, nor did I know any of the other faculty at the Arctic Geophysics department. But after reading the half-page article it became clear to me that he seemed to know a thing or two about space physics and the aurora. After all, he was the head of the Kjell Henriksen Observatory. I was one and a half years away from writing my master's thesis in space physics, but my father, knowing that I was looking for a topic to write my thesis on, encouraged me to reach out to Fred. In the spring of 2019 I gathered my courage and sent him an email, asking if he was looking for any master students within the field of auroral science. It didn't take long before Fred got back to me, saying he indeed had a project I could work on. By the time the fall semester came around in August 2019, Fred had recruited two more supervisors to take part in the project: Finn Søraas from the Birkeland Centre for Space Science (BCSS) at the University of Bergen and Magnar G. Johnsen from Tromsø Geophysical Observatory (TGO) at the UiT. The rest, as they say, is history.

There are many people I would like to thank for their contributions to this master's thesis, but first and foremost, I would like to thank each of my three supervisors for all their patience and efforts to help me complete my thesis over the past six months. First off, I would like to thank Fred for organizing the research project from the beginning and allowing me to be apart of it. Finn deserves a lot of credit for guiding me though the satellite data analysis, for answering any question I might have and for being the POES and MATLAB guru he truly is. Magnar deserves special recognition for being my principal supervisor at UiT, both for my project paper and my master's thesis. I am very grateful that he took on the responsibility of sorting out all the paperwork and formalities associated with writing a master's thesis, and for recommending me to attend the AGF-345/845 Polar Magnetospheric Substorms course at UNIS as a preparation for my master's thesis. I would also like to thank Karl M.

Laundal from BCSS for paying me and Fred a visit at UNIS together with Finn, and for the input he provided on magnetic coordinate systems during their stay in Longyearbyen. I am very grateful for all your comments, feedback and encouragement along the way.

The list of people to thank goes on, but there are a few more that deserve to be recognized. I would like to thank the entire AGF-345/845 class of 2019 for giving me an introduction to UNIS student life and for making it clear to me that I simply had to return to Svalbard to write my thesis at UNIS. Special thanks goes out to all the people I have lived with at the 2nd floor of the Sjøskrenten student accommodation in Longyearbyen, especially Christina Hess, Laura Scholtz, Will Hartz, Veerle van Winden, Karlotta Kürzel and Craig Hammock. During the last two months of writing my thesis, this crazy bunch ensured that I was happy, well fed and that I did not eat Drytech Real Turmat for supper every night (that being said, I probably consumed about the same amount of Drytech in the last month of thesis writing as in my entire prior life combined). I could not possibly tell how many times I have mooched food somebody else had prepared, but it was often enough that the act of eating a fellow student's food became synonymous with my name. I appreciate you all, particularly your cooking skills. I want to extend special gratitude to fellow "Substorminators" Daria Paul and Alexander Dutoy, who helped me proof read my thesis and came with suggestions on how to improve my writing. Your feedback throughout the last few days before submission was invaluable. Thank you.

I must not forget to thank my family either. I would like to thank my brother, for setting a great example and for showing me what a proper master's thesis should look like. My parents, deserve a lot of recognition for keeping me motivated throughout the writing process. At times when motivation was hard to find, my mother and father always had some encouraging words and advice to share. Finally, I want to thank my father for handing me that April 19, 2018 copy of Svalbardposten.

Contents

List of Figures

List of Tables

1 Introduction

1.1 Motivation

Auroral forecasting concerns itself with predicting when and where on the Earth auroras will occur. One of the first to systematically map the occurrence of auroras, Fritz (1881) defined the geographic areas where auroras were most likely to appear. In the late 19th Century, using auroral observations in the Northern Hemisphere spanning 172 years, from 1700 to 1872, Fritz developed a map detailing where auroras were expected to occur with a given frequency (so-called isochasms) (Vestine, 1944). Known as the auroral zone, this statistically defined region consists of two bands between approximately 65° and 75° geomagnetic latitude. During the International Geophysical Year (IGY, 1957-58), following extensive imaging in the auroral zones using all-sky cameras, Feldstein (1964) suggested that auroras occur in ovals roughly centred at the geomagnetic poles in the Northern and Southern Hemispheres (see Figure 1.1). Feldstein's studies also revealed that the auroral oval is dynamic; its shape and size is subject to diurnal, annual and long-term variations in geomagnetic activity. Throughout the past 60 years, significant progress has been made in the development of models for predicting the morphology of the auroral oval. The advancement of auroral oval prediction techniques has benefited tremendously from the technological developments initiated by the beginning of the space age (coinciding with the IGY).

The auroral ovals may be referred to as the regions in the ionosphere receiving the majority of the particle precipitation (Xiong & Lühr, 2014). Centred in the

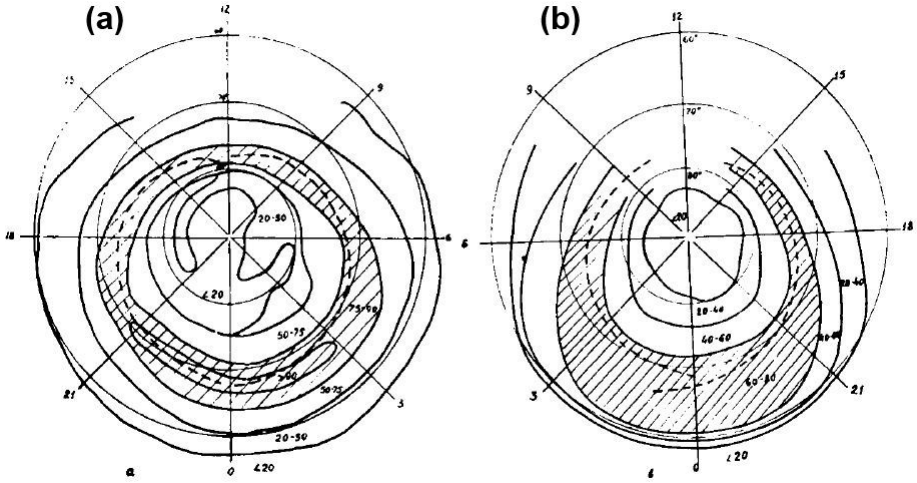

Figure 1.1: The auroral ovals in the Northern (a) and Southern (b) hemispheres, derived from all-sky camera surveys during the International Geophysical Year (1957-1958). The numbers within the ovals indicate the frequency (in percent) of observed aurora at zenith. From Feldstein (1964).

vicinity of the geomagnetic poles and taking the shape of continuous bands with radii of roughly 3500 km, the auroral ovals are essentially a mapping of the magnetosphere into the Earth's atmosphere, i.e. the regions where aurora may be observed at any given instant in time (Weiss, Reiff, Hilmer, Winningham, & Lu, 1992). The size of the auroral oval is mainly controlled by the north-south component of the interplanetary magnetic field (IMF) (Holzworth & Meng, 1975). The poleward boundary of the auroral oval tends to correspond to the polar cap, inside which Earth's magnetic field lines are open and merged with the IMF (Xiong & Lühr, 2014). Consequently, the open-closed field line boundary defines the approximate location of the poleward boundary of the auroral oval (Johnsen, 2013). Processes in the magnetosphere are in turn related to the activity of the Sun via the solar wind, meaning the size of the auroral oval provides a proxy of the solar activity (Wagner & Neuhäuser, 2019).

The aurora has been an important factor for space weather predictions and provides substantial information about the conditions in the upper atmosphere. It may be considered to be the only visible manifestation of space weather (Carbary, 2005). While the geomagnetic activity may be used to predict the size and location of the auroral oval, the reverse process may be applied to determine solar activity in the past. A set of historical observations of the aurora may be linked to a parameter representing the magnetic activity, which in turn provides information about the solar activity at the time of the observations. Moreover, observations of the auroral ovals may be used to find the past

locations of the geomagnetic poles (Wagner & Neuhäuser, 2019). Repeated observations may give an indication of the drift of the geomagnetic poles. For these purposes, it becomes evident that it is useful to derive a model to predict the location and size of the auroral ovals. A common method used to develop models for the auroral ovals is to determine the boundaries of the oval based on empirical observations and correlate these observations with a magnetic activity index, representing the level of geomagnetic activity at the time the observations were made (Carbary, 2005). By implementing such a model, it is possible to estimate the location of the equatorward and poleward boundaries in the past, present or future, given that the level of magnetospheric disturbance is known.

Particularly in the Northern Hemisphere, an entirely different incentive for developing auroral oval models comes in the shape of auroral tourism. This fairly new industry has seen rapid growth over the past decade. In Alaska alone, 320,000 tourists visited during the winter months of 2018. The majority of these tourists came to see the northern lights (Williams, 2019). Having a reliable auroral forecasting service for the expected conditions at a particular geographic location is a valuable asset for aurora guiding firms and tourists alike. Access to aurora forecasting application software, such as Aurora Forecast 3D (Sigernes, 2016), make auroral forecasts easy to access and interpret by the user.

Incentives to better understand the morphology of the auroral ovals also extend beyond practical and commercial applications to the purely scientific. The auroras in the two hemispheres are often assumed to be mirror images of each other, where charged particles are evenly distributed among the two hemispheres (Laundal & Østgaard, 2009). The first comparisons between the auroral ovals in the Northern and Southern Hemispheres revealed a high degree of conjugacy, particularly during quiet geomagnetic conditions (Akasofu, 1978). However, Laundal and Østgaard (2009), using more recent satellite observations, reported significant asymmetries in the auroral pattern between the Northern and Southern Hemispheres. Developing separate models for auroral ovals in the Northern and Southern Hemispheres provides a step on the way to better understand these asymmetries.

Beyond the Earth, observations of auroras on other planets in the Solar System are an important indicator for the existence of a magnetic field and an atmosphere. In particular, the spectrum of the aurora may provide significant information about the atmospheric composition of a planet's atmosphere. For instance, if the auroral spectrum from a given planet contains the 557.7 nm "green line", the atmosphere is likely to contain oxygen (since the 557.7 nm emission is due to the transition of atomic oxygen from the ^1S state to the ^1D state (Brekke, 2013)). This in turn is an important prerequisite for the existence

of both plant and animal life. Hence, auroral science may play a role in the search for extraterrestrial life (Akasofu, 1999).

While the likes of Fritz (1881), Vestine (1944) and Feldstein (1964) laid the foundation of modern research into the morphology of the auroral oval, the advent of the space age and Earth-observing satellites provided unparalleled opportunities for auroral research. Not hampered by varying observational conditions (cloudy or inclement weather, midnight sun, etc.), satellites have the ability to make more extensive and accurate observations of the auroral ovals. Consequently, most auroral models developed over the past decades are based on satellite observations. Auroral oval boundary observations by satellite may be divided into two main regimes: the first is particle measurements of precipitating energetic particles causing the aurora (see e.g. Newell, Sotirelis, and Wing (2009)), and the second is direct imaging of the auroral oval (see e.g. Holzworth and Meng (1975), Zhang and Paxton (2008) and Wagner and Neuhäuser (2019)). The first approach has the advantage of providing well-defined oval boundaries, but only along the satellite orbit. The second regime provides a global view of the auroral oval at any one instant in time, but comes at the expense of lower spatial resolution and less well-defined boundaries (Carbary, 2005). Alternative space-based methods include the use of magnetometers on spacecraft (see e.g. the CH-Aurora-2014 model by Xiong and Lühr (2014)).

Although various auroral oval models have been developed over the past decades, most models have limitations due to the fact that underlying assumptions and simplifications need to be made in order to effectively predict the size and location of the auroral ovals. For instance, the Feldstein model does not distinguish between the auroral ovals in the Northern and Southern Hemispheres (Feldstein, 1964). By continuing to develop new auroral oval models based on different data and magnetic activity indices, progress is made in establishing more accurate and reliable auroral forecasts. This thesis aims to add a small piece to this puzzle.

1.2 Objectives

The objective of this master's thesis is to develop a simple auroral oval model consisting of separate approximations for the equatorward and poleward auroral oval boundaries in the Northern and Southern Hemispheres. The model will be based on empirical data obtained throughout 2012, from particle detectors carried on board five Polar-orbiting Operational Environmental Satellites (POES) operated by the National Oceanic and Atmospheric Administration (NOAA), as well as the MetOp-A satellite, operated by the European Organi-

sation for the Exploitation of Meteorological Satellites (EUMETSAT) (NOAA, 2020). The detectors used in this work measure the flux of precipitating electrons and protons over two different energy ranges per particle species. The detected boundaries will be correlated to the K_p index, a common measure of the level of geomagnetic disturbance (Thomsen, 2004). Once the correlation coefficients have been determined, the equator and poleward boundaries of the auroral oval may be determined for any arbitrary K_p value.

Four separate auroral ovals will be developed within each hemisphere: electrons with energies less than 20 keV, electrons with energies greater than 30 keV, protons with energies less than 20 keV and protons with energies between 30 keV and 80 keV. To describe the oval boundaries, three different functions will be fitted to the boundary detection events: (1) a polynomial fit, (2) an ellipse fit and (3) a Fourier series fit. The resulting auroral oval models based on these three methods will be evaluated with respect to the Feldstein auroral oval model. Moreover, the boundary detections in the Northern and Southern hemispheres will be compared to each other for different K_p values to investigate for any apparent asymmetries in the morphology of the auroral ovals between the hemispheres. Lastly, the location of the isotropic boundary (IB) will be determined in both hemispheres and compared to the location of the equatorward auroral oval boundaries in both hemispheres.

1.3 Thesis Structure

Chapter 2 provides a general introduction to central geophysical principles relevant for the development of auroral oval models, including the magnetic coordinate system in which the satellite data is expressed, general characteristics of auroral particles and the physical principles underlying the existence of the isotropic boundary. Subsequently, the POES and MetOp satellite programs and the six satellites used to conduct the observations are presented. The two particle detector instruments carried on board each of the satellites are described in detail. Furthermore, common magnetic activity indices are introduced, with particular emphasis on the K_p index. The Feldstein auroral oval model is presented, with emphasis on the equations used to determine the boundaries as a function of K_p. The general features of the Aurora Forecast 3D software application are described, and a visualization of the Feldstein auroral oval as it appears in the application is provided. The methodology used to create the three auroral oval models is detailed in Chapter 3. An overview of the data set used to develop the models is provided, including the data coverage of each individual satellite throughout 2012. The preliminary data processing, including binning of the data into fixed K_p and MLT intervals is described, followed by an explanation of the equations involved in each of

the three fitting methods. The polynomial fit, ellipse fit and Fourier series fit methods are all presented in turn. The method for calculating the location of the isotropic boundary is presented at the end of the chapter.

In Chapter 4 a step-by-step procedure to obtain the auroral oval boundaries for a given K_p value is provided for each of the three models. Examples of the resulting ovals for selected K_p values in both the Northern and Southern Hemispheres are presented. The estimated location of the isotropic boundary is shown relative to the equatorward and boundaries boundaries in both hemispheres. The three auroral oval models are evaluated in Chapter 5, both with respect to each other and to the Feldstein model. The models are assessed on their ability to encompass the features observed in the equatorward and poleward boundary detection data. In addition, the three models are evaluated based on their relevance for potential future implementation and improvement of the Aurora Forecast 3D software. Furthermore, any apparent differences between the auroral ovals in the Northern and Southern Hemispheres for different levels of magnetic activity are described. The location of the isotropic boundary is discussed with respect to its location suggested by the literature. Throughout the discussion particular emphasis will be but on the auroral ovals caused by electrons with energies less than 20 keV, as these particles are most closely associated with the visible auroral oval. At the end of the chapter, suggestions for future work and further development of the model are provided. Chapter 6 summarizes the most important results and provides some concluding remarks.

2

Background

2.1 Magnetic Coordinate Systems

Phenomena in the near-Earth space environment, including the aurora, are highly affected by the Earth's magnetic field and disturbances within. The sphere of influence of Earth's magnetic field stretches to about 15 Earth radii ($1R_E \approx 6,371$ km) on the dayside hemisphere (the side of the Earth facing the Sun) and up to several hundred Earth radii on the nightside. Since the charged particles in space plasma are controlled by the magnetic field, it is useful to describe such phenomena in a magnetic coordinate system, as opposed to, for instance, a geographic coordinate system. However, there are many different magnetic coordinate systems, each of which is useful to describe particular phenomena in the magnetosphere and the ionosphere. Magnetic coordinate systems are based on the spherical harmonic expansion coefficients of the International Geomagnetic Reference Field (IGRF), and in some cases, the position of the Sun. The nature of the magnetic coordinate systems may be either orthogonal or non-orthogonal. Which coordinate system is most useful to use depends on how far away from the Earth a phenomena of interest occurs (Laundal & Richmond, 2016).

At ionospheric altitudes (approximately 60 – 800 km) (Brekke, 2013) the centred dipole (CD) coordinate system may be used. This is one of the most commonly used magnetic coordinate systems, and is often referred to by various names, including the geomagnetic, the geomagnetic dipole and the magnetic coordinate systems. The CD coordinate system is an orthogonal magnetic

coordinate system, involving a translation of the poles from the rotational axis to the the dipole axis of the Earth. Since auroras occur at altitudes around 100 km, the CD coordinate system is applicable for auroral phenomena (Laundal & Richmond, 2016).

To perform the translation from the rotational axis to the dipole axis, the IGRF dipole model may be used to. The IGRF is a mathematical model that describes the Earth's magnetic field on a large scale, by means of a 13^{th} order spherical harmonics function. The model has been developed by the International Association of Geomagnetism and Aeronomy (IAGA) since 1965 and is updated every five years. The IGRF must be updated regularly in order to take into account continuous changes in the Eath's magnetic field caused by fluctuations in the Earth's outer core. The first generation IGRF model (IGRF-1) was valid for epoch 1955 to 1975, whereas the 12^{th} generation (IGRF-12) was valid from epoch 1900 to 2020 (Thébault et al., 2015). The current IGRF generation (IGRF-13) was released by IAGA in December 2019 (Alken, 2019).

The IGRF model describes the Earth's main magnetic field $\boldsymbol{B}$ on and above the Earth's surface (considering only internal sources of magnetism) in terms of the scalar potential V, where $\boldsymbol{B}(r, \theta, \phi, t) = -\nabla V$. The scalar potential V is a function of the radial distance r from the centre of the Earth, the geocentric co-latitude θ, the eastward longitude ϕ and time t. The following finite series expansion approximates the potential (Thébault et al., 2015):

$$V(r, \theta, \phi, t) = a \sum_{n=1}^{N} \sum_{m=0}^{n} \left(\frac{a}{r}\right)^{n+1} \left[g_n^m(t) \cos(m\phi) + h_n^m(t) \sin(m\phi)\right] P_n^m(\cos\theta) \tag{2.1}$$

where $a = 6,371.2$ is the geomagnetic conventional mean spherical radius of the Earth. The degree of truncation $N = 13$ (Alken, 2019). The term $P_n^m(\cos\theta)$ represents the Schmidt quasi-normalized associated Legendre functions of degree n and order m, while g_n^m and h_n^m are the time dependent Gauss coefficients of the internal magnetic field. It is these coefficients that are updated every five years (Laundal & Richmond, 2016). Describing the dipole magnetic field requires the first three Gauss coefficients: g_1^0, g_1^1 and h_1^1. The magnetic moment unit vector of the dipole field $\hat{\boldsymbol{m}}$ is given by

$$\hat{\boldsymbol{m}} = -\frac{1}{B_0} \begin{bmatrix} g_1^1 \\ h_1^1 \\ g_1^0 \end{bmatrix} \tag{2.2}$$

where the reference magnetic field B_0 may be expressed as:

$$B_0 = \sqrt{\left(g_1^0\right)^2 + \left(g_1^1\right)^2 + \left(h_1^1\right)^2} \tag{2.3}$$

The magnetic moment is anti-parallel to the dipole axis, hence the negative sign in Equation 2.2. This is due to the convention of letting the geomagnetic dipole be positive northwards, despite the fact that dipole axis of the Earth's magnetic field points southwards (i.e. the North Pole of the dipole is geographically in the Southern Hemisphere).

The Cartesian base vectors for the CD coordinate system are as follows:

$$\begin{aligned} \hat{\boldsymbol{z}}_{cd} &= \hat{\boldsymbol{m}} \\ \hat{\boldsymbol{y}}_{cd} &= \frac{\hat{\boldsymbol{z}}_{geo} \times \hat{\boldsymbol{z}}_{cd}}{\|\hat{\boldsymbol{z}}_{geo} \times \hat{\boldsymbol{z}}_{cd}\|} \\ \hat{\boldsymbol{x}}_{cd} &= \hat{\boldsymbol{y}}_{cd} \times \hat{\boldsymbol{z}}_{cd} \end{aligned} \tag{2.4}$$

The z axis is aligned with the dipole axis, pointing along $\hat{\boldsymbol{m}}$. The y axis is perpendicular to the plane spanned by the Earth's rotation axis and the dipole axis. The unit vector $\hat{\boldsymbol{z}}_{geo}$ is aligned with the Earth's rotation axis. The right-handed coordinate system is completed by the x axis (Laundal & Richmond, 2016).

Like many other magnetic coordinate systems, CD coordinates are defined to be fixed relative to the Earth. In space physics, however, it is often useful to express models and data with respect to the position of the Sun. A common way to do this is to express magnetic longitude and latitude in terms of magnetic local time (MLT) and magnetic latitude (MLAT), which are fixed with respect to the Sun. There are several definitions of MLT, the principle idea being that the Earth, centred at the magnetic poles, is divided into a 24-hour clock where 1 hour corresponds to 15° magnetic longitude. Midnight (MLT 00) is at the magnetic prime meridian, counting positive towards the east. MLT 12 represents the subsolar point, i.e. the point at which the Sun would be directly overhead. This means that the MLT-MLAT coordinate system will rotate with respect to the surface of the Earth. The rate at which the subsolar point crosses the magnetic meridians determines the rotation rate of the MLT-MLAT system. The rotation rate may be either constant of varying, depending on the magnetic coordinate system and the spacing of the meridians for the coordinate system in question (Laundal & Richmond, 2016).

Another definition of MLT is given by Equation 2.5, where ϕ is the magnetic

longitude of a given point, Φ_N is the geographic longitude of the CD North Pole, and UT is universal time in hours. However, this particular definition does not yield MLT 12 for the subsolar point (Baker & Wing, 1989).

$$MLT = UT + \frac{\phi + \Phi_N}{15} \tag{2.5}$$

An alternative definition is

$$MLT = \frac{\phi + \phi_{cds}}{15} + 12 \tag{2.6}$$

where ϕ_{cds} is the longitude of the subsolar point in CD coordinates. The magnetic longitude ϕ of the point in question can be in CD coordinates or in a number of other magnetic coordinate systems (Laundal & Richmond, 2016).

O'Brien, Laughlin, Allen, and Frank (1962) introduced an alternative to magnetic latitude, referred to as the invariant latitude Λ (ILAT), which is particularly useful for studying trapped particles in the inner magnetosphere.

$$\Lambda = \cos^{-1}\left(\sqrt{\frac{1}{L}}\right) \tag{2.7}$$

The invariant latitude essentially describes where a given magnetic field line touches the surface of the Earth. It is based upon the L parameter, which is constant along a given magnetic field line. The L parameter is defined in such a way that in a perfect dipole field, it would correspond to the equatorial radius of the field line in Earth radii. L is a function of the magnetic field strength B and the longitudinal adiabatic invariant (or integral invariant) I (McIlwain, 1961). In this thesis, the detected auroral oval boundaries and the models that are derived fro those boundaries are expressed in the MLT-ILAT coordinate system.

2.2 Characteristics of the Auroral Ovals

The auroras that are visible in the night sky are caused by the emission of radiation from atoms and molecules in the atmosphere (predominantly atomic

oxygen and nitrogen), that are excited by precipitating energetic particles (electrons and ions/protons). The precipitating auroral particles collide with the atmospheric constituents in the upper polar atmosphere. During the collision, the kinetic energy of the precipitating particles is partly converted into energy stored in chemically excited states of the atmospheric atoms and molecules. As the excited states relax, the stored energy is emitted in the form of radiation, the wavelength of which is determined by the energy transition in the excitation process. Depending on the atom or molecules, several different excitation transitions are possible. Consequently, the emission spectrum of the aurora spans a wide range of spectral lines, from infrared to ultraviolet wavelengths. The brightest visible auroral emission is the 557.7 nm "green line", caused by the transition of an electron in atomic oxygen from the ^{1}S excited state to the ^{1}D state (Kivelson & Russell, 1995). The strongest auroral emissions occur at an altitude of approximately 110 km (Brekke, 2013).

The population of auroral particles consists primarily of electrons and ions (protons) with energies from less than 100 eV to a few 100 keV. The sources of these particles are in the plasma sheet of the magnetic tail and in the polar cusp region of the magnetosphere (see Figure 2.1). Near the Earth, the particles that precipitate into the atmosphere are found polewards of 55° MLAT. The visible aurora is caused by medium-energy particles (approximately $0.5 - 20$ keV), according to Kivelson and Russell (1995). Brekke (2013) defines the majority of visible aurora to be caused by electrons with energies < 21 keV. These particles are located on a circle shifted towards the midnight sector and away from the Sun. The dayside aurora in this circle is associated with low-energy electrons and protons (energies < 1 keV), that are channelled down to the upper atmosphere in the cusp region without significant acceleration. The dayside auroral particles originate from the magnetosheath (the area between the magntopause and the bow shock caused by the solar wind) and precipitate into the polar atmosphere around 78° MLAT. Due to this asymmetry in the in the location of auroras between the nightside and dayside, this region is known as the auroral oval (Kivelson & Russell, 1995).

Figures 2.2 2.3 provide an simplified overview of the precipitation zones of particles with various energies. The auroral oval is represented the region with diagonal lines in Figure 2.2. The most energetic particles are located on a circle of constant latitude around the magnetic pole, equatorwards of the main auroral oval (Kivelson & Russell, 1995), with highly energetic electrons (energies > 40 keV) concentrated on the morning side and protons with energies > 4 keV located on the evening side (Brekke, 2013).

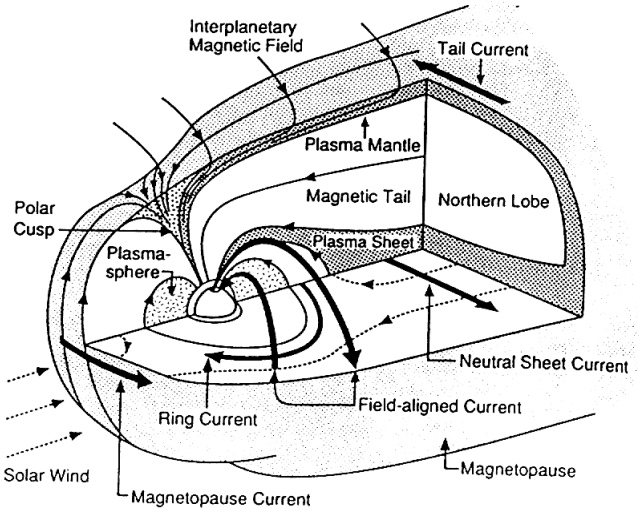

Figure 2.1: Three-dimensional illustration of the main magnetic fields, currents and plasma regions in the Magnetosphere. Auroral particles originate from the plasma sheet in the magnetic tail. From Kivelson and Russell (1995).

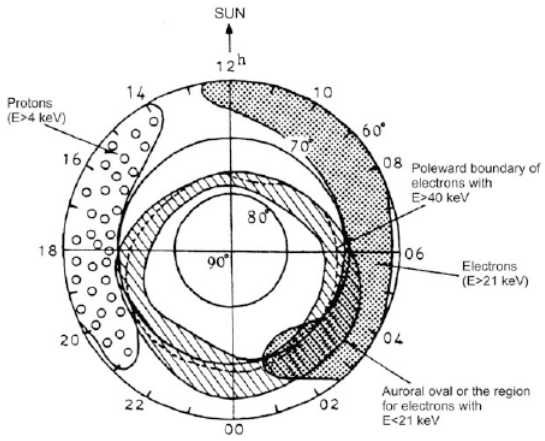

Figure 2.2: Generalized overview of the precipitation zones of various auroral particles at high latitudes in a MLT coordinate system. The region with diagonal stripes, associated with electrons with energies $E < 21\,\text{keV}$, represents the visible auroral oval. The dashed line indicates the poleward boundary of trapped electrons with $E > 40\,\text{keV}$. A proton precipitation zone is located on the evening side, and a highly energetic election precipitation zone is found on the morning side. Both of these regions are equatorward of the main auroral oval. From Tohmatsu (1990).

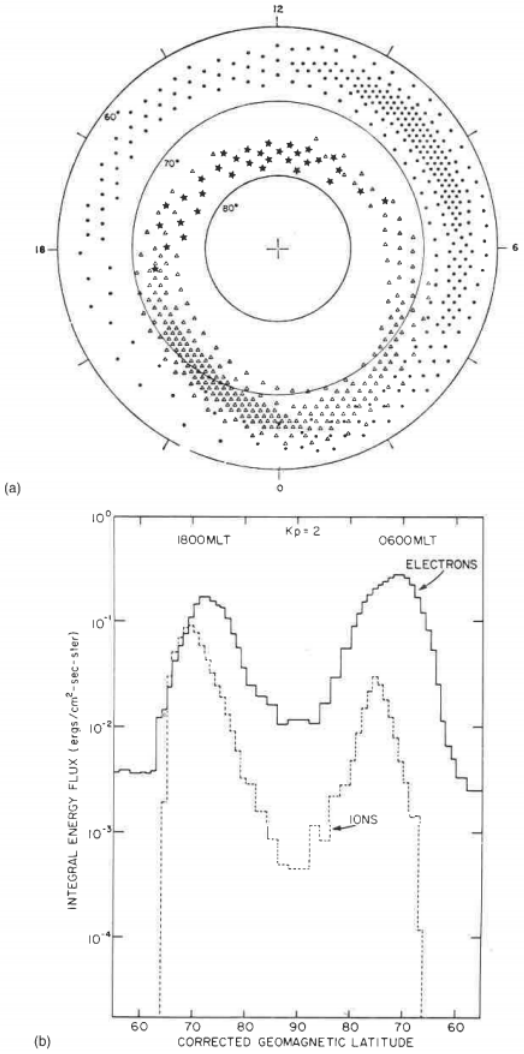

Figure 2.3: (a) A highly idealized overview of the precipitation zones of various auroral particles in a MLT coordinate system. The triangles represent the medium-energy (0.5 – 20 keV) particle precipitation associated with the main auroral oval, the dots represent the high-energy (> 20 keV) precipitation, while the stars around noon MLT indicate the low-energy (< 1 keV) precipitation in the cusp region. The density of the symbols is an indication of the flux. From Hartz (1971). (b) Integrated enegy flux of elections and ions in the dawn-dusk MLT plane. From Kivelson and Russell (1995).

While auroras may take on various shapes and structures, it is useful to distinguish between discrete aurora and diffuse aurora. The former is associated with well defined structures, such as arcs and rays. Diffuse aurora, on the other

hand, is identified by weak emissions and less well-defined structures, which may be hard to observe optically. Associated with the precipitation region where the proton flux is the highest, diffuse aurora tends to be found on a circle around the magnetic poles. Even tough it is practical to categorize aurora by means of these two types, discrete structures may still be found inside diffuse aurora.

The first comparisons between the auroral ovals in the Northern and Southern Hemispheres revealed a high degree of conjugacy, particularly for diffuse aurora during quiet geomagnetic conditions. The conjugacy between the aurora borealis and aurora australis was less prominent for discrete auroras, during active conditions (Akasofu, 1978). It has been proposed that this is due to the mechanisms by which the two categories of auroras are excited and the acceleration mechanisms of the precipitating particles (Akasofu, 1978). Nevertheless, the auroras in the two hemispheres are in general often assumed to be mirror images of each other, where charged particles are evenly distributed among the two hemispheres. However, Laundal and Østgaard (2009) report significant asymmetries in the auroral pattern between the Northern and Southern Hemispheres. These asymmetries are thought to be caused by differences in the ionospheric conductivities in the two hemispheres, resulting in season-dependent inter-hemispheric currents.

The differences in ionospheric conductivity are season dependent due to the changing orientation of the Earth relative to the Sun throughout the year. For most of the year, one polar region will be sunlit, while the other will be in darkness. The sunlit hemisphere will experience a higher degree of ionization due to the Sun, causing an enhanced ionospheric conductivity. The opposite hemisphere would have a lower ionospheric conductivity, which is typically associated with more intense auroras (Laundal & Østgaard, 2009).

2.3 Isotropic Boundary

Within the auroral zones, there is a distinct boundary between a poleward region with isotropic particle precipitation and an equatorward region with anisotropic particle fluxes. In the first region the loss cone is filled, meaning that the flux of particles moving along the magnetic field is equal to the flux of particles moving with 90° relative to the local magnetic field. In the case of anisotropic particle fluxes, the loss cone is empty, meaning that the majority of particles are trapped and gyrate along the magnetic filed lines. The boundary between these two regions is known as the isotropic boundary (IB) (Ganushkina et al., 2005).

The isotropic particle precipitation on the nightside has a number of characteristic features. First of all, the IB is observed for ions for all MLT values and for all levels of magnetic activity. Secondly, the latitude of the IB is dependent on the particle species that is precipitating, the MLT and the level of magnetic activity. Thirdly, the latitude of the IB is not equal for all MLT for a given particle species with the same energy. The IB will be further polewards at local noon than at local midnight. Lastly, the higher the energy of a given particle species, the lower the latitude of the IB (Ganushkina et al., 2005). In general the IB concept is mostly applicable to ions due to their larger gyro radius compared to electrons.

The IB arises due to pitch angle scattering. A particle's pitch angle is defined as the angle between the particle's velocity vector and the local direction of the magnetic field (Kivelson & Russell, 1995). The pitch angle scattering observed in the polar region is associated with the violation of the first adiabatic invariant. The term "Adiabatic invariant" refers to a constant of motion that does not change when a slow change (relative to the period of motion) is made to a system. In plasma physics there are three such invariants. The first adiabatic invariant μ is equivalent to the magnetic moment of a gyrating particle (Chen, 2015).

$$\mu = \frac{m{v_\perp}^2}{2B} \tag{2.8}$$

In Equation 2.8, m is the mass of the particle, $v_\perp$ is the velocity component of the particle that is perpendicular to the magnetic field $\boldsymbol{B}$. The first adiabatic variant is violated when $\omega << \omega_c$, i.e. when the frequency ω, characterizing the rate of change of the magnetic field $\boldsymbol{B}$, is less than the cyclotron frequency ω_c with which the particle gyrates along the magnetic field lines (Chen, 2015). Likewise, μ is not invariant if the Larmor radius r_L approaches the magnetic field line curvature R_c in the equatorial current sheet. The radii are given by

$$r_L = \frac{mv_\perp}{|q|B} \tag{2.9}$$

$$R_c = \frac{B_z}{\partial B_x / \partial z} \tag{2.10}$$

where m is the particle mass and $v_\perp$ is the particle velocity, B is the magnetic field strength and q is the particle charge. The magnetic field line curvature

R_c in Equation 2.10 is given by the B_x and B_z components of the magnetic field.

The principal mechanism causing pitch angle scattering, and consequently particle precipitation, is thought to be wave-particle interactions (Ganushkina et al., 2005). Several mechanisms have been discussed as potential causes, including scattering related to field line curvature (FLC) and scattering due to electromagnetic ion cyclotron waves (EMIC) (Dubyagin, Ganushkina, & Sergeev, 2018).

2.4 POES and MetOp Satellites

The Polar-orbiting Operational Environmental Satellites (POES) are a large fleet of meteorological satellites, operated by NOAA. The first POES satellite (TIROS 1) was launched on April 1, 1960. In the following 50 years, the TIROS-series satellites were replaced by the ITOS-series and NOAA-series satellites. On February 6, 2009, the final NOAA-series satellite (NOAA-19) was launched. The successor to the NOAA satellites is the European Space Agency's and EUMETSAT's fleet of three MetOp satellites, launched in 2006, 2012 and 2018, respectively. The objective of the POES satellites is to provide extensive meteorological and environmental measurements, encompassing both surface (e.g. ice coverage, vegetation) and atmospheric conditions (e.g. temperature, ozone distribution). In addition to scientific instruments, the NOAA satellites carry Search and Rescue (SAR) technology (NASA, 2019). The satellite data used in this thesis was obtained by five different satellites from the NOAA-series (NOAA-15 through NOAA-19), as well as MetOp-A (also known as MetOp-02). Table 2.1 lists the launch and operational dates of these six satellites, in addition to their current status. All six satellites are located in low-Earth Sun-synchronous near polar orbits. Their altitudes vary between 800 and 900 km, with inclinations close to 90°. Sun-synchronous orbits are characterized by the satellite passing over the same location on Earth at approximately the same local solar time each day. This occurs when the orbital plane of the satellite rotates at the same rate as the Earth revolves around the Sun, i.e. one revolution per year (Fortescue, Swinerd, & Stark, 2011). Table 2.2 lists a selection of orbital parameters for the six satellites. Due to their 100-minute orbital periods, the satellites complete approximately 14 orbits per day, providing daily global coverage (NOAA, 2020). Figure 2.4 illustrates the orbital footprints in the polar regions of five of the six satellites as of March 2013 in a MLT-ILAT coordinate system.

Table 2.1: Operational status of NOAA-15 through NOAA-19 and EUMETSAT MetOp-A. Data from NOAA (2015), NOAA (2016) and NOAA (2019).

Satellite	Launch Date	Operational Date	Status (2019)
NOAA-15	1998-05-13	1998-12-15	Active
NOAA-16	2000-09-21	2001-03-20	Decommissioned
NOAA-17	2002-06-24	2002-10-15	Decommissioned
NOAA-18	2005-05-20	2005-08-30	Active
NOAA-19	2009-02-06	2009-06-02	Active
MetOp-A	2006-10-19	2007-05-21	Active (2016)

Table 2.2: Orbital parameters of POES NOAA-15 through NOAA-19 and EUMETSAT MetOp-A. LTAN is the local time of the ascending node. The data was obtained from NOAA (2015), NOAA (2016) and NOAA (2019).

Satellite	Alt. [km]	Period [min]	Inclination [°]	LTAN [hh:mm:ss]
NOAA-15	807	101.1	98.50	17:41:25
NOAA-16	849	102.1	99.00	21:01:39
NOAA-17	810	101.2	98.70	19:02:32
NOAA-18	854	102.1	98.74	17:40:01
NOAA-19	870	102.1	98.70	14:29:07
MetOp-A	817	101.4	98.70	21:29:05

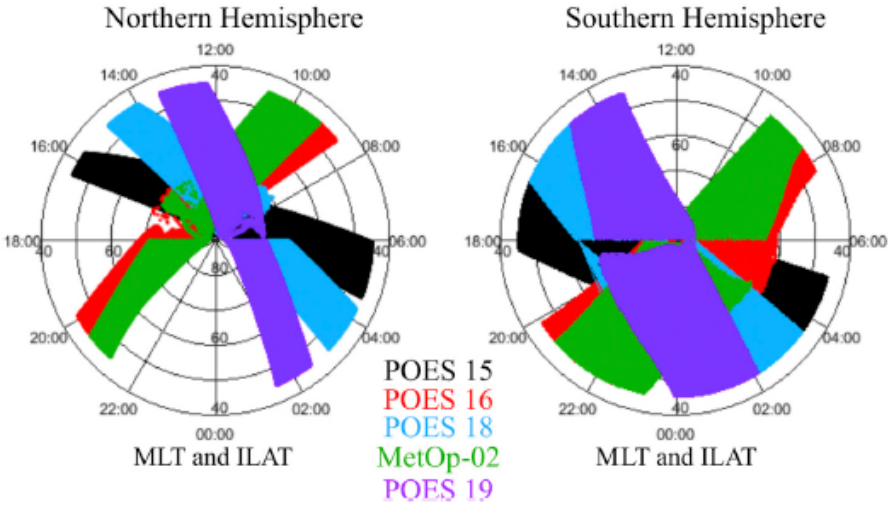

Figure 2.4: The footprints of the orbits of four different POES satellites, as well as MetOp-02 in the Northern and Southern Hemispheres. The footprints are given in an MLT-ILAT coordinate system and correspond the the satellite orbits as of March 2013. From Søraas et al. (2018).

2.5 Instruments

POES and MetOp satellites carry various instruments for environmental and atmospheric research (NASA, 2019). For auroral research the satellites carry the Space Environment Monitor (SEM) instrument suite. The purpose of these instruments is to monitor the flux of energetic electrons and protons into the atmosphere and measure the particle radiation environment at the spacecraft altitude. The magnitude and spatial distribution of these quantities are good measures of the atmospheric response to the energy input provided by the energetic particles, as well as the level of auroral activity. (Evans & Greer, 2004). Beginning with NOAA-15 (launched May 13, 1998), all POES satellites, as well as the fleet of MetOp satellites (EUMETSAT, 2020), carry an upgraded SEM. Named SEM-2, the upgraded instrument suite consists of two different sensors: the Total Energy Detector (TED) and the Medium Energy Proton and Electron Detector (MEPED). The two sensors are combined with a common Data Processing Unit (DPU), serving as the interface between the two sensors and the spacecraft bus (NASA, 2019). Figure 2.5 displays a schematic overview some components of a POES spacecraft. The coordinate axes given in the figure provide a means of describing the orientation of the spacecraft. Figure 2.6 shows a photograph of the three main components of the SEM-2 instrument suite.

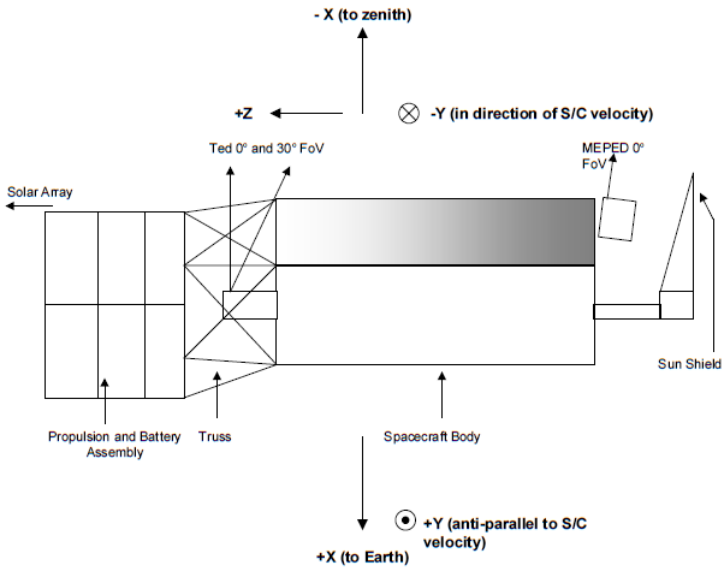

Figure 2.5: Schematic of the main components of a POES satellite, including the location of the TED and MEPED instruments, as well as the spacecraft's orientation with respect to the Earth. From Evans and Greer (2004).

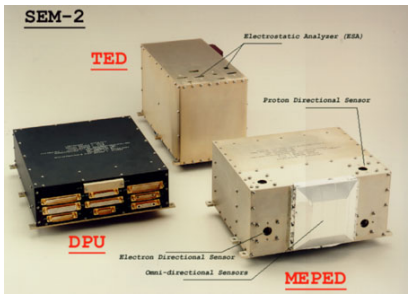

Figure 2.6: Image of the the TED and MEPED instruments, as well as the DPU, comprising SEM-2. From EUMETSAT (2020).

2.5.1 TED

The Total Energy Detector measures the energy flux of electrons and protons precipitating down into the polar atmosphere. The TED sensor in SEM-2 consists of eight separate charged-particle detectors, of the cylindrical curved-plate electrostatic analyzer Channeltron type. These eight detector systems are divided into two sets of four, where each set of detector systems is oriented differently relative to the geomagnetic field, such that directional energy fluxes relative to the geomagnetic field are measured at two different angles. One set of four detectors is mounted on the spacecraft (which is three-axis stabilized), such that the centre of the field of view of each of the four detectors is facing outward along the local zenith, and parallel to the radial vector connecting the centre of the Earth and the satellite. The other set of four detectors is oriented such that the field of view of each of the detector is centred at a 30° angle relative to the Earth-centre-to-satellite radial vector. The former set of four detectors is referred to as the 0° detectors, whereas the latter is referred to as the 30° detectors (Evans & Greer, 2004).

Within each set of four detectors. Two of the detectors measure electrons, one over the energy range from 50 eV to 1.000 eV, and the other from 1.000 eV to 20 keV. The remaining two detectors measure protons over the same two energy ranges. The field of view of the low-energy electron detector system is $6.7° \times 3.3°$, half angles. For the proton detector system with the same energy, the field of view is $6.6° \times 8.7°$, half angles. The field of view for the high-energy detector systems is $1.5° \times 9°$, half angles, for both the electron and protons detectors. Within each of the eight detectors, the voltage of the electrostatic analyzer is swept in order to measure the particles within the energy ranges specified in Table 2.3. The first eight energy bands (1 though 8) were for the low-energy (50 eV to 1.000 eV) proton and electron detectors, while the last eight energy bands (9 thought 16) were applied to the high-energy (1.000 eV to 20 keV) proton and electron detectors (Evans & Greer, 2004).

Table 2.3: Energy band limits for the TED electrostatic analyzers. Data from Evans and Greer (2004).

Channel	Lower Energy [eV]	Centre Energy [eV]	Upper Energy [eV]
1	50	61	73
2	73	89	106
3	106	139	154
4	154	189	224
5	224	274	325
6	325	399	472
7	473	580	688
8	688	844	1, 000
9	1, 000	1, 227	1, 454
10	1, 454	1, 784	2, 115
11	2, 115	2, 595	3, 075
12	3, 075	3, 774	4, 472
13	4, 472	5, 488	6, 503
14	6, 503	7, 980	9, 457
15	9, 457	11, 605	13, 753
16	13, 753	16, 877	20, 000

2.5.2 MEPED

The Medium Energy Proton and Electron Detector consists of a set of eight solid-state energetic particle detectors systems, measuring the particle flux of electrons and protons with energies ranging from 30 keV to 200 MeV. Particles within this energy range originate from the Van Allen radiation belt, solar proton event and low-energy galactic cosmic rays. MEPED consists of eight separate detector systems, allowing the instrument to detect particle fluxes over such a wide range of energies. Two of the eight detectors are proton solid-state detector telescopes, monitoring the proton flux in six energy bands over a range of 30 keV to 6.900 keV. The next two detectors are electron solid-state detector telescopes monitoring the electron flux in three energy bands over a range of 30 keV to 2.500 keV. The remaining four detectors systems are omni-directional solid-state detector systems, which measure highly energetic protons over many different angles of incidence (Evans & Greer, 2004).

The field of view for the two electron and and the two proton solid state detector telescopes is 30°. For both electrons and protons, one detector is positioned such that is the central axis of the field of view is oriented 9° from the $-X$ direction towards the $-Z$ direction, in the XZ-plane. This detector is called the 0° detector. The other detector is oriented such that the central axis of the field of view is rotated by 9° from the $+Y$ direction towards the $-Z$ direction, in the

YZ-plane. This detector is called 90° detector, Figure 2.5 illustrates how these detector telescopes are oriented relative to the satellite. The configuration of the 0° and 90° MEPED detectors relative to Earth's magnetic field and the atmospheric loss cone is illustrated in Figure 2.7. Table 2.4 provides an overview of the energy channels measured by both the electron and protons solid state detectors. The omni-directional detectors are not descried in any further detail since measurements made by these detectors are not used in this thesis.

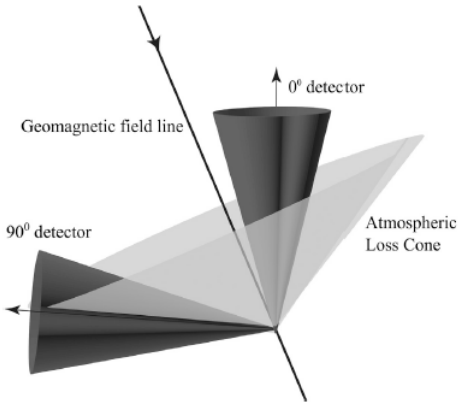

Figure 2.7: Schematic of the opening angle of the 0° and 90° MEPED detectors, relative to the Earth's magnetic field line and the atmospheric loss cone. The size of the loss cone and the opening angles are not fixed throughout the satellite orbit. From Søraas et al. (2018).

Table 2.4: Particle energy ranges measured by the MEPED electron and proton detector channels. Data from Evans and Greer (2004).

	Electrons	
Channel	Lower Energy [keV]	Upper Energy [keV]
E1 (0°/90°)	30	2, 500
E2 (0°/90°)	100	2, 500
E3 (0°/90°)	300	2, 500
	Protons	
Channel	Lower Energy [keV]	Upper Energy [keV]
P1 (0°/90°)	30	80
P2 (0°/90°)	80	240
P3 (0°/90°)	240	800
P4 (0°/90°)	800	2, 500
P5 (0°/90°)	2, 500	6, 900
P6 (0°/90°)	6, 900	-

2.6 Magnetic Activity Indices

The size and location of the auroral oval is highly dependent on the level of disturbance of the Earth's magnetic field. It is useful to provide a measure of the level of magnetospheric activity in the form of a magnetic activity index. These indices are functions of a parameter that is related to the disturbance of the geomagnetic field. Usually, the geomagnetic disturbance is measured using magnetometers located on the surface of the Earth. Throughout the past decades, a large number of indices have be defined; the simplest indices being based on subjective observations of the disturbance level. In this section, some of the most common indices which appear in the literature are presented: the range indices (K, K_p, A and A_p), the Q index, the substorm indices (AU, AL, AE and AO) and the storm index Dst (Kivelson & Russell, 1995). According to Starkov (1994b), the K_p, AL and AE indices are the most popular for characterizing disturbances in the Earth's magnetic field. In more recent years, other indices have been derived, using space-based instrumentation. One such index, based on solar wind parameters rather than magnetometer data is the merging electric field (E_m), based on a solar wind-magnetosphere coupling function (Newell, Sotirelis, Liou, Meng, & Rich, 2007).

Many of the aforementioned indices have been used as the basis for various aruroal oval models. According to Xiong, Lühr, Wang, and Johnsen (2014), E_m correlates best with the auroral oval boundaries, for boundaries determined by means of field-aligned currents. However, Thomsen (2004) argues that, despite its shortcomings, many magnetospheric properties correlate with K_p and that the index is a good measure for magnetospheric convection. Because K_p has been recorded as far back as the 1930s and is still widely used for current auroral oval models (see e.g. Wagner and Neuhäuser (2019)), it was decided to base the model developed in this thesis on the K_p index. Furthermore, the Feldstein auroral oval boundaries may be expressed in terms of K_p, simplifying the comparison to the new model. In the following, the K_p index is described in detail. Other central magnetic activity indices are mentioned briefly.

2.6.1 The K and and Kp Indices

The K index is a three-hour range index, first defined by Julius Bartels in 1939. The day is divided into eight intervals, each three hours in duration. Each interval is assigned an integer value between 0 and 9 (starting at UT 00), representing the level of geomagnetic disturbance. The index derived by considering the difference between the maximum and minimum deviation from a smooth curve representing the daily background variation in the magnetic field, within a three-hour period. The daily background variation for a given element of the magnetic field represents the expected level of magnetic activity

on a magnetically quiet day, given the season, the current solar activity and lunar phase. For each of the three magnetic elements (or components) comprising the local magnetic field vector, the range between the highest and lowest deviation from the background curve is calculated. The three magnetic elements are usually expressed in terms of declination D and the horizontal component H and the downwards vertical component Z, or by means of a local rectangular coordinate system with northward X, eastward Y and vertically downward Z components (Bartels, Heck, & Johnston, 1939). The element with the largest deviation, measured by the amplitude a in units of γ is used as a basis for the value of the K index Bartels (1957a).

The measured K value is unique to a given magnetic observatory. Depending on their location, different observatories will record different K values for the same geomagnetic disturbance. The range of the disturbance variation a for a given magnetic observatory is related to K on a quasi-logarithmic scale. The values of a that correspond to a given K value are determined by the latitude of a given observatory. Consequently, each observatory has chosen its own range limits to determine the K value. For instance, for an observatory at approximately 50° geomagnetic latitude, $K = 5$ if a exceeds 500 γ. However, each observatory does not derive its own scale for K values. Instead, the observatory chooses a predetermined set of range limits, based on the observatory's geomagnetic latitude (Bartels, 1957a).

Because most observatories will measure different K values, it is useful to define a common global K index, known as the K_p index (Kivelson & Russell, 1995). Currently, the K_p index is published by GFZ The German Research Centre for Geosciences in Postdam (Matzka, 2020). For a given observatory, there will be significant diurnal variations in the recorded K value throughout the eight-intervals. Particularly at auroral latitudes, certain K values will be recorded more frequently for a given three-hour interval than others. These variations may be mitigated by introducing a standardized K index, K_s. The standardized K_s index is essentially a conversion of the K index, that may be treated as a continuous variable. Finally, the K_p index is defined as the average of the standardized K_s indices from a fixed number of magnetic observatories. It is currently measured using a network of 13 magnetometer stations. As illustrated in Figure 2.8, the observatories are located at mid-latitudes (35° to 60°) in both the Northern and Southern Hemispheres (ISGI, 2013).

The K_p index may take on values between 0 and 9, where 0 represents quiet geomagnetic conditions and and value above 5 indicates a geomagnetic storm (Sigernes et al., 2011). However, as opposed to the K index, the K_p is defined on a scale of thirds: 0o, 0+, 1−, 1o, 1+, 2−, 2o, 2+, ..., 8+, 9−, 9o, such that the interval between two integer values is divided into three parts. Simplified, K_p may also be expressed on an integer scale, where 0o, 1o, 2o, 3o, 4o, 5o, 6o, 7o, 8o, 9o

correspond to the integers 1, 2, 3, 4, 5, 6, 7, 8, 9. (Bartels, 1957a). The A and A_p indices are daily average equivalents to the K and K_p indices, respectively. These indices are useful for long-term studies (Kivelson & Russell, 1995). As opposed, to the K and K_p indices, the A and A_p indices are linear in nature Bartels (1957a).

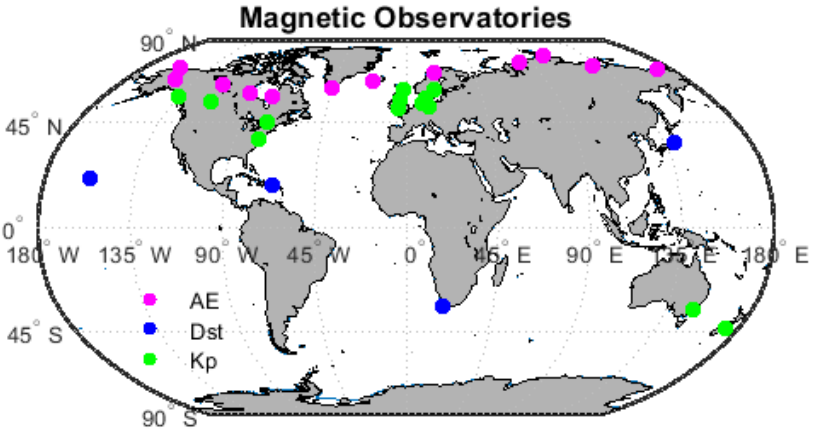

Figure 2.8: The geographic locations of the magnetometer stations used to derive the *AE* (magenta), *Dst* (blue) and K_p (green) indices. Seven of the thirteen observatories used to determine the K_p index are located in Europe. The geographic coordinates of the magnetometer stations were obtained from ISGI (2013).

2.6.2 The Q Index

The Q index forms the basis for some of the early work on the morphology of the auroral oval. The index represents the maximum deviation of the horizontal component of the local magnetic field, relative to a quiet reverence level within a 15-minute interval (Starkov, 1994b). The Q index is defined on a scale from 0 to 11 (Bartels, 1957b), where 0 indicates quiet geomagnetic conditions and 6 or more represents a high level of activity. In certain aspects, the Q index is similar to the K indices. However, the Q index has the advantage of being defined on a time scale of 15 minutes, significantly shorter than the three-hour time scale of the K index. Moreover, the Q scale is not latitude-dependent, meaning a uniform scale may be adapted for all observatories (Bartels, 1957b).

2.6.3 The Auroral Electrojet Indices

The substorm indices (AU, AL, AE and AO), also known as the auroral-electrojet indices, provide a measure of the strength of the auroral electrojet currents in the Earth's ionosphere. The indices are currently calculated based on measurements of the horizontal component of the geomagnetic field, using a network of 12 high-latitude observatories, between 56°N and 78°N (see Figure 2.8) (ISGI, 2013). The auroral upper (AU) index is the maximum positive magnetic disturbance measured by any observatory within the network at a given instant in time. Correspondingly, the auroral lower (AL) index is the minimum magnetic disturbance measured by any observatory. The AE index is defined as the difference between AU and AL: $AE = AU - AL$, whereas the AO index is the average of the auroral upper and lower indices: $AO = (AU + AL)/2$ (Kivelson & Russell, 1995).

2.6.4 The Dst Index

The disturbance storm time (Dst) index is a measure of the strength of the ring current (Newell et al., 2007). Since the ring current lies in the equatorial plane, magnetic measurements are conducted by four low-latitude observatories, between 36°N and 34°S (See Figure 2.8) (ISGI, 2013). The derivation of the Dst index is based on the same principles as the derivation of substorm indices. However, as opposed to the substorm indices, Dst is corrected for long-term and diurnal variations in the Earth's magnetic field. This requires the definition of a quiet baseline value, which is done by considering days with no activity that are not close to a magnetic storm recovery, and taking a sequence of values with minimum diurnal variation (occurring a midnight). A polynomial may be fitted to these values, which subsequently may be subtracted from all data collected at a given observatory throughout an entire year. Intervals with low magnetic activity within the data sequence are defined by means of another magnetic activity index. The data within the quiet intervals are corrected for any bias due to geomagnetic storms. By applying Fourier analysis to this data, the resulting coefficients and harmonics may be used to predict the horizontal component of the magnetic field at any given time. Having found the baseline value of the magnetic field, the amplitude of the residual magnetic field is scaled by dividing it by the cosine of the observatory's magnetic latitude. Taking the average of the scaled residuals as measured by a global network of observatories at a given instant in time yields the Dst index (Kivelson & Russell, 1995).

2.6.5 Solar Wind-Magnetosphere Coupling Function

Newell et al. (2007) defines a coupling function for the interaction between the solar wind and the magnetosphere. By correlating several coupling functions to 10 different magnetic activity indices (including the K_p, AL, AU, AE and Dst indices), the electric field merging rate $\mathrm{d}\Phi_{MP}/\mathrm{d}t$ was found to provide the best correlation with the largest number of indices (all indices, except Dst):

$$\frac{\mathrm{d}\Phi_{MP}}{\mathrm{d}t} = {v_{sw}}^{\frac{4}{3}} {B_t}^{\frac{2}{3}} \sin^{\frac{8}{3}}\left(\frac{\theta_c}{2}\right) \tag{2.11}$$

where v_{sw} is the solar wind velocity, $B_t = \sqrt{{B_y}^2 + {B_z}^2}$ is the magnitude of the interplanetary magnetic field (IMF), the factor $\sin^{8/3}(\theta_c/2)$ represents the percentage of IMF lines that merge and θ_c is the IMF clock angle ($\tan\theta_c = B_y/B_z$). In order to take into account the "memory-effect" of the magnetosphere-ionosphere system, $\mathrm{d}\Phi_{MP}/\mathrm{d}t$ may be integrated to find the integrated merging rate E_m:

$$E_m(t,\tau) = \frac{\int_{t_1}^{t} \frac{\mathrm{d}\Phi_{MP}}{\mathrm{d}t}(t') \exp\left(\frac{t'-t}{\tau}\right)}{\int_{t_1}^{t} \exp\left(\frac{t'-t}{\tau}\right)} \tag{2.12}$$

where t_1 and the e-folding time τ (the time interval for which a quantity increases or decreases by a factor of e) are determined experimentally (Xiong & Lühr, 2014). As a coupling function for the solar wind-magnetosphere interaction, E_m represents another index for the level of disturbance in the Earth's magnetic field. Due to the fact that E_m is derived from solar wind parameters, it is not a magnetic activity index in the same sense as the other indices mentioned here.

2.7 The Feldstein Auroral Oval Model

Feldstein and Starkov (1967) defined an auroral oval model using a large network of all-sky cameras during the IGY, from 1957 to 1958. The location of the auroral ovals were defined as a function of the Q index. As the model was derived purely from ground-based optical observations, it provides a good indication for where aurora may be seen for an observer on the ground. As a result, it remains in use today. However, the model does not distinguish between the auroral ovals in the Northern and Southern Hemispheres. Holzworth and

Meng (1975) applied a curve fitting to the statistical ovals defined by Feldstein, deriving a mathematical model for the location of the auroral oval, and comparing the model to satellite images from the Defense Meteorological Satellite Program (DMSP). Subsequently, Starkov (1994a) used a similar method to express the equatorward, poleward and diffuse auroral oval boundaries, based on Feldstein's observations. However, instead of correlating the ovals to the Q index, Starkov (1994a) expressed the oval boundaries in terms of the AL index.

The Feldstein auroral oval model, as defined by Starkov (1994a), expresses the corrected geomagnetic latitude θ of the poleward, equatorward and diffuse boundaries of the auroral oval as a sum of sinusoids. Although originally expressed as a function of the AL index, Starkov (1994b) defined a conversion equation, allowing the oval boundaries to expressed in terms of a selection of magnetic activity indices, by means of the following third-order polynomial:

$$AL = c_0 + c_1 M + c_2 M^2 + c_3 M^3 \tag{2.13}$$

where M may be any of the Q, K_p or AE indices. The values of the coefficients $\{c_0, c_1, c_2, c_3\}$ depend on which of the indices are related to each other (Starkov, 1994b). For instance, if AL is expressed in terms of K_p, the coefficients $\{c_0, c_1, c_2, c_3\} = \{18$ nT, -12.3 nT, 27.2 nT, -2.0 nT$\}$ (Starkov, 1994b).

Sigernes et al. (2011) presents the auroral oval boundaries given by Starkov (1994a) using the following notation:

$$\theta_m = A_{0m} + A_{1m}\cos[15(t + \alpha_{1m})] + A_{2m}\cos[15(2t + \alpha_{2m})] + A_{3m}\cos[15(3t + \alpha_{3m})] \tag{2.14}$$

where the index $m \in \{0, 1, 2\}$ indicates whether Equation 2.14 refers to the poleward ($m = 0$), equatorward ($m = 1$) or equatorward diffuse aurora ($m = 2$) boundaries. The amplitudes $\{A_{0m}, A_{1m}, A_{2m}, A_{3m}\}$ are in units of degrees of latitude, while the phases $\{\alpha_{0m}, \alpha_{1m}, \alpha_{2m}, \alpha_{3m}\}$ are in units of decimal hours. The local time t is expressed in hours. Starkov (1994a) estimates the values of the amplitudes and phases directly from the AL index:

$$A_{im} \text{ or } \alpha_{im} = b_{0m} + b_{1m} \log_{10} \mid AL \mid + b_{2m} \log_{10}{}^2 \mid AL \mid + b_{3m} \log_{10}{}^3 \mid AL \mid \quad (2.15)$$

where the index $i \in \{0, 1, 2, 3\}$ indicates which amplitude or phase is to be calculated for a given boundary m. Based on the calculated A_{im} indices, Starkov (1994a) provides a means of determining the total area S of the oval for a given boundary type m:

$$S = \pi \sum_{i=0}^{3} A_i{}^2 \quad (2.16)$$

In general, the coefficient A_{1m} tends to be significantly larger than A_{2m} and A_{3m}. In this case, Starkov (1994a) states that the auroral ovals may be represented as circles, the centre of which is translated relative to the geomagnetic pole. This approximation is valid if the accuracy of the boundaries is between 1° and 1.5° or higher.

Figure 2.9 illustrates an implementation of the Feldstein auroral oval model for selected K_p values between 0 and 9 in corrected geomagnetic coordinates (CGM), where the longitude is converted to MLT. Figure 2.10 display the same oval boundaries in a Cartesian coordinate system, providing a simple comparison between the oval boundaries for different levels of magnetic disturbance. An overview of the coefficients necessary to implement the Feldstein model are given by Starkov (1994a).

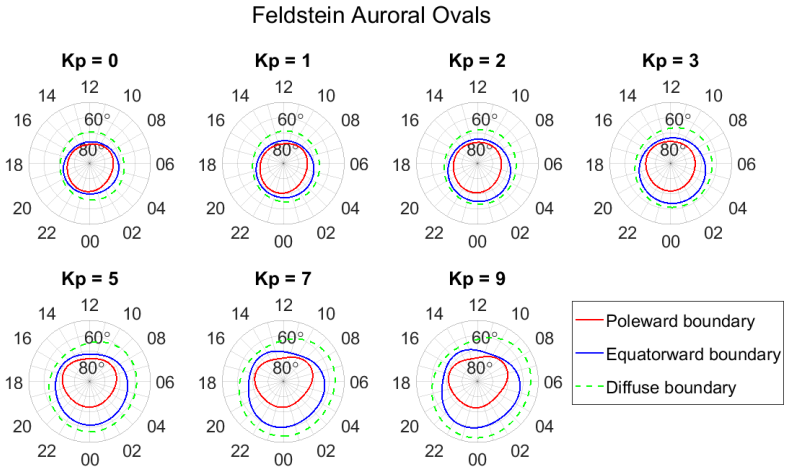

Figure 2.9: The Feldstein auroral ovals implemented for selected K_p values between 0 and 9 in a MLT-CGM coordinate system. The auroral oval is the area between the poleward boundary (red line) and the equatorward boundary (blue line). The green dashed line represents the equatorward boundary of the diffuse auroral oval.

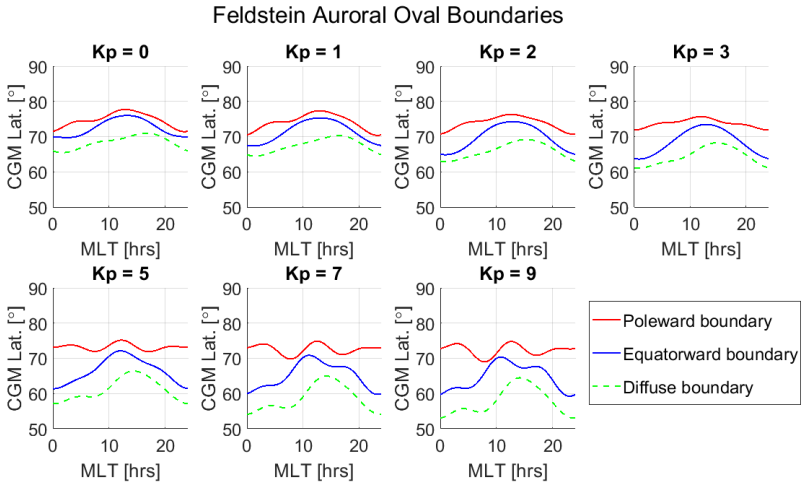

Figure 2.10: The Feldstein auroral ovals implemented for selected K_p values between 0 and 9 in a MLT-CGM coordinate system, as Cartesian coordinates. The auroral oval is the area between the poleward boundary (red line) and the equatorward boundary (blue line). The green dashed line represents the equatorward boundary of the diffuse auroral oval.

2.8 Aurora Forecast 3D

Aurora Forecast 3D is an aurora forecasting software application developed by Professor Fred Sigernes at the University Centre in Svalbard (UNIS). The application is free to download both for smartphones and for personal computers [1] (Sigernes, 2016). Figure 2.11 shows a screenshot from the interface. The application provides an interactive three-dimensional map of the Earth, which may be scaled and rotated in any direction. The auroral ovals are derived from the Feldstein model, and are projected onto the globe in both the Northern and Southern Hemispheres. The size and location of the ovals are updated in real-time. In addition to the projection of the auroral ovals, the application incorporates an Auroral Compass. This feature indicates in which cardinal direction auroras may be observed when looking up to the sky from a given ground track point. Furthermore, the Auroral Compass indicates what percentage of the sky is expected to be covered by auroras, as well as the location of the Sun and the Moon if they are within the field of view. The user can displace the ground track point and find the likelihood of observing auroras at any location on the globe.

The software application provides short-term forecasts for the auroral oval morphology, three and six hours ahead in time. These forecasts are based on the K_p values predicted by the NOAA Space Weather Prediction Center (SWPC) [2] , by means of Sun-monitoring satellites. Additionally, a three-day long-term forecast in K_p is provided. The application incorporates the option to manually change the K_p using the "dial" at the bottom of the screen, as displayed in Figure 2.11, allowing the user to see how the auroral ovals change in shape and size depending on the level of magnetic disturbance (Sigernes, 2016).

1. http://kho.unis.no/
2. https://www.swpc.noaa.gov/

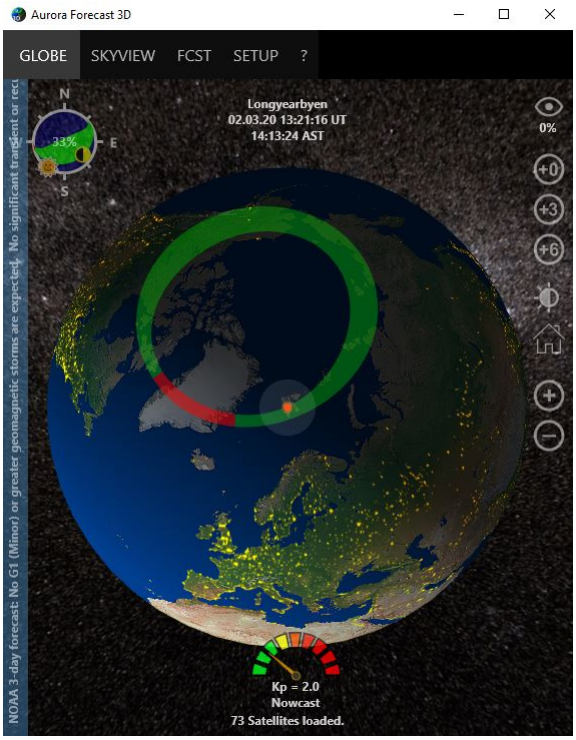

Figure 2.11: Screenshot from Aurora Forecast 3D. The image shows the auroral oval in the auroral oval in the Northern Hemisphere on March 2, 2020 at 13:21 UT. The green part of the auroral oval is the nightside aurora, while the red region represents the dayside aurora.

3 Methodology

3.1 The Satellite Data

The empirical satellite data from which the auroral oval models were derived, was collected throughout 2012. This was chosen to be a suitable year since six POES/MetOp satellites with identical instrumentation operated simultaneously for large parts of the year, providing good coverage. The satellite data was obtained from NOAA [1] through the University of Bergen (UiB). Table 3.1 provides an overview of the days (numbered 1 through 366, since 2012 was a leap year) during which the respective satellites collected data. The only period no data was recorded was a 10-day period from February 28 (day 59) to March 8 (day 68).

Table 3.1: Days during 2012 for which the six different POES satellites collected data.

Satellite	Data Coverage [2012 day no.]
MetOp-A	1-59, 69-366
NOAA-15	1-30, 68-366
NOAA-16	1-30, 68-366
NOAA-17	1-59, 68-366
NOAA-18	1-58, 68-366
NOAA-19	181-365

1. https://www.swpc.noaa.gov/

The satellite data was provided in the form of MATLAB files (.mat). All data files contained the particle measurements from both the TED and MEPED particle detectors for a given number of days during 2012. Each satellite provided measurements for both the Northern and Southern Hemispheres. For each data file, the measurements from each detector were labelled depending on which hemisphere the measurements originated from, as well as whether the measurements originated from the morning side or evening side of the Earth (in MLT). The two MLT regions were 12 hours wide, centred at midnight (MLT 00) and noon (MLT 12), respectively. Separate data arrays contained the MLT and ILAT of each measurement. In most cases, each detector channel on all six satellites recorded 180 measurements between 45° and 90° geographic latitude during each orbit on both the morning side and the evening side in each hemisphere. Consequently, the data provided a resolution of 0.25° in ILAT. With each satellite completing approximately 14 orbits per day, assuming the auroral oval boundaries were detected in both hemispheres on every orbit, up to 20,000 equatorward and poleward boundary detection events were recorded per detector channel (depending on the operational period of the satellites).

The auroral ovals were based on four different particle species/energy range combinations: electrons with energies $0.2 - 20$ eV (referred to as < 20 keV), protons with energies $0.2 - 20$ eV (referred to as < 20 keV), electrons with energies $30 - 2,500$ keV (referred to as > 30 keV) and protons with energies $30 - 80$ keV. These four particle types were chosen, since they represented different aspects of the auroral particle precipitation, although the higher energy electrons are not strictly associated with auroral emissions (Kivelson & Russell, 1995). The electrons and protons with energies < 20 keV were measured by TED, using the combined high-energy ($50 - 1,000$ eV) and low-energy ($1 - 20$ keV) detector systems. Electrons with energies > 30 keV were measured using the MEPED E1 solid state detector channel, while the protons with energies were measured by the MEPED P1 channel (see Table 2.4). In order to determine the equatorward and poleward boundaries for each of these four particle types, only the particle measurements from the 0° detectors were used. For the isotropic boundary, both the 0° and 90° MEPED electron and proton measurements were used. Table 3.2 provides an overview of the detectors, particle species ans energies used in this thesis.

The recorded magnetic activity indices for 2012, such as the K_p, Dst and AE, could be downloaded from the NASA's OMNIWeb Data Explorer, maintained by the Space Physics Data Facility at Goddard Space Flight Center (NASA, 2020). The data was downloaded with an hourly resolution. Due to the nature of the K_p index (see Section 2.6), this effectively meant a three-hour resolution. The OMNIWeb Data Explorer maintains a decimal version of the K_p index multiplied by a factor of 10, providing an accuracy to the first decimal place.

Table 3.2: The detectors, particle species and energy ranges of the particle precipitation measurements used to define auroral ovals.

Detector	Instrument	Particle	Orientation	Energy Range [keV]
1	TED	Electrons	0°	< 20
2	TED	Protons	0°	< 20
3	MEPED	Electrons	0°/90°	> 30
4	MEPED	Protons	0°/90°	$30 - 80$

3.2 Data Processing

The first step was to combine the variables of interest into one common file for every satellite. This was done in order to simplify further processing. The second step was to determine which particle measurements corresponded to the poleward and equatorward boundaries of the auroral oval. For this purpose, the data was categorized by hemisphere and morning/evening side. Within each of these four categories, the data for the four detectors for each of the six satellites was evaluated. Equatorward and poleward boundary detections were distinguished by comparing all particle measurements to certain boundary values. These values were different for each of the four detectors, but did not vary between the 0° and 90° MEPED detectors. The boundary values are given in Table 3.3.

Table 3.3: The boundary values defining equatorward and poleward boundaries for each of the four detectors.

Det. No.	Instrument	Particle	Energy [keV]	Boundary Value
1	TED	Electrons	< 20	0.05
2	TED	Protons	< 20	0.05
3	MEPED	Electrons	> 30	5,000
4	MEPED	Protons	$30 - 80$	100

By tracing measurements made during each orbit from both the north and the south, the equatorward and poleward boundaries were detected when the particle measurements exceed the given boundary values. Which boundary was being detected depended on the hemisphere, morning/evening side, as well as the direction in which the orbit was traced. Having found the location of every equatorward and poleward boundary detection in MLT-ILAT coordinates, it was possible to find the width of the auroral oval at at given time and MLT. Figures 3.1 and 3.2 show the location (in ILAT) of the auroral oval boundary detections around MLT 18 in the Northen and Southern Hemispheres from the TED electron detector on board the NOAA-17 spacecraft throughout 2012. The

boundary detection plots are stacked on top of the corresponding oval width as well as the measured flux throughout the year. The bottom two plots provide the K_p and Dst index for comparison.

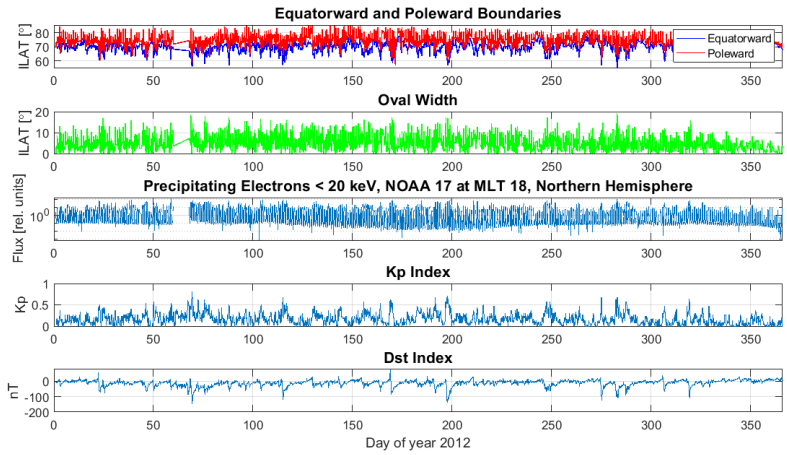

Figure 3.1: The auroral oval boundary location and width, as well as particle flux throughout 2012, as measured by the TED electron detector on board NOAA-17 at approximately 18 MLT in the Northern Hemisphere. The two lowest plots display the K_p and Dst index for the same period, respectively.

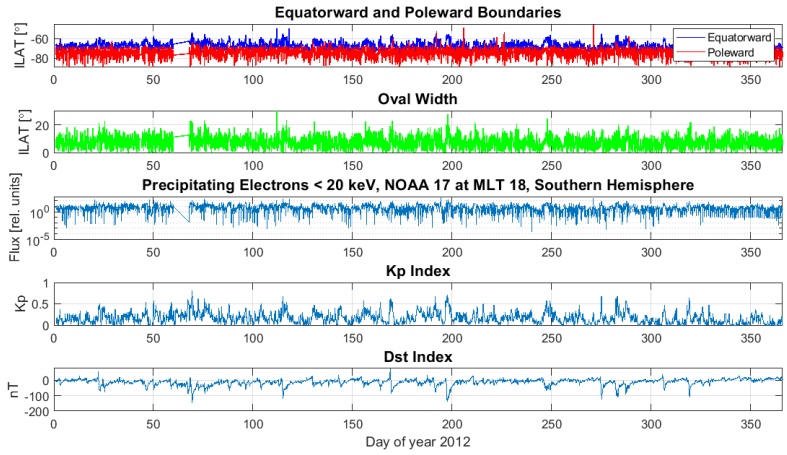

Figure 3.2: The auroral oval boundary location and width, as well as particle flux throughout 2012, as measured by the TED electron detector on board NOAA-17 at approximately 18 MLT in the Southern Hemisphere. The two lowest plots display the K_p and Dst index for the same period, respectively.

In order to correlate the location of the auroral oval boundaries to K_p, the boundary detection measurements had to be interpolated to fit the one-hour resolution magnetic activity indices. Once the the arrays specifying the poleward and equatorward boundary detections were of the same length as the array containing the K_p values, it was possible to combine the measurements made by each satellite and sort them according to detector and hemisphere.

Having defined the locations where the different detectors on all satellites measured the equatorward and poleward boundaries of the auroral oval, the boundaries had to be correlated with K_p. For this purpose, K_p was considered a continuous variable allowing fractional values. First, the boundary detection events were divided into 15 different K_p bins. The bins varied significantly in size, in order to ensure that there were at least 1000 detection events within each K_p bin. Due to the fact that K_p was recorded only to one decimal place, certain bins contained an order of magnitude more detections that others. Table 3.4 provides an overview of the K_p bin boundaries. The same K_p bins boundaries were used in for all detectors in both the Northern and Southern Hemispheres.

Table 3.4: K_p ranges of the 15 bins into which the boundary detection data was sorted. The same K_p ranges were used in both hemispheres.

Bin No.	Lower K_p	Upper K_p
1	0.0	0.1
2	0.2	0.3
3	0.4	0.7
4	0.8	1.1
5	1.2	1.5
6	1.6	1.9
7	2.0	2.1
8	2.2	2.3
9	2.4	2.7
10	2.8	3.1
11	3.2	3.5
12	3.6	3.9
13	4.0	4.3
14	4.4	4.9
15	5.0	8.9

Figures 3.3 through 3.6 show the distribution of the total number of boundary detections in MLT and ILAT, obtained by the MEPED electron detectors on all six satellites over the course of 2012. The four histograms show the distributions in the Northern and Southern Hemispheres for K_p bin number 4 and 10, respectively. In the Northern Hemisphere a four-hour wide region around

midnight local time is missing data coverage by the six satellites. This was a consequence of the satellite orbits. In the Southern Hemisphere, the boundaries were detected for all MLT values, although there were few detections around noon local time. This is illustrated by Figures 3.7 and 3.8, showing all the equatorward and poleward boundary detections in MLT-ILAT polar plots, in the Northern and Southern Hemispheres respectively. The figures show the detection events recorded by each of the four detectors for K_p bin number 10.

The next step was to sort the data within each K_p bin further by dividing every K_p bin into 48 contiguous MLT bins of equal size. Each MLT bin was 0.5 hours (7.5°) wide. The average equatorward and poleward boundary location of each MLT bin was calculated. In addition to the mean, the standard deviation in ILAT and MLT was calculated for the boundary detection events within each MLT bin. This provided a measure for the spread and uncertainty in the average boundary detection locations. The data processing procedure up to this point formed the basis for the three auroral oval models to be developed, and was preformed separately for the data originating from the Northern and Southern Hemispheres.

All three models (polynomial fit, ellipse fit and Fourier series fit) were based on the same principles: (1) Using a known fitting method to fit a particular type of function to the data (polynomial, ellipse, Fourier series), expressing ILAT in terms of MLT, obtaining the function coefficients. (2) Repeating the procedure for all 15 K_p bins in each hemisphere and correlate the individual function parameters to K_p by means of a second order polynomial fit. (3) Using the polynomial fit coefficients expressing each function parameter as a function of K_p, the function parameters may be calculated for an arbitrary K_p value. These parameters may in turn may be used to define the function determining the auroral oval boundary. These three steps were repeated for the equatorward and poleward boundary detection events recorded by all four detectors, in both hemispheres.

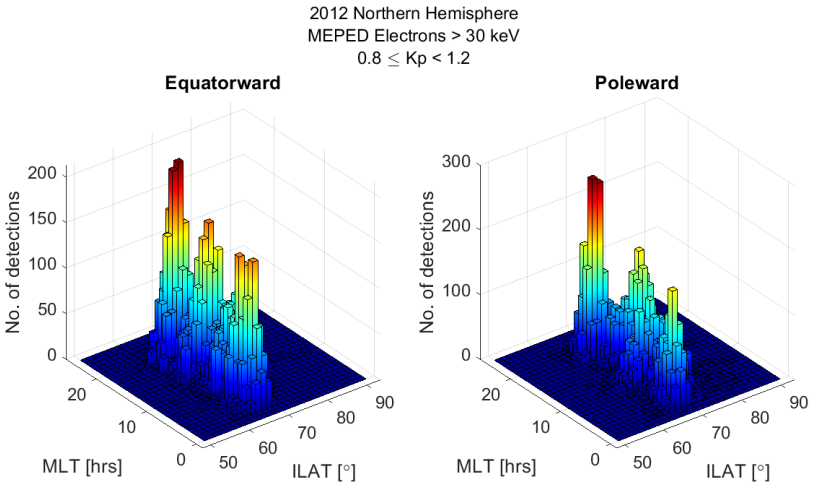

Figure 3.3: The total number of boundary detections distributed over ILAT and MLT in the Northern Hemisphere for K_p values between 0.8 and 1.2, obtained by the MEPED electron detector.

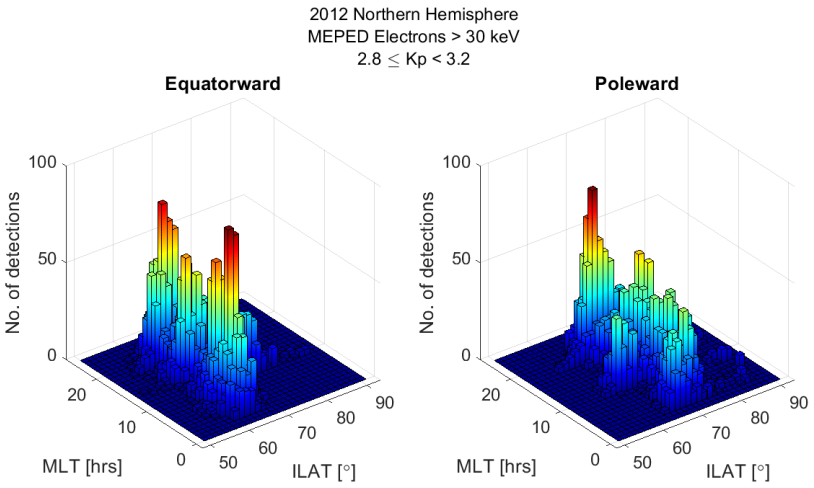

Figure 3.4: The total number of boundary detections distributed over ILAT and MLT in the Northern Hemisphere for K_p values between 2.8 and 3.2, obtained by the MEPED electron detector.

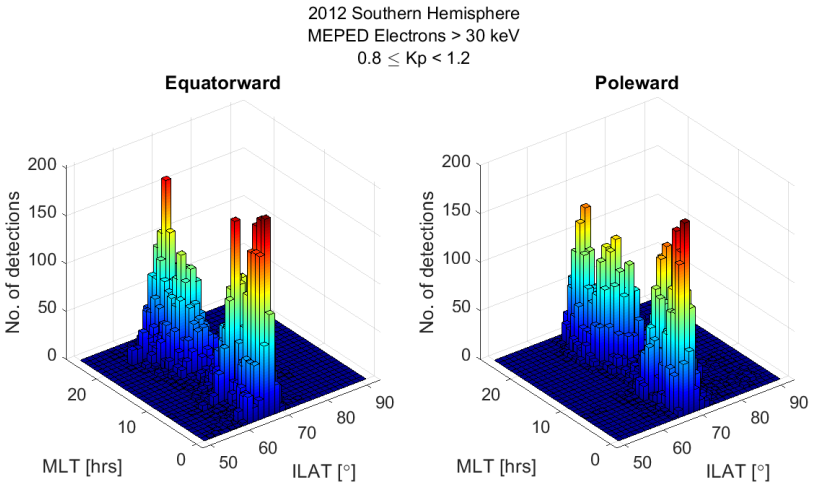

Figure 3.5: The total number of boundary detections distributed over ILAT and MLT in the Southern Hemisphere for K_p values between 0.8 and 1.2, obtained by the MEPED electron detector.

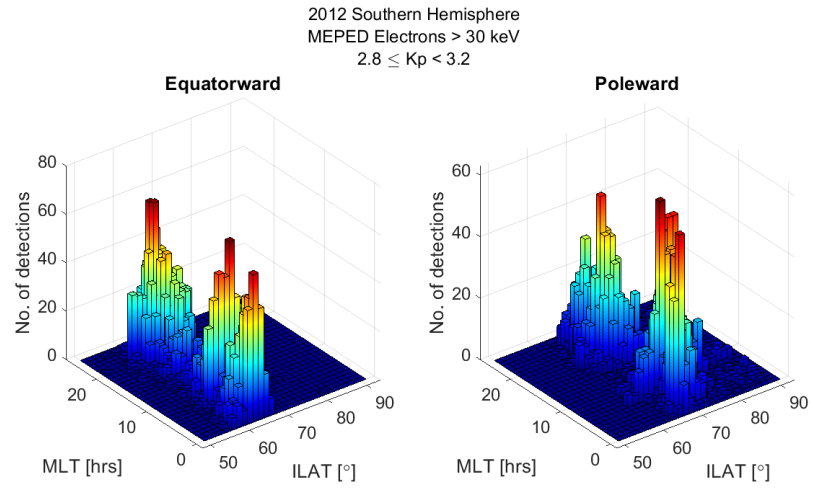

Figure 3.6: The total number of boundary detections distributed over ILAT and MLT in the Southern Hemisphere for K_p values between 2.8 and 3.2, obtained by the MEPED electron detector.

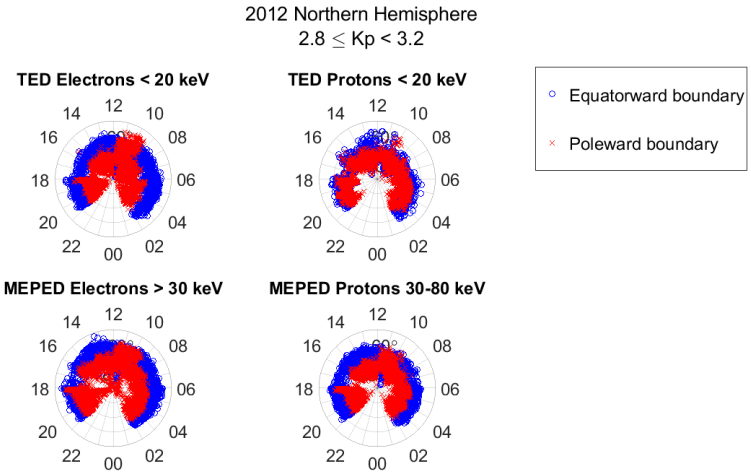

Figure 3.7: The boundary detection events in the Northern Hemisphere, measured by each of the four detectors, for K_p values between 2.8 and 3.2. The blue circles represent equatorward boundary detections, while the red x's mark the poleward detections.

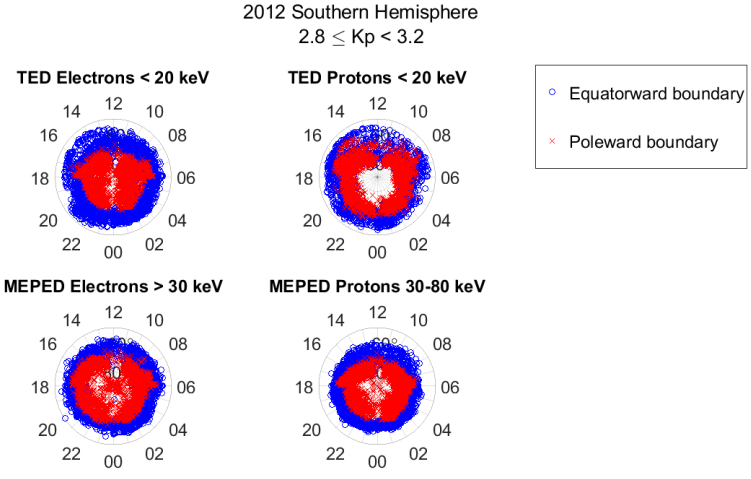

Figure 3.8: The boundary detection events in the Southern Hemisphere, measured by each of the four detectors, for K_p values between 2.8 and 3.2. The blue circles represent equatorward boundary detections, while the red x's mark the poleward detections

3.2.1 Polynomial Fit

Polynomials were fitted to the average boundary detections by means of MATLAB's integrated "polyfit" function [2]. This function provides the polynomial coefficients for a given polynomial order by means of a least-squares fitting method. This technique provides the best-fitting curve to a set of data points by minimizing sum of the squares of the residuals, i.e. the offsets between the fitted curve and the data points (Weisstein, 2020b). In order to prevent discontinuities at MLT 00 and MLT 24, the first and last 24 data points were added to the beginning (MLT 0 to 12) and end (MLT 12 to 24) of the chosen data range. Initially, an attempt was made to fit a polynomial to three consecutive identical data sets, in order to diminish discontinuities at the end of the central data set. However, this resulted in the variations within a 24-hour MLT period being averaged out, and required polynomials of very high orders to obtain any considerable ILAT variations within one data set. Consequently, only 24 data points were added to the beginning and the end of the data set. Fitting polynomials of various orders to the data showed that the lowest order polynomial that would fit the average boundary detections was 4. Consequently, each auroral oval boundary was described by a function similar to Equation 3.1, where x would be an MLT value and y the corresponding ILAT of a given boundary.

$$y(x) = p_1x^4 + p_2x^3 + p_3x^2 + p_4x + p_5 \tag{3.1}$$

The "polyfit" function calculated the polynomial coefficients $\{p_1, p_2, p_3, p_4, p_5\}$. Having found the coefficients for the equatorward and poleward boundaries within each K_p bin, for each of the four detectors, the five coefficients could be correlated to K_p, again by means of the "polyfit" function in MATLAB. A second order polynomial was deemed sufficient to accurately correlate the coefficients to K_p.

$$y(x) = q_1x^2 + q_2x + q_3 \tag{3.2}$$

Here, x was a K_p value and y one of the polynomial coefficients $\{p_1, p_2, p_3, p_4, p_5\}$. Having obtained the coefficients $\{q_1, q_2, q_3\}$ for both the equatorward and poleward boundary for each of the detectors in both hemispheres, it was possible to obtain the boundary of interest for an arbitrary K_p value between 0 and 9.

2. https://se.mathworks.com/help/matlab/ref/polyfit.html

3.2.2 Ellipse Fit

Since the shape of an oval can be approximated well by an ellipse, it was reasonable to attempt to express the equatorward and poleward boundaries of the auroral ovals in terms of ellipse parameters. The chosen ellipse fitting method was a direct least squares fitting, proposed by Fitzgibbon, Pilu, and Fisher (1999). This method was chosen due to its simplicity to implement, as well as being a non-iterative, robust and efficient ellipse fit. A characteristic of the method is that it returns an ellipse even if the data could be better approximated by a hyperbola.

The general second order polynomial describing any conic section is given by Equation 3.3. The term conic section refers to any curve than can be obtained by letting a plane intersect with the surface of a cone. There are three types of conic sections: parabolas, hyperbolas and ellipses.

$$F(\boldsymbol{a}, \boldsymbol{x}) = \boldsymbol{a} \cdot \boldsymbol{x} = c_1 x^2 + c_2 xy + c_3 y^2 + c_4 x + c_5 y + c_6 = 0 \tag{3.3}$$

In Equation 3.3 the polynomial coefficients are given by the vector $\boldsymbol{a} = \begin{bmatrix} c_1 & c_2 & c_3 & c_4 & c_5 & c_6 \end{bmatrix}$, while $\boldsymbol{x} = \begin{bmatrix} x^2 & xy & y^2 & x & y & 1 \end{bmatrix}$. A conic section may be fitted to a set of N data points by minimizing the sum of squared algebraic distances D_A. The term "algebraic distance" $F(\boldsymbol{a}, \boldsymbol{x}_i)$ refers to the distance from a given point (x, y) to the conic section $F(\boldsymbol{a}, \boldsymbol{x})$ (Fitzgibbon et al., 1999).

$$D_A(\boldsymbol{a}) = \sum_{i=1}^{N} F(\boldsymbol{x}_i)^2 \tag{3.4}$$

The method proposed by Fitzgibbon et al. (1999) introduced the equality constraint $4c_1c_3 - {c_2}^2 = 1$ in order to specifically ensure that ellipses were fitted, while maintaining efficiency. Furthermore, the polynomial coefficients were normalized, such that $\|\boldsymbol{a}\| = 1$.

For the purposes of ellipse fitting, it was useful to express the ellipses in terms of five parameters: the semi-major axis a, the semi-minor axis b, the position (x_0, y_0) in Cartesian coordinates of the ellipse centre relative to the origin of the coordinate system and the orientation angle ϕ_0 of the ellipse. The orientation angle is a measure of how the ellipse is oriented relative to the axes of the coordinate system. Equations 3.5 through 3.9 can be used to calculate these

five parameters using the coefficients in Equation 3.3 (Weisstein, 2020a).

$$a = \sqrt{\frac{2(c_1{c_5}^2 + c_3{c_4}^2 + c_6{c_2}^2 - c_2c_4c_5 - 4c_1c_3c_6)}{({c_2}^2 - 4c_1c_3)[\sqrt{(c_1 - c_3)^2 + {c_2}^2} - (c_1 + c_3)]}} \tag{3.5}$$

$$b = \sqrt{\frac{2(c_1{c_5}^2 + c_3{c_4}^2 + c_6{c_2}^2 - c_2c_4c_5 - 4c_1c_3c_6)}{({c_2}^2 - 4c_1c_3)[-\sqrt{(c_1 - c_3)^2 + {c_2}^2} - (c_1 + c_3)]}} \tag{3.6}$$

$$x_0 = \frac{2c_3c_4 - c_2c_5}{{c_2}^2 - 4c_1c_3} \tag{3.7}$$

$$y_0 = \frac{2c_1c_5 - c_2c_4}{{c_2}^2 - 4c_1c_3} \tag{3.8}$$

$$\phi_0 = \begin{cases} 0 & \text{if } c_2 = 0 \text{ and } c_1 < c_3 \\ \frac{\pi}{2} & \text{if } c_2 = 0 \text{ and } c_1 > c_3 \\ \frac{1}{2}\cot^{-1}\left(\frac{c_1 - c_3}{c_2}\right) & \text{if } c_2 \neq 0 \text{ and } c_1 < c_3 \\ \frac{\pi}{2} + \frac{1}{2}\cot^{-1}\left(\frac{c_1 - c_3}{c_2}\right) & \text{if } c_2 \neq 0 \text{ and } c_1 > c_3 \end{cases} \tag{3.9}$$

In the context of fitting ellipses to auroral oval boundary detections, (x_0, y_0) corresponds to the displacement of the ellipse centre from the magnetic pole, with the positive x-axis pointing towards MLT 00 and the positive y-axis towards MLT 6, in a MLT-ILAT coordinate system. The orientation angle ϕ_0 represents the angle between the semi-major axis of the ellipse and the midnight-noon axis, where a positive angle is measured counterclockwise. Figure 3.9 illustrates the five ellipse parameters graphically. The subsequent steps of the ellipse fitting method were closely related to the auroral oval ellipse fitting procedure published by Xiong and Lühr (2014), for the derivation of their CH-Aurora-2014 auroral oval model. However, whereas this the models described here are based on K_p, Xiong and Lühr (2014) used the solar wind-magnetosphere coupling function E_m as the underlying correlation variable.

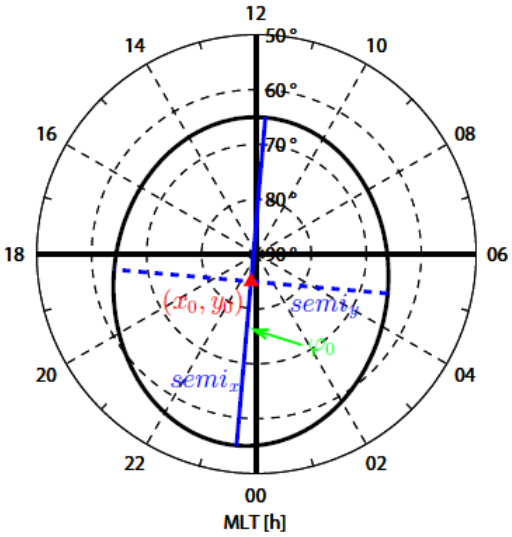

Figure 3.9: Visualization of the five ellipse parameters. The semi-major axis $semi_x$ and semi-minor axis $semi_y$, in solid and dashed blue, respectively, are equivalent to a and b. The red triangle represents the centre of the ellipse, with coordinates (x_0, y_0). The ellipse orientation angle ϕ_0 is measured counterclockwise. From Xiong and Lühr (2014).

The first step in deriving the ellipse fitting model was to convert each boundary detection from polar coordinates to Cartesian coordinates (x, y). This was done by means of Equation 3.10, where r_{det} and θ_{det} represented the location of a given detection in ILAT and MLT, respectively.

$$\begin{aligned} x &= r_{det} \cos \theta_{det} \\ y &= r_{det} \sin \theta_{det} \end{aligned} \tag{3.10}$$

Subsequently, the direct least squares fitting method could be applied, using a numerically stable version of the fitting procedure in MATLAB code, provided by Chernov (2020). The coefficients in 3.3 were converted into the five ellipse parameters by means of Equations 3.5 through 3.9. Next, equations had to be obtained to express the location r of the oval boundary for an arbitrary rotation angle θ (measured counterclockwise from the midnight-noon axis, with respect to the ellipse centre) in terms of the five ellipse parameters. The general ellipse equation in its most simple form in Cartesian coordinates is given by Equation 3.11. Again, a and b are the semi-major and semi-minor axes

of the ellipse, respectively (Weisstein, 2020a).

$$\frac{x^2}{a^2} + \frac{y^2}{b^2} = 1 \tag{3.11}$$

Combining Equation 3.11 with Equation 3.10, and exchanging r_{det} and θ_{det} for r_0 and θ, provides the general Ellipse equation in polar coordinates.

$$\frac{{r_0}^2 \cos^2\theta}{a^2} + \frac{{r_0}^2 \sin^2\theta}{b^2} = 1 \tag{3.12}$$

Solving Equation 3.12 with respect to the distance r_0 from the ellipse centre for a given angle θ yields (Weisstein, 2020a):

$$r_0(\theta) = \frac{ab}{\sqrt{(a\sin\theta)^2 + (b\cos\theta)^2}} \tag{3.13}$$

By incorporating the rotation angle ϕ_0, Equation 3.13 becomes:

$$r_0 = \frac{ab}{\sqrt{[a\sin(\theta + \phi_0)]^2 + [b\cos(\theta + \phi_0)]^2}} \tag{3.14}$$

However, since the ellipse might be centred at (x_0, y_0), rather than at the magnetic pole, the difference between the location of the ellipse centre and the magnetic pole must be taken into account. The distance r between the magnetic pole and the boundary defined by the ellipse is given by Equation 3.15. This corresponds to the co-latitude of the boundary for a given MLT (Xiong & Lühr, 2014).

$$r = \sqrt{[r_0\cos(\theta + \phi_0) + x_0]^2 + [r_0\sin + (\theta + \phi_0)x_0]^2} \tag{3.15}$$

The last step in fitting an ellipse to the data is to express r in terms of the MLT angle $\lambda = 2\pi \times (\text{MLT})/(24\text{ h})$, which may be expressed in terms of the ellipse parameters as:

$$\lambda = \tan^{-1}\left[\frac{r\sin(\theta + \phi_0) + y_0}{r\cos(\theta + \phi_0) + x_0}\right] \tag{3.16}$$

The offset of the ellipse centre relative to the magnetic pole causes the rotation angle θ to be different from the MLT angle λ. The rotation angle is measured relative to the ellipse centre, whereas λ is measured from the origin of the coordinate system, which in this case is the magnetic pole. Xiong and Lühr (2014) utilized a two-step approximation to minimize the error caused by the difference between these two angles. The approximation involves the following steps: firstly, θ was replaced with λ in Equations 3.14 and 3.15 for a given MLT value. Subsequently, another MLT angle λ' was calculated using Equation 3.16. Equation 3.17 was used to calculate the difference between λ' and λ.

$$\Delta\lambda = \lambda' - \lambda \tag{3.17}$$

In the second step, the corrected angle θ can be calculated for a given local time as:

$$\theta = \lambda + \Delta\lambda \tag{3.18}$$

The new angle θ incorporating the correction value $\Delta\lambda$ can finally be used in Equations 3.14 and 3.15 to obtain the location of the oval boundaries.

The last step of the ellipse fit model is to correlate the five ellipse parameters to the level of magnetic activity, represented by K_p. This procedure was analogous to determining the relationship between the polynomial coefficients and K_p. Again, the least squares "polyfit" function in MATLAB was used to find the second order polynomial u_1, u_2, u_3, describing each of the five ellipse parameters $\{a, b, x_0, y_0, \phi_0\}$ as a function of K_p.

$$y(x) = u_1 x^2 + u_2 x + u_3 \tag{3.19}$$

3.2.3 Fourier Series Fit

The Fourier series method is in may ways very similar to the polynomial fit method. The model is based on the same binned data as the two other models. Instead of fitting a polynomial or an ellipse to the average location of the poleward and equatorward boundary in each MLT bin, a second order Fourier series was fitted to the detections. This was done by means of the "fit" function available in MATLAB [3], providing a trigonometric Fourier series of the

3. https://se.mathworks.com/help/curvefit/fourier.html?requestedDomain=

form:

$$f(x) = a_0 + \sum_{i=1}^{n} [a_i \cos(i\omega x) + b_i \sin(i\omega x)] \tag{3.20}$$

where n is the number of harmonics and ω represents the fundamental angular frequency. For a second order Fourier series ($n = 2$), Equation 3.20 is truncated to:

$$f(x) = a_0 + a_1 \cos(\omega x) + b_1 \sin(\omega x) + a_2 \cos(2\omega x) + b_2 \sin(2\omega x) \tag{3.21}$$

where x represents MLT and $f(x)$ is ILAT. In order to ensure that the periodicity of the data was taken into consideration, i.e. that the ILAT of any given boundary at MLT 00 was the same at MLT 24, the Fourier series were fitted to three consecutive data sets. Once the Fourier Series had been fitted to the boundary detections, provided by the four detectors in both hemispheres, each of the six parameters $\{a_0, a_1, b_1, a_2, b_2, \omega\}$ could be correlated to K_p. This was entirely analogous to the previous two methods, by fitting a polynomial of the form

$$y(x) = v_1 x^2 + v_2 x + v_3 \tag{3.22}$$

to each of the coefficients, expressing them as a function of K_p.

3.3 Isotropic Boundary Detection

The IB can be detected by comparing the measured particle fluxes from the 0° and 90° detectors on the MEPED instrument. For any of the six satellites, the IB was detected if the following condition was satisfied:

$$\frac{\Phi_0}{\Phi_{90}} \geq 1 \tag{3.23}$$

where Φ_0 is the particle flux measured by the MEPED 0° detector and Φ_{90} is the particle flux measured by the MEPED 90°. IB detections were derived for both electrons with energies < 30 keV and protons with energies $30 - 80$ keV, in

both the Northern and Southern Hemisphere. The IB boundary detection data was sorted into the 15 K_p bins, which were again subdivided into 48 0.5-hour wide adjacent MLT bins. Similar to the equatorward and poleward boundary data, the mean and standard deviation of the data within each MLT bin were calculated in order to obtain an estimate for the spread in IB data. However, a complete model expressing the location of the IB as a function of K_p was not developed. Still, it was possible to evaluate the location of the IB with respect to the location of equatorward and poleward boundaries for different levels of magnetic activity.

4

Results

4.1 Boundary Detection

The boundary detection events obtained by each of the four detectors, for selected K_p bins in the Northern and Southern Hemispheres, are displayed in Figures 4.1 through 4.4. Each marker represents the mean location of the boundary detections within a 0.5-hour wide MLT bin. The error bars represent one standard deviation in ILAT (vertical) and MLT (horizontal) from the mean value. The green dashed vertical lines indicate the region between MLT 00 and MLT 24. The horizontal axes in both figures are slightly longer at both ends of the MLT region in order to accommodate error bars extending beyond the region. For instance, an error bar extending to MLT -2, in reality extends to MLT 22. In all subsequent data plots, the error bars are omitted in order to make the figures easier to interpret and less congested.

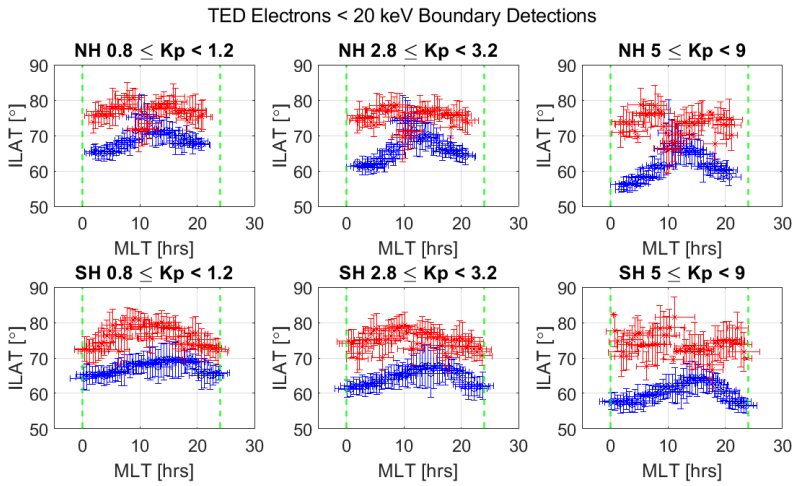

Figure 4.1: The TED electron average equatorward (blue) and poleward (red) boundary detection events with errors bars. The Error bars represent one standard deviation in ILAT (vertical) and MLT (horizontal). The vertical green bars indicate the region between MLT 00 and MLT 24.

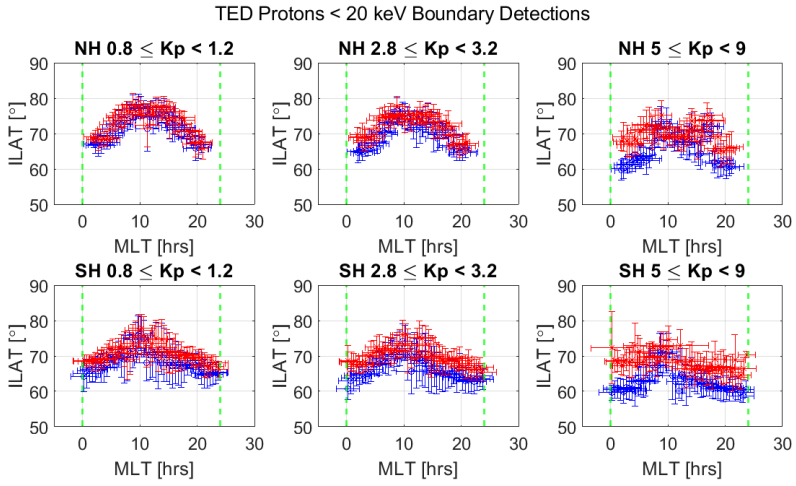

Figure 4.2: The TED proton average equatorward (blue) and poleward (red) boundary detection events with errors bars. The Error bars represent one standard deviation in ILAT (vertical) and MLT (horizontal). The vertical green bars indicate the region between MLT 00 and MLT 24.

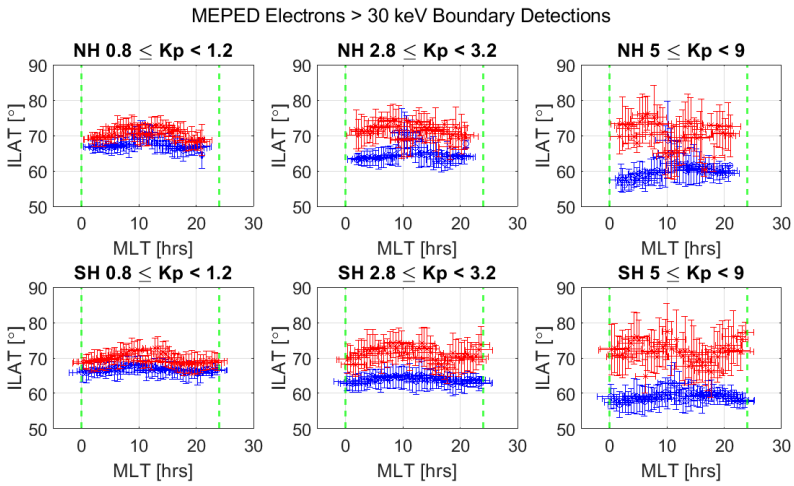

Figure 4.3: The MEPED electron average equatorward (blue) and poleward (red) boundary detection events with errors bars. The Error bars represent one standard deviation in ILAT (vertical) and MLT (horizontal). The vertical green bars indicate the region between MLT 00 and MLT 24.

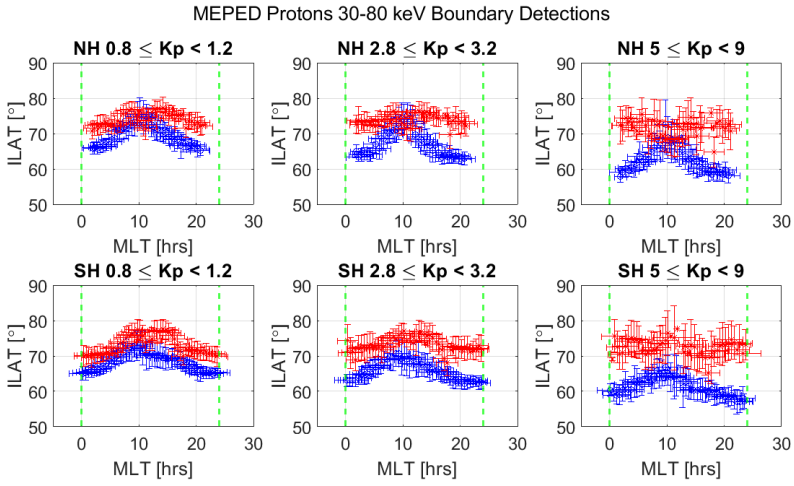

Figure 4.4: The MEPED proton average equatorward (blue) and poleward (red) boundary detection events with errors bars. The Error bars represent one standard deviation in ILAT (vertical) and MLT (horizontal). The vertical green bars indicate the region between MLT 00 and MLT 24.

4.2 Polynomial Model

Given the method presented in Chapter 3, the polynomial fit model can be implemented for any arbitrary K_p value between 0 and 9, by means of the following three steps: (1) Selecting the desired level of magnetic disturbance by means of the K_p value and choosing the hemisphere and the type of auroral oval boundary (equatorward/poleward, electron/proton and energy range) of interest. (2) Using the corresponding quadratic fit coefficients $\{q_1, q_2, q_3\}$ presented in the correlation figures in Appendix A.2, in combination with Equation 3.2 to calculate the fourth order polynomial coefficients $\{p_1, p_2, p_3, p_4\}$, describing the chosen oval boundary. (3) Calculate the ILAT of the boundary for a given MLT using Equation 3.1.

Figure 4.5 provides an example of the initial polynomial fit to the boundary detections measured by the TED electron detector. The figure shows the fits for three different K_p bins in both the Northern and Southern Hemisphere. The correlation between polynomial coefficients and K_p for the same detector are illustrated by Figures 4.6 and 4.7, for the equatorward boundary and poleward boundary respectively. A complete overview of similar figures for all fours detectors is given in Appendices A.1 and A.2. Figures 4.8 through 4.11 display the polynomial fit model implemented in a polar MLT-ILAT coordinate system for each of the four TED/MEPED electron/proton detectors. The figures show how the locations of the equatorward and poleward boundaries in both hemispheres change with increasing K_p, relative to the Feldstein ovals. It should be noted that that while the polynomial fit boundaries are expressed in a MLT-ILAT coordinate system, the Feldstein oval boundaries are expressed in terms of MLT and corrected geomagnetic (CGM) latitude.

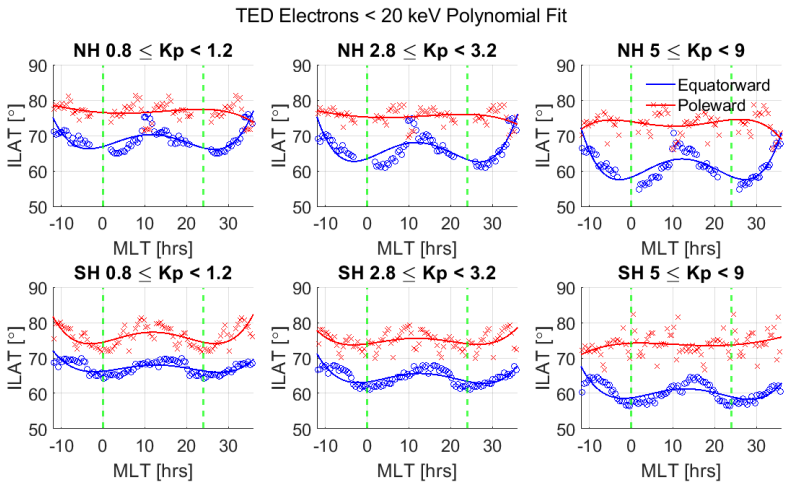

Figure 4.5: Fourth order polynomials fitted to the averaged boundary detections from the TED electron detector, for three K_P ranges in the Northern (NH) and Southern (SH) Hemispheres. The vertical dashed line in green represents the region between MLT 00 and MLT 24 within which the polynomial fit is valid.

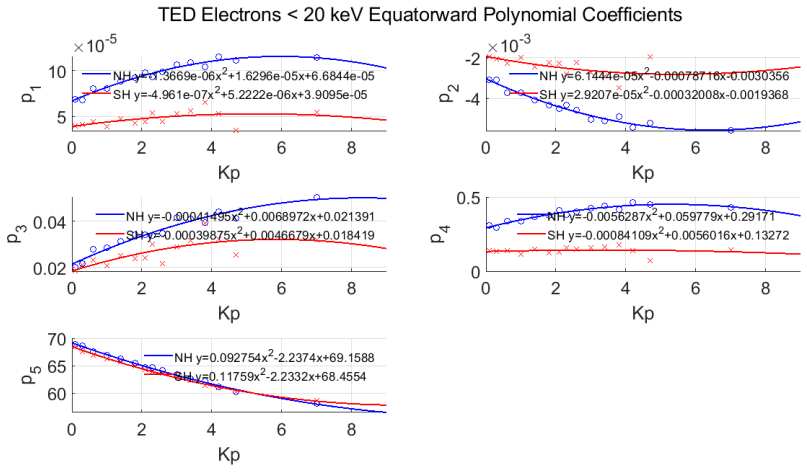

Figure 4.6: Second order polynomials correlating the five polynomial coefficients of the TED electron equatorward boundary to K_p, in both the Northern (NH in blue) and Southern (SH in red) Hemisphere.

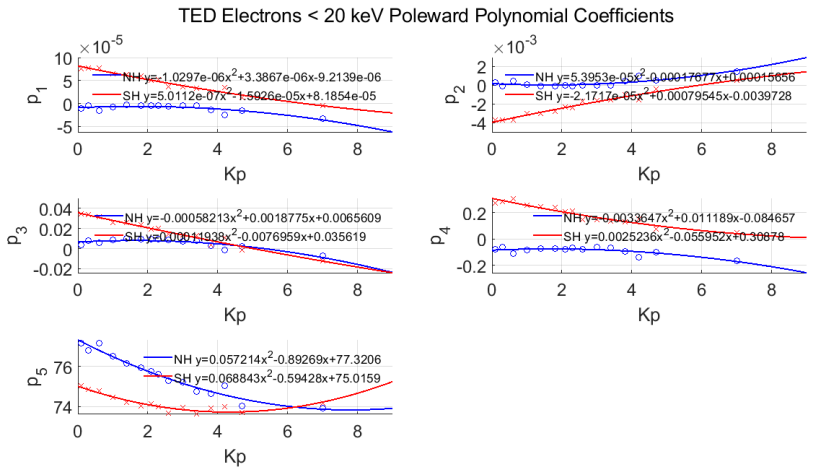

Figure 4.7: Second order polynomials correlating the five polynomial coefficients of the TED electron poleward boundary to K_p, in both the Northern (NH in blue) and Southern (SH in red) Hemisphere.

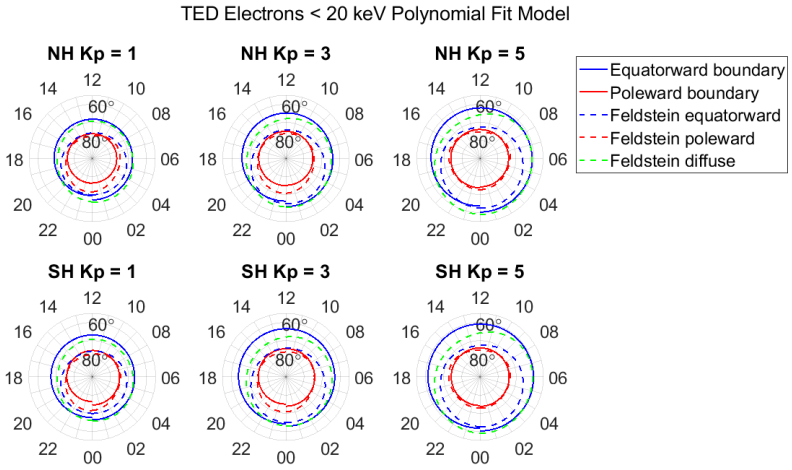

Figure 4.8: The TED electron auroral ovals estimated using the polynomial fit model for three different K_p values in the Northern (NH) and Southern (SH) Hemispheres. The dashed lines represent the Feldstein ovals for the same K_p values.

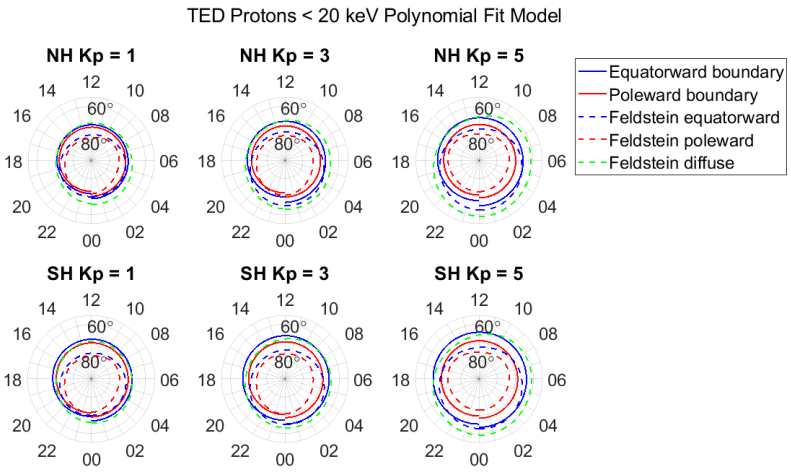

Figure 4.9: The TED proton auroral ovals estimated using the polynomial fit model for three different K_p values in the Northern (NH) and Southern (SH) Hemispheres. The dashed lines represent the Feldstein ovals for the same K_p values.

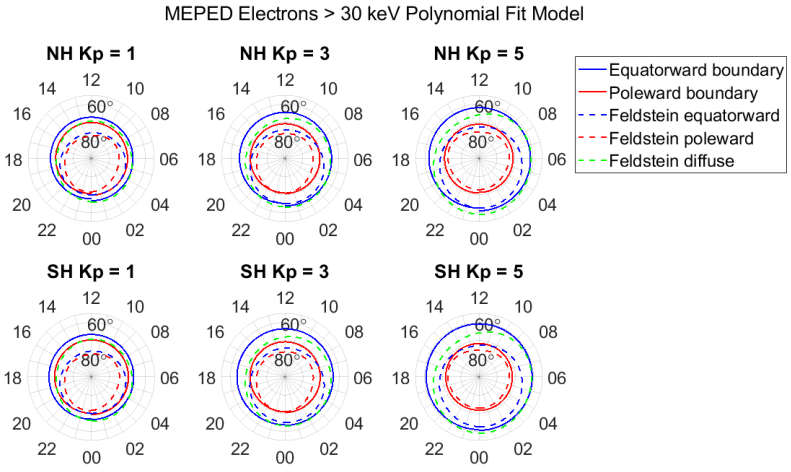

Figure 4.10: The MEPED electron auroral ovals estimated using the polynomial fit model for three different K_p values in the Northern (NH) and Southern (SH) Hemispheres. The dashed lines represent the Feldstein ovals for the same K_p values.

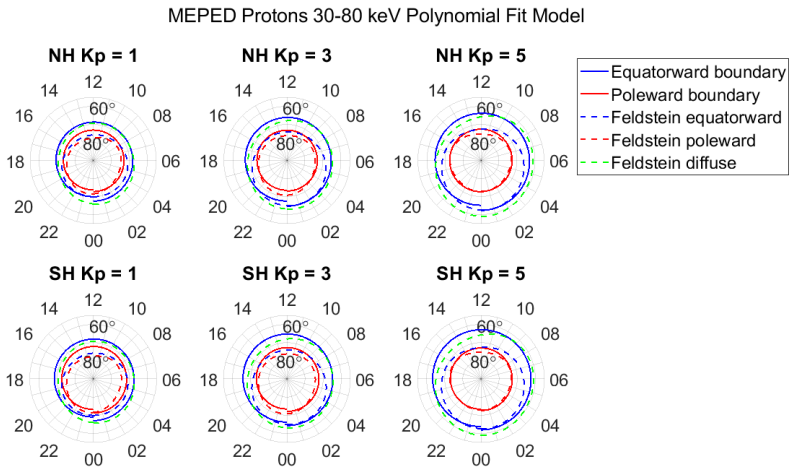

Figure 4.11: The MEPED proton auroral ovals estimated using the polynomial fit model for three different K_p values in the Northern (NH) and Southern (SH) Hemispheres. The dashed lines represent the Feldstein oval boundaries for the same K_p values.

4.3 Ellipse Model

Similar to the polynomial fit model, the implementation of the ellipse fit model can be broken down into the following steps: (1) Selecting the hemisphere, the particle type of interest and the K_p value for which the oval boundaries are to be found. (2) Choosing the quadratic fit coefficients $\{u_1, u_2, u_3\}$ from the correlation figures in B.2, matching the oval boundaries of interest and calculating the five ellipse parameters $\{a, b, x_0, y_0, \phi_0\}$ using Equation 3.19. (3) Inserting the five parameters into Equations 3.14 and 3.15 to calculate r_0 and r, using the MLT angle λ instead of θ in the equations. (4) Using Equation 3.16 to calculate a new angle λ' and calculating a new angle θ by means of Equations 3.17 and 3.18. (5) Combining the new angle θ with Equations 3.14 and 3.15 yields the location of the auroral oval boundary in ILAT for a given MLT.

Figures 4.12, 4.13 and 4.13 provided an example of the initial ellipse fits to the boundary detections and the correlation coefficients with K_p for the TED electron detector in both hemispheres. A complete overview for the remaining detectors is provided in Appendices B.1 and B.2. Figures 4.15 through 4.18 show the resulting implementation of the ellipse fit models for $K_p = 1$, $K_p = 3$ and $K_p = 5$ in both hemispheres, with the corresponding Feldstein oval boundaries superimposed onto the same set of axes. While the ellipse fit boundaries are expressed in MLT-ILAT coordinates, the latitude of the Feldstein boundaries is

given in CGM coordinates.

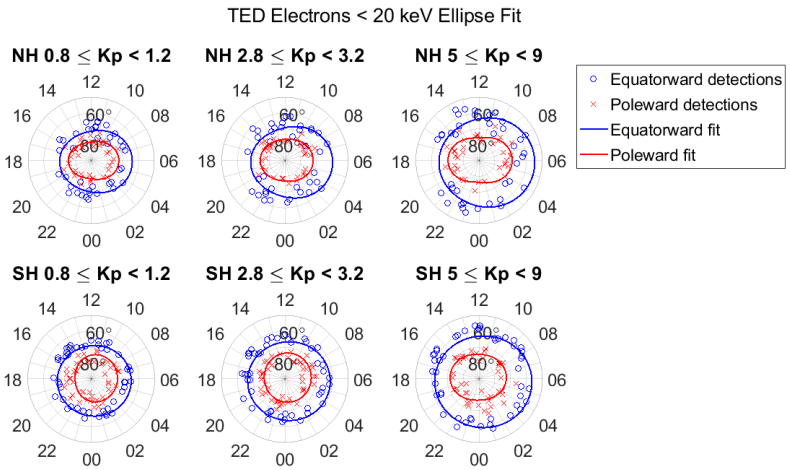

Figure 4.12: Ellipses fitted to TED electron boundary detection events, for three K_p ranges in the Northern (NH) and Southern (SH) Hemispheres.

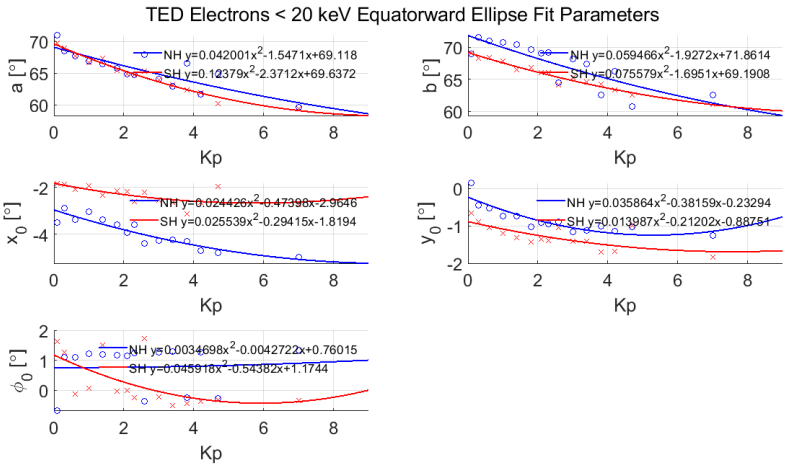

Figure 4.13: Second order polynomials correlating the five ellipse parameters of the TED electron equatorward boundary to K_p, in both the Northern (NH in blue) and Southern (SH in red) Hemisphere.

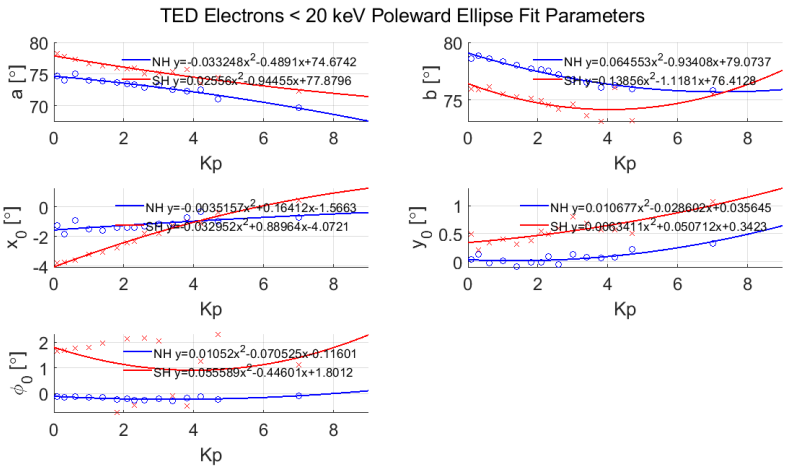

Figure 4.14: Second order polynomials correlating the five ellipse parameters of the TED electron poleward boundary to K_p, in both the Northern (NH in blue) and Southern (SH in red) Hemisphere.

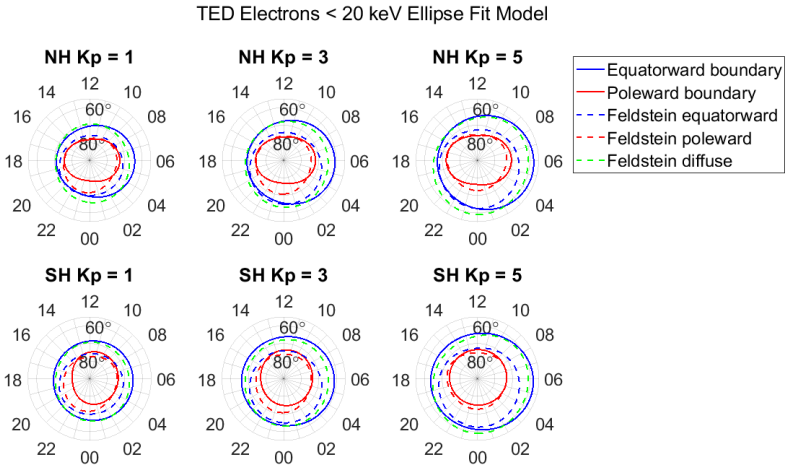

Figure 4.15: The TED electron auroral ovals estimated from the ellipse fit model for three different K_p values in the Northern (NH) and Southern (SH) Hemispheres. The dashed lines represent the Feldstein oval boundaries for the same K_p values.

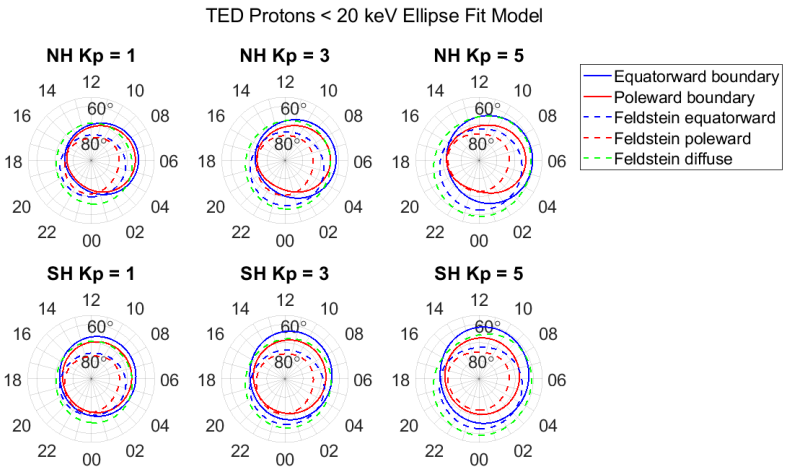

Figure 4.16: The TED proton auroral ovals estimated from the ellipse fit model for three different K_p values in the Northern (NH) and Southern (SH) Hemispheres. The dashed lines represent the Feldstein oval boundaries for the same K_p values.

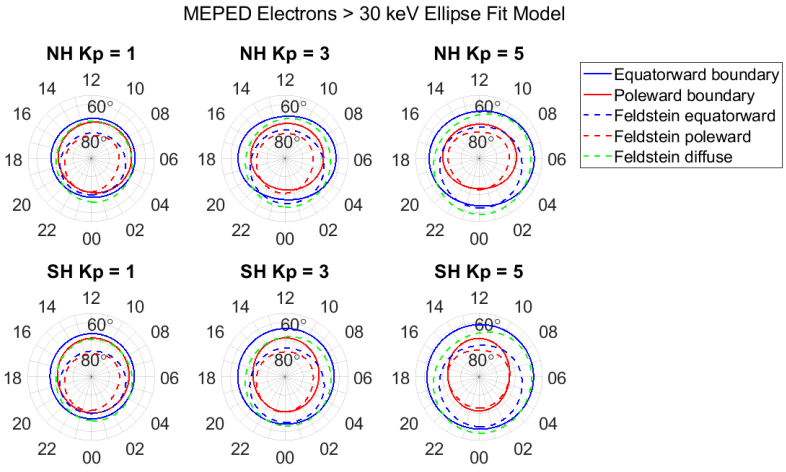

Figure 4.17: The MEPED electron auroral ovals estimated from the ellipse fit model for three different K_p values in the Northern (NH) and Southern (SH) Hemispheres. The dashed lines represent the Feldstein oval boundaries for the same K_p values.

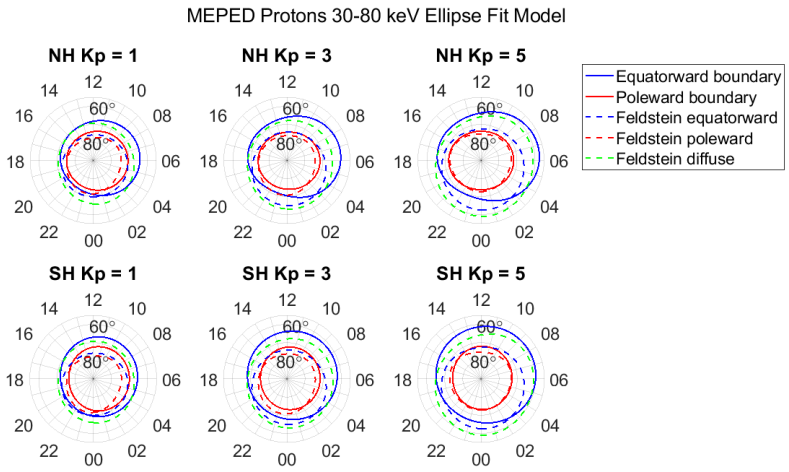

Figure 4.18: The MEPED proton auroral ovals estimated from the ellipse fit model for three different K_p values in the Northern (NH) and Southern (SH) Hemispheres. The dashed lines represent the Feldstein oval boundaries for the same K_p values.

4.4 Fourier Series Model

The implementation of the Fourier series model is analogous to the polynomial fit model, but the specific steps are repeated to provide clarity: (1) Selecting the hemisphere, the particle type of interest and the K_p value for which the oval boundaries are to be found. (2) Choosing the quadratic fit coefficients $\{v_1, v_2, v_3\}$ from the correlation figures in Appendix C.2 for the a given oval boundary, and calculating the six Fourier coefficients $\{a_0, a_1, b_1, a_2, b_2, \omega\}$ by means of Equation 3.22. (3) Using Equation 3.21 to calculate the ILAT of the boundary for a given MLT.

Figures 4.19, 4.20 and 4.21 show the Fourier series fit to the boundary detections and the correlation coefficients with K_p for the TED electron detector in the Northern and Southern Hemispheres. The green dashed vertical bars in Figure 4.19 indicate the region between MLT 00 and MLT 24, within which the model is valid. Appendices C.1 and C.2 provide similar figures for all four detectors. Figures 4.22 through 4.25 illustrate the implementation of the Fourier series model fit for all four detectors, together with the corresponding Feldstein oval boundaries. Again, the Fourier series boundaries are in MLT-ILAT coordinates, while the latitude of the Feldstein boundaries is given in CGM coordinates.

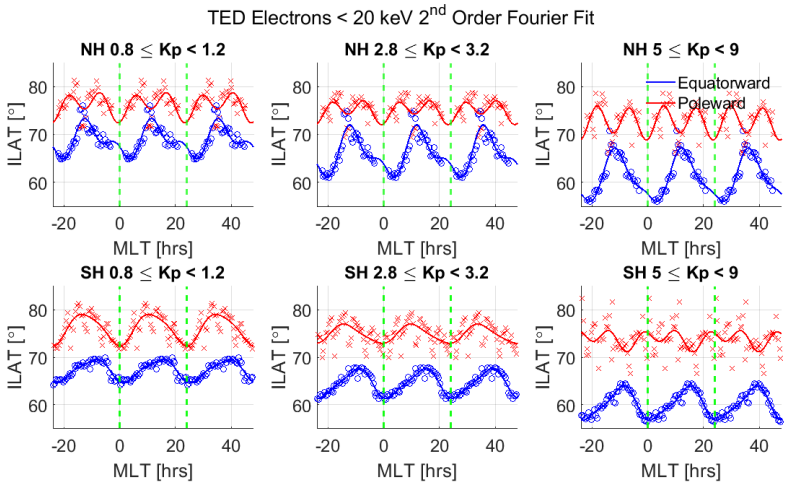

Figure 4.19: A second order Fourier series fitted to TED electron boundary detection events, for three K_p ranges in the Northern (NH) and Southern (SH) Hemispheres.

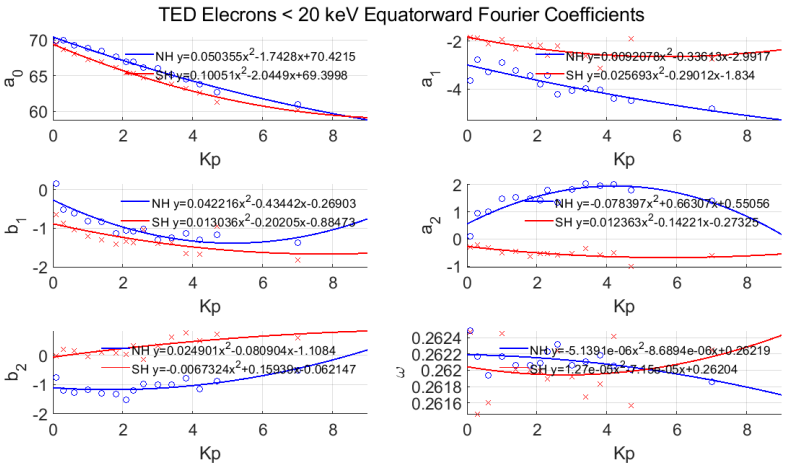

Figure 4.20: Second order polynomials correlating the six Fourier series coefficients of the TED electron equatorward boundary to K_p, in both the Northern (NH in blue) and Southern (SH in red) Hemisphere.

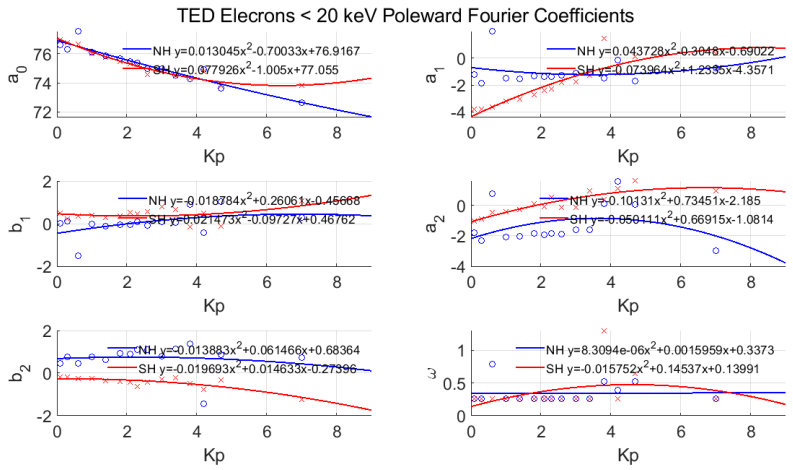

Figure 4.21: Second order polynomials correlating the six Fourier series coefficients of the TED electron poleward boundary to K_p, in both the Northern (NH in blue) and Southern (SH in red) Hemisphere.

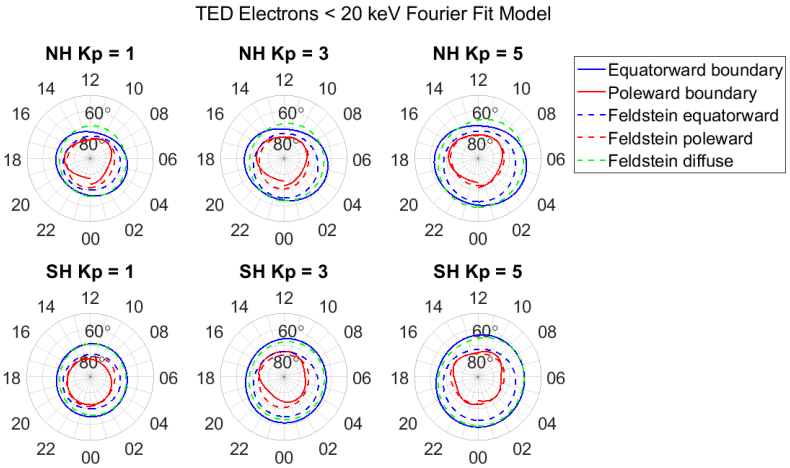

Figure 4.22: The TED electron auroral ovals determined by the Fourier series model for three different K_p values in the Northern (NH) and Southern (SH) Hemispheres. The dashed lines represent the Feldstein oval boundaries for the same K_p values.

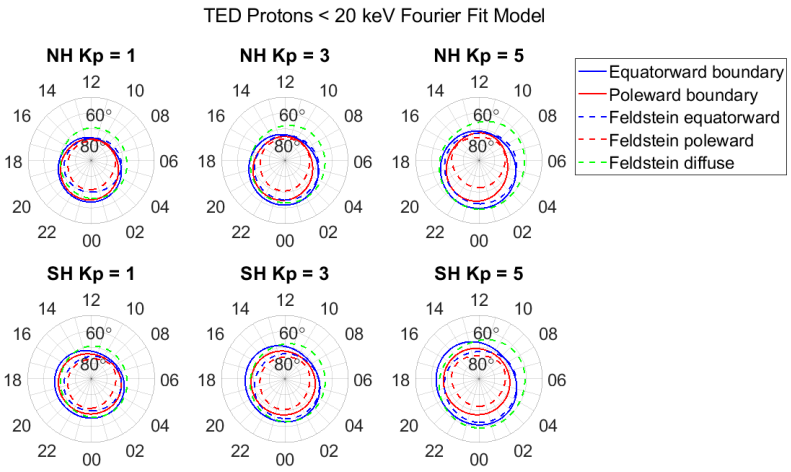

Figure 4.23: The TED proton auroral ovals determined by the Fourier series model for three different K_p values in the Northern (NH) and Southern (SH) Hemispheres. The dashed lines represent the Feldstein oval boundaries for the same K_p values.

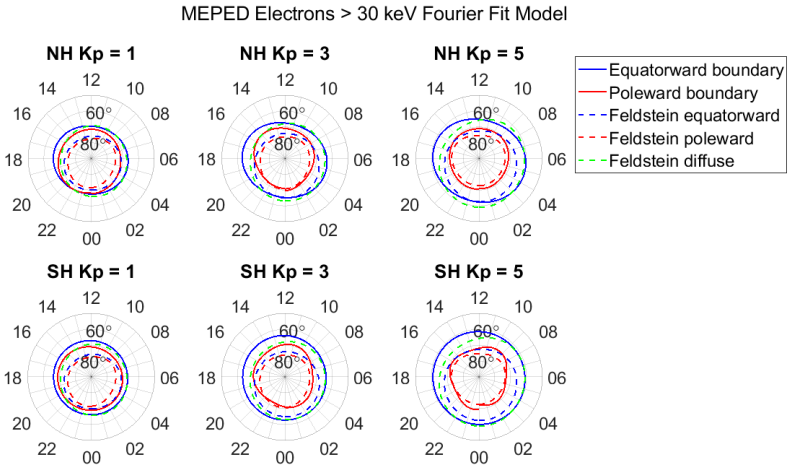

Figure 4.24: The MEPED electron auroral ovals determined by the Fourier series model for three different K_p values in the Northern (NH) and Southern (SH) Hemispheres. The dashed lines represent the Feldstein oval boundaries for the same K_p values.

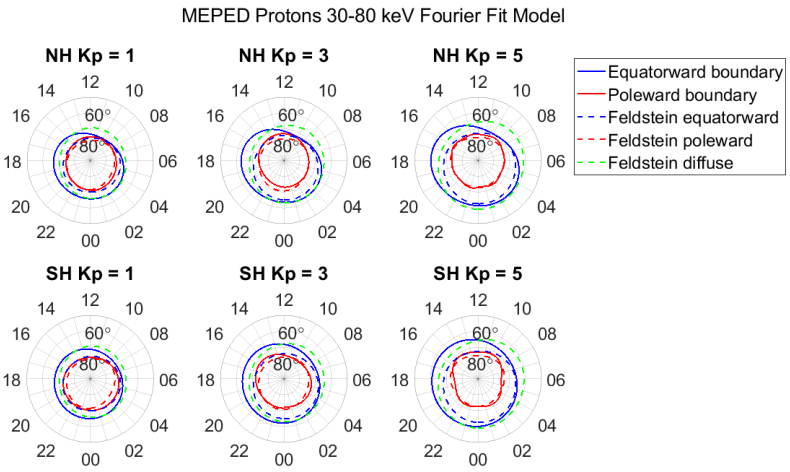

Figure 4.25: The MEPED proton auroral ovals determined by the Fourier series model for three different K_p values in the Northern (NH) and Southern (SH) Hemispheres. The dashed lines represent the Feldstein oval boundaries for the same K_p values.

4.5 Isotropic Boundary

Figures 4.26 and 4.27 display the location of the IB detection events in polar MLT-ILAT plots, relative to the poleward and equatorward boundary detections measured by the MEPED electron and proton detectors. The IBs are plotted for three different K_p values, illustrating the evolution of the IB relative to the other boundaries for different levels of magnetic disturbance. Since each boundary detection represents the average detection location within a 0.5-hour wide MLT bin, Figures 4.28 and 4.29 show the same IB detection data with error bars representing the spread in the data within each MLT bin. The length of the error bars is equivalent to one standard deviation.

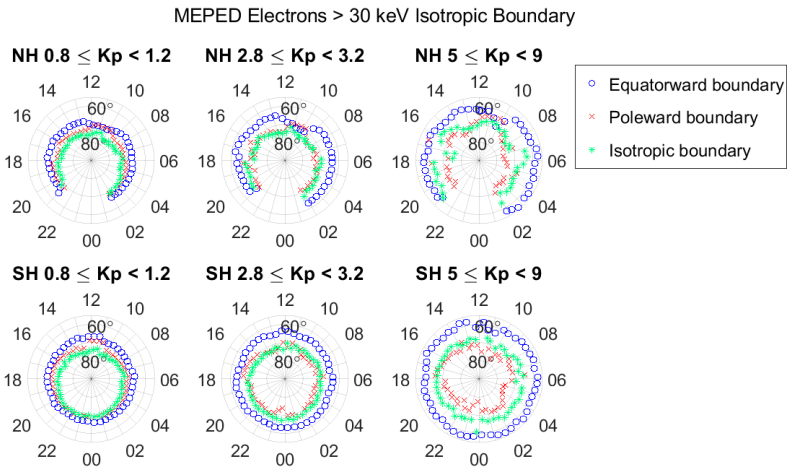

Figure 4.26: The isotropic boundary for electrons detected by MEPED (in turquoise) for three different K_p bins in the Northern and Southern Hemispheres. The boundaries are plotted in an MLT-ILAT polar coordinate system.

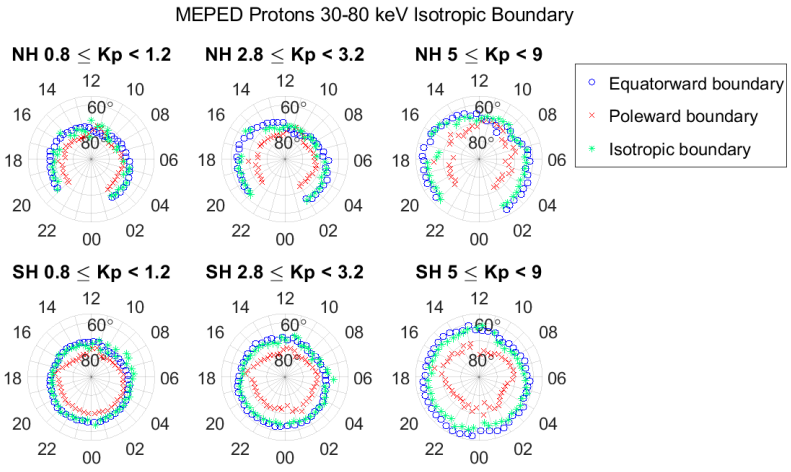

Figure 4.27: The isotropic boundary for protons detected by MEPED (in turquoise) for three different K_p bins in the Northern and Southern Hemispheres. The boundaries are plotted in an MLT-ILAT polar coordinate system.

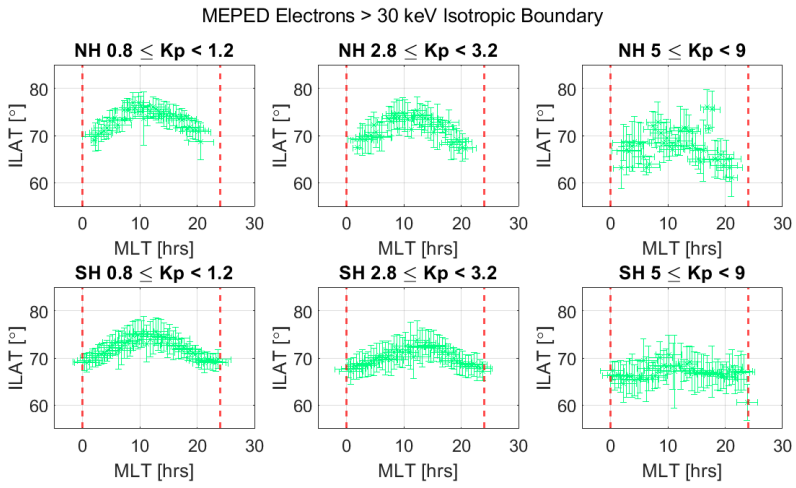

Figure 4.28: The isotropic boundary for electrons detected by MEPED (in turquoise) for three different K_p bins in the Northern and Southern Hemispheres. The error bars represent one standard deviation (in ILAT and MLT, respectively) from the mean.

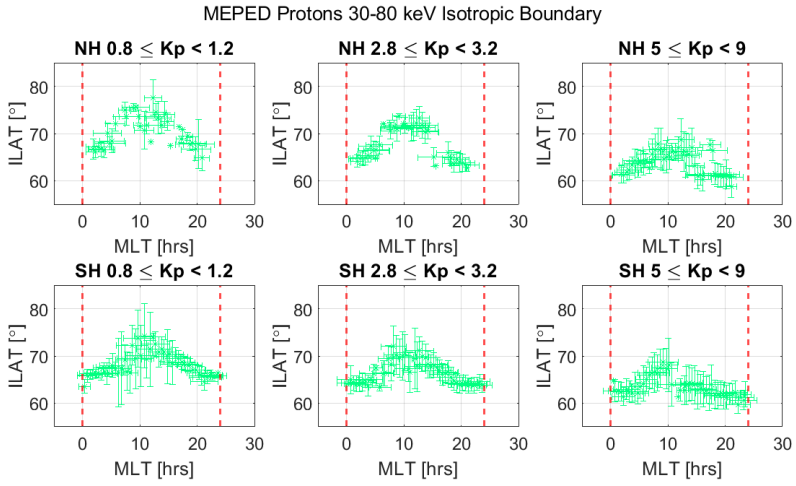

Figure 4.29: The isotropic boundary for protons detected by MEPED (in turquoise) for three different K_p bins in the Northern and Southern Hemispheres. The error bars represent one standard deviation (in ILAT and MLT, respectively) from the mean.

5 Discussion

5.1 Features of the Auroral Oval Boundaries

The mean locations of the equatorward and poleward boundary detections and their respective standard deviations, exhibit a general trend in the observed location of the auroral oval boundary with varying K_p, as illustrated by Figures 4.1 through 4.4. Across all detectors, the equatorward boundaries move equatorwards for increasing K_p, as expected (see e.g. Feldstein and Starkov (1967)). The poleward boundaries show clear variability with the level of magnetic activity. However, the poleward boundary motion differs slightly from detector to detector. The isotropic boundary also shows a clear equatorwards motion with increasing K_p values, as can be seen in Figures 4.28 and 4.29. Across all detectors, the equatorward, poleward and isotropic boundaries show significant standard deviations. for certain detections the standard deviation may be almost 10° in ILAT. A general characteristic is that the standard deviation in ILAT is significantly larger than in MLT. This is due to the choice of narrow MLT bins (only 0.5-hour wide), limiting the spread in the MLT-dimension. The disadvantage of such narrow bins is that it limits the number of data points within each bin, which may further increase the standard deviation in ILAT. As expected, the standard deviations, particularly in ILAT, are significantly larger for the last K_p bin ($5 \leq K_p < 9$). Since this is a large bin, spanning five different K_p values, the spread in the location of the respective boundaries is significantly larger compared to the narrower K_p bins.

In the following subsections, the characteristics that are specific to the equa-

torward and poleward boundary detections of each detector, as well as the isotropic boundary, are discussed in more detail.

5.1.1 TED Electron Boundaries

The TED electron oval boundaries represent the low and medium-energy electron precipitation (energy < 20 keV), and consequently provide an indication of the location of the visible aurora in both hemispheres (Kivelson & Russell, 1995). In the Northern Hemisphere, Figure 4.1 shows the equatorward boundary to be located at approximately 65° ILAT around midnight MLT, approaching 75° ILAT around noon, for low levels of magnetic disturbance. Under the same conditions, the poleward boundary is located approximately between 70° ILAT and 80° ILAT. This is in line with one of the early descriptions of the auroral ovals by Akasofu (1968) for low and moderate levels of magnetic activity (see Chapter 2). As the K_p increases, the equatorward boundary expands equatorwards (by almost 10° ILAT on the nigthside), while the poleward boundary moves only a few degrees towards the equator. This increases the width of the auroral oval significantly on the nightside, while the width remains relatively constant on the dayside. This behaviour is in agreement with the general description of the auroral oval provided by Kivelson and Russell (1995).

In the Northern Hemisphere, Figure 4.1 clearly indicates an unexpected dip in the ILAT of the poleward boundary detections around noon MLT, from almost 80° to 70° during low levels of magnetic activity (and extending even further during active conditions). This is not a common feature of the auroral oval. However, the error bars for the unexpectedly low detections are significantly larger than those belonging to other detections. Evaluating Figure 3.7, it is possible to see that the TED electron detector, measures poleward boundary detections over a very wide ILAT range, overlapping almost all equatorward boundary detections between MLT 10 and 12. Given the results presented in Figure 4.1, it is fair to assume that the same problem arises for several K_p bins. This could suggest that the TED detector on the satellite covering this particular MLT region is faulty, for instance because it has degraded over time. However, if this was the case, a similar problem would likely have been observed in the Southern Hemisphere as well.

The auroral oval in the Southern Hemisphere shows similar characteristics as its northern counterpart. During quiet conditions, the equatorward boundary is located between 65° and 70° ILAT, while the poleward boundary varies between approximately 70° ILAT at midnight and 80° ILAT at noon. For more disturbed conditions, the equatorward boundary expands to almost 55° ILAT at midnight MLT, while the location of the poleward boundary remains predominantly constant (however, the uncertainties in ILAT increase significantly). In contrast

to the boundary detections in the Northern Hemisphere, the equatorward boundary reaches its maximum ILAT around MLT 15. This feature is present for all three K_p bin examples in Figure 4.1. Consequently, this indicates a general asymmetry between the shape of the auroral ovals in Northern and Southern Hemispheres.

5.1.2 TED Proton Boundaries

The proton ovals with particle energies < 20 keV, are shown to be very narrow, as Figure 4.2 indicates. The equatorward and poleward boundaries are located very closely together. For low levels of magnetic activity in the Northern Hemisphere, the oval is located just above 65° ILAT at midnight MLT and just below 80° ILAT at noon. The boundary detections in the Southern Hemisphere show a similar pattern. However, the oval as a whole seems to be located slightly further polewards in Southern Hemisphere. During disturbed magnetic conditions, the oval widens around midnight MLT, while remaining narrow around noon. Furthermore, for high K_p values, the auroral oval as a whole expands towards the equator, the poleward boundary being located close to 70° ILAT and the equatorward boundary shifting to 60° ILAT at MLT 00.

Based on these observations, the TED proton measurements may be described as a narrow band of proton precipitation within the medium-energy (< 20 keV) electron oval. This corresponds well to the simplified high-latitude particle precipitation regions described by Kivelson and Russell (1995). The aurora producing ions (protons) coincide with the electron auroral oval, although the proton precipitation region is shifted slightly towards the dusk side (MLT 18) with respect to the electron oval (see Figure 2.3).

5.1.3 MEPED Electron Boundaries

Although Kivelson and Russell (1995) argue that electrons with energies > 30 keV are not directly associated with auroral emissions, it is still worthwhile to discuss the precipitation pattern of the these electrons. For low levels of magnetospheric disturbance, Figure 4.3 shows the precipitation zone to be a narrow almost circular region, located at approximately 70°. For increasing K_p the region widens, as the equatorward boundary expands to just below 60° ILAT and the poleward boundary moves a few degrees polewards. This characterization applies to both hemispheres. At higher K_p values in the Northern Hemisphere, a few equatorward boundary detections around local midnight are 5° to 10° further north than the boundary detections for adjacent MLT bins. However, these detections have sufficiently large uncertainties to assign the cause of this unexpected observation to poor statistics. Overall, the loca-

tion of the energetic electrons correlates well with the idealized precipitation regions for high-energy auroral particles (energies > 20 keV), presented by Hartz (1971). Figure 2.3 indicates this region to be located on a circular band at constant latitude.

5.1.4 MEPED Proton Boundaries

For low levels of magnetic activity, Figure 4.4 indicates the protons with energies < 30 − 80 keV to be located between 65° ILAT and 75° ILAT. At local midnight, the equatorward boundary is located at approximately 65° ILAT and the poleward boundary is just above 70° ILAT. Around MLT 10, the two boundaries approach each other around 75° ILAT. As K_p increases, the poleward boundary shifts towards a circle of constant latitude just polewards of 70° ILAT. The equatorward boundary remains shifted towards the night side, while expanding equatorwards to about 65° ILAT at local noon and to well below 60° ILAT on the nightside. These features of the energetic proton precipitation apply to both hemispheres. In the highest K_p bin in the Northern Hemisphere, the poleward boundary seems to decrease unexpectedly in ILAT at local noon. However, this may likely be attributed to the high uncertainties around noon in this particular K_p bin.

Although more energetic and with a wider precipitation zone than the TED protons, the MEPED protons are still part of the proton population associated with auroral emissions (in general, proton energies < 1 MeV) (Kivelson & Russell, 1995). Consequently, the precipitating protons detected by MEPED may be associated with the same precipitation region as the TED protons, as presented in 2.3.

5.1.5 Isotropic Boundary

The location of the isotropic boundary for electrons > 30 keV seems to move from just inside the poleward boundary to being located just equatorwards of the poleward boundary, as K_p increases from quiet geomagnetic conditions to disturbed conditions. However, as Figure 4.26 illustrates, for the energetic protons, the IB seems to coincide with or be located just northwards of the equatorward boundary. For the electron and proton IBs these observations seem to be applicable for both hemispheres. This means that the IB expands and contracts along with the equatorward boundary, as a result of varying levels of magnetic disturbance. Although data is missing around midnight MLT, in the Northern Hemisphere the IB is located further polewards, particularly on the morning side around noon. For lower levels of magnetic disturbance, the electron IB in the Northern Hemisphere is located at approximately 70°

ILAT at MLT 00 and at 75° ILAT at MLT 12. The proton IB is located sightly further equatorwards for lower K_p values, varying between 65° at MLT 00 and 75° around noon local time. Similar characteristics may be observed for the electron and proton IBs in the Southern Hemisphere. These observations are in line with the IB characteristics presented by Ganushkina et al. (2005).

There is a significant spread in the IB detection data, comparable to the equatorward and poleward boundary detections. The largest uncertainties are observed in ILAT for the last and widest K_p bin. This is most likely due to IB detections over a large K_p ranges being binned together into the same K_p bin. The standard deviation is relatively consistent among the hemispheres and particle species, with maximum deviations varying from 2.5° to 2.8°. For protons the maximum standard deviation in ILAT is limited to 4.7° in the Northern Hemisphere and 5.6° in its southern counterpart. For electrons, however, the maximum standard deviations are significantly larger, measuring 6.4° and 7.8° in the Northern and Southern Hemispheres, respectively. Nevertheless, by considering the error bars in Figures 4.28 and 4.29, the proton IB shows particularly large spreads in ILAT around MLT 12 for lower K_p bins in the Southern Hemisphere. Although the standard deviations are significant for higher K_p values, the IB is relatively well defined in both hemispheres for lower levels of magnetic disturbance.

5.2 Hemispherical Differences

The data coverage provided by the POES/MetOP satellites is important to take into account when comparing the auroral ovals in the Northern and Southern Hemispheres. As Figures 3.7 and 3.8 illustrate, the six satellites cover all MLTs in the Southern Hemisphere, but do not pass over a four-hour wide MLT region centred at local midnight in the Northern Hemisphere. Despite providing good data coverage for all other MLTs in the Northern Hemisphere, this particular feature of the satellites' orbits is likely to have an effect on the functions that were fitted to the data. In particular, the data gap must be taken into account when comparing the auroral ovals in the two hemispheres.

Among the four detectors, the TED electron detector showed the most prominent difference in the shape of the auroral ovals between the Northern and Southern Hemispheres. The other three detectors did also show minor variations in the poleward and equatorward boundary detections between the hemispheres, for instance the oval being located at slightly lower latitudes in one of the hemispheres. However, these differences were in most cases not larger than the uncertainties involved. Nevertheless, the visible auroral ovals associated with electron energies below 20 keV, did show a clear asymmetry

in terms of where the equatrward boundary was located furthers towards the pole.

5.3 Limitations of the Models

5.3.1 Polynomial Model

The polynomial model has a number of apparent advantages and caveats. Firstly, a major advantage of the model is that it is relatively simple both in development and implementation. However, a high order polynomial is necessary to describe the shape of the oval accurately. Any polynomial lower than fourth order was found to insufficiently incorporate latitudinal variations of the oval boundaries over MLT. This led to another problem with the model, which arguably is its largest weakness: the discontinuity at MLT 00. For all detectors and particularly for the equatorward boundary, the oval is disconnected at midnight local time. Since the polynomial fit is not periodic, it does not take into account that MLT 00 and MLT 24 represent the same location and that the corresponding ILAT of a given boundary should also be the same. As mentioned in Chapter 3, the initial polynomial fits were carried out on two successive boundary detection data sets (centred on one of the data sets), in order to eliminate major discontinuities at MLT 00. However, it was found that if more of the same data sets were plotted in succession, more of the variation in ILAT was averaged out over a 24-hour MLT period. This would require even higher order polynomials to accurately describe the shape of the oval boundaries, increasing the computational complexity of the model. Consequently, there was a trade-off between taking into account longitudinal variations of the oval location and diminishing the nightside discontinuity.

Despite these limitations, in a broad sense, the oval boundaries behave as expected with changing magnetic activity levels. As illustrated by Figures 4.8 through 4.11, the ovals show a significant expansion of the equatorward boundary towards the equator with increasing K_p, for both electrons and proton detectors. The poleward boundary is significantly less fluid than its equatorward counterpart, but for higher K_p values this boundary moves equatorward as well. The lower energy electrons (TED electrons < 20 keV) show the widest auroral ovals, while the TED protons yield the narrowest boundary. None of the ovals display a widening of the oval around local midnight for higher K_p values. In general, all ovals are visually close to circular (disregarding the discontinuity at midnight MLT). This might be caused by the fact that the fourth order polynomial fitted to the data is not able to take into account the highest variations in the boundary location over MLT (see figures in Appendix A.1). The fitted ovals are not accurate enough to take into account the asymmetric

property observed in the boundary detections.

5.3.2 Ellipse Model

Overall, the ellipse model does not provide a good fit to the data. Consider for instance the initial ellipse fit to the boundary detection data illustrated by Figure 4.12 for the TED electron boundaries. The ellipses only partly fit the data, and create some unexpected shapes, such as a widening of the oval towards MLT 6. More severely, Figure B.2 in Appendix B.1 shows an overlap between the equatorward and poleward boundary fits. Once implemented, these characteristics are carried over to the model itself, as Figures 4.15 through 4.18 illustrate. These effects are observed in both hemispheres.

Although the ellipse fit method has the advantage of not incorporating any discontinuities around MLT 00, the orientation of the ellipses seems to be off. This could be caused by an erroneous calculation of either the shift of the ellipse centre relative to the centre of the MLT-ILAT coordinate system (x_0, y_0), or the rotation angle of the ellipse. This suggests that the poor fit was due to the ellipse fitting algorithm that was applied, or an error made when implementing the algorithm. This could potentially act in combination with the significant spread in the boundary detection data. A characteristic feature of the particular ellipse fitting method used was that it would always fit an ellipse, even if the data in question is not accurately described by an ellipse (Fitzgibbon et al., 1999). If the measured oval boundaries are not well described by an ellipse, unexpected boundary estimations could occur. Nevertheless, in general, the auroral ovals are fairly elliptical in nature. Moreover, Xiong and Lühr (2014) did successfully implement an ellipse-based auroral oval model. However, it is not clear which ellipse fitting algorithm was used in this situation. Furthermore, Xiong and Lühr (2014), correlated the ellipse coefficients with the E_m parameter rather than the K_p index.

Despite its apparent shortcomings, in a broad sense, the ellipse model does display the expected response to the increasing K_p values. For both particle species measured by the TED and MEPED instruments, the equatorward boundary expands significantly further towards lower latitudes with increasing K_p values. Similar to the polynomial model, the poleward boundary is more fixed in latitude across various levels of magnetic disturbance. Compared to the polynomial fit approach, the ovals produced by the ellipse fit method are significantly less circular, and display significant differences between the hemispheres. Nevertheless, due to their unexpected orientation, it is hard to tell if this is simply a result of an erroneous calculation, or whether the model in fact incorporates any hemispheric asymmetries.

5.3.3 Fourier Series Model

The initial second order Fourier series fits to the boundary detection data show promising results. Compared to the two other models, the Fourier series fit the data well, as illustrated by Figure 4.19. Particularly for the equatorward boundary, the second order Fourier series fits to all data points except for the boundary detections with the highest ILAT. For the poleward boundary, the boundary detections are significantly more scattered, particularly for the highest K_p bins. The periodic trend in the poleward detection data was less apparent, causing the Fourier series fits to be less ideal. Consider for instance the poleward boundary fit in the Northern Hemisphere for $5 \leq K_p < 9$ in Figure C.3 in Appendix C.1. Here, the periodic variation of the poleward boundary fit is too short. The result of these fits is visible in Figures 4.22 through 4.25. While the equatorward boundary is continuous, the poleward boundary has major discontinuities. This feature is observed in both the Northern and the Southern Hemisphere.

The decision to base this model on a second order Fourier series as opposed to any other order series, was primarily based on the assumption that it should not be too complex and not prone to be significantly affected by any noise or outliers that may be present in the data. A first order Fourier series was ruled out on the basis that it would provide too rough of an estimate of the oval boundaries. Figure 5.1 displays the implementation of the Fourier series model for the TED electron data, using a first order Fourier series ($n = 1$ in Equation 3.20) instead of a second order series. As the figure illustrates, the poleward boundaries look significantly better in terms of discontinuities. However, this was not the case for all detectors, as the first order fit introduced discontinuities in other poleward boundaries where there were previously none, as Figure 5.2 illustrates. Consequently, it was decided to stick with the second order Fourier fit, since it provided the best fits for the equatorward boundary.

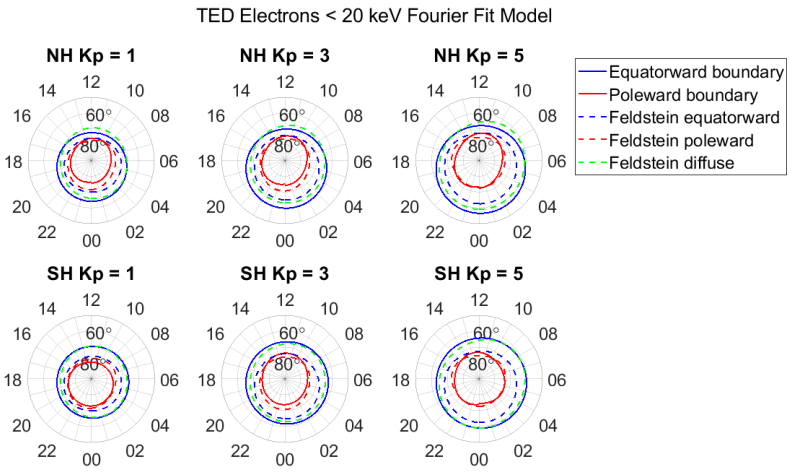

Figure 5.1: First order Fourier series model based on TED electron boundary detections.

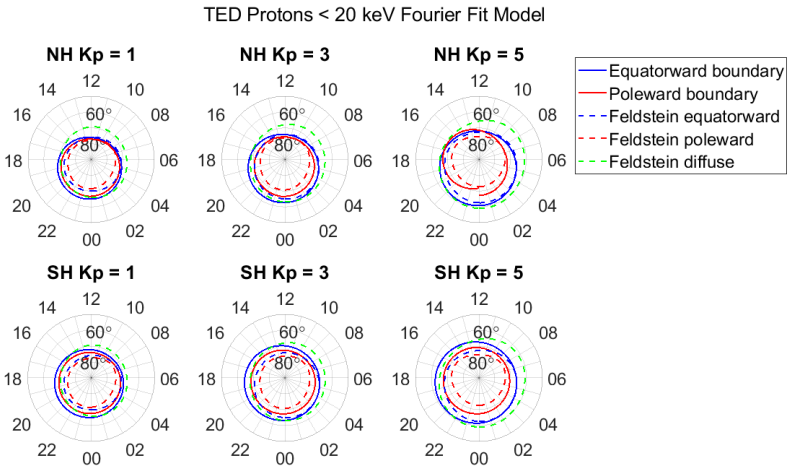

Figure 5.2: First order Fourier series model based on TED proton boundary detections.

The model could be improved by deciding to adjust order of the fitted Fourier series on a case-by-case basis. For instance, the order of the Fourier series could be adjusted to produce the best possible fit, depending on the particle species and energy range. However, this would be significantly more complex to implement than the chosen method.

Whereas hemispherical differences may be hard to distinguish for the poleward

boundary due to the scattered boundary detections, the equatorward boundary does reveal a consistent difference between the auroral ovals between the two hemispheres. Considering the TED electron ovals in Figure 4.22, in the Northern Hemisphere the oval is significantly narrower around noon MLT compared to the corresponding oval in the Southern Hemisphere. For disturbed conditions ($K_p = 5$), the equatorward boundary at MLT 12 in the Northern Hemisphere is located at approximately 70°. In the Southern Hemisphere, however, the equatorward boundary is located at roughly 65° ILAT at MLT 12.

5.3.4 Comparison of the Three Models

It is evident that all three models presented have significant limitations. While the polynomial fit is quick and simple to implement, the resulting boundaries are fairly rough, providing only a general indication of the location of the equatorward and poleward boundaries. It may be argued that higher order polynomials would provide a better fit and minimize the discontinuities on the nightside. However, it turned out that many additional orders of magnitude would be necessary to provide major improvement over the fourth order polynomial used, making implementation impractical. The ellipse model, while having no issues with discontinuities, had the major drawback of not fitting properly to the data and causing equatorward and poleward boundaries to overlap. Finally, while the Fourier model has major discontinuities and is possibly the heaviest to process computationally, it is the only model capable of taking into account the hemispherical difference observed in the TED electron boundary detections. Consequently, while still producing only a rough estimate for the location of the auroral oval, the Fourier series model provides the most advantages compared to its caveats.

5.4 Comparison to the Feldstein Model

Among the oval boundaries observed by each of the four detectors, it is expected that the TED electron boundaries will be most closely related to the oval boundaries predicted by the Feldstein model. As mentioned, electrons with energies < 20 keV represent the majority of the visual aurora, and since the Feldstein ovals are based on optical observations, these two are assumed to correlate. In the following comparison between the new models and the Feldstein oval, the focus will be on the models derived from the TED electron boundary detections. However, comparison plots are provided for the other boundaries as well in Appendices A.3, B.3 and C.3. Figures 5.3, 5.4 and 5.5 display the difference in latitude between the boundaries of the Feldstein model and the polynomial, ellipse and Fourier series models, as a function

of MLT for K_p values of 1, 3 and 5. Boundary comparisons are given for both the Northern (solid lines) and Southern (dashed lines) Hemispheres. For any given boundary comparison in these three figures, a positive deviation indicates that the new model value is equatorwards of the corresponding Feldstein boundary, while a negative value means that the boundary is located polewards of the Feldstein model boundary. The figures consider the following boundary comparisons: poleward-Feldstein poleward, equatorward- Feldstein equatorward and equatorward- Feldstein diffuse. It is important to note that while the difference in latitude is given as ILAT in the figures, the latitude of the Feldstein boundaries is in fact given in CGM coordinates. Consequently, the comparison provided in the figures can only be considered a first order estimate of the difference in location between the boundaries.

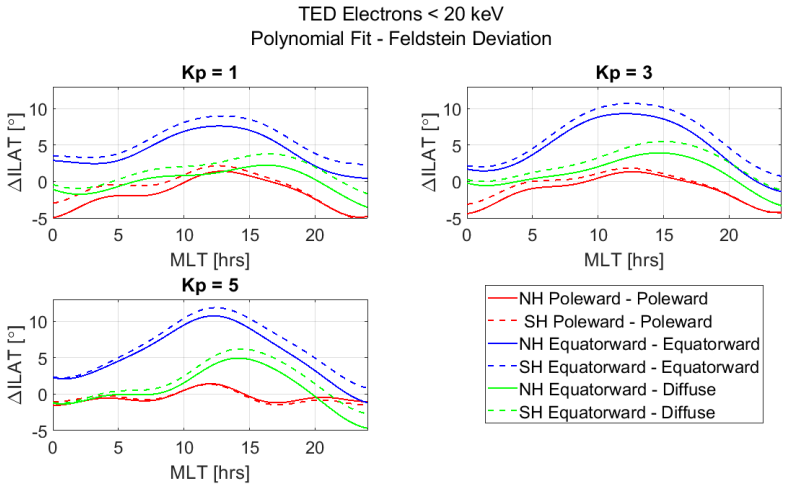

Figure 5.3: The difference in ILAT between the TED electron polynomial fit boundaries and the Feldstein boundaries, for: polynomial poleward and Feldstein poleward (red), polynomial equatorward and Feldstein equatorward (blue) and polynomial equatorward and Feldstein diffuse (green). Solid lines represent boundary comparisons in the Northern Hemisphere (NH) and dashed lines indicate comparisons in the Southern Hemisphere (SH).

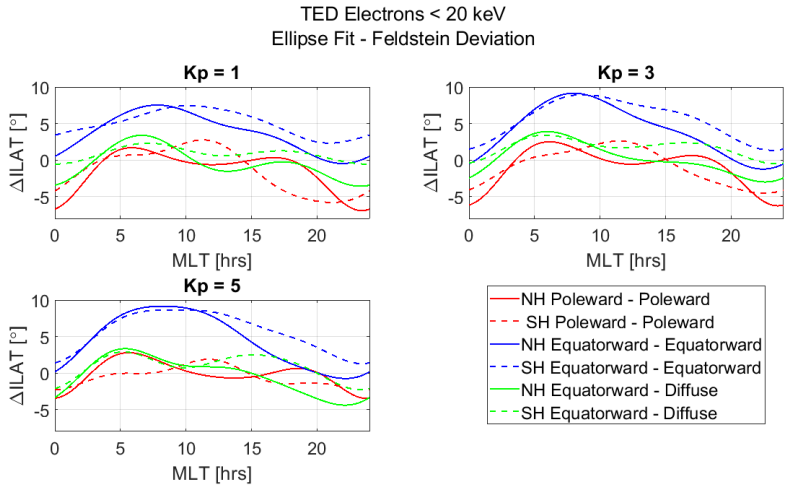

Figure 5.4: The difference in ILAT between the TED electron ellipse fit boundaries and the Feldstein boundaries, for: ellipse poleward and Feldstein poleward (red), ellipse equatorward and Feldstein equatorward (blue) and ellipse equatorward and Feldstein diffuse (green). Solid lines represent boundary comparisons in the Northern Hemisphere (NH) and dashed lines indicate comparisons in the Southern Hemisphere (SH).

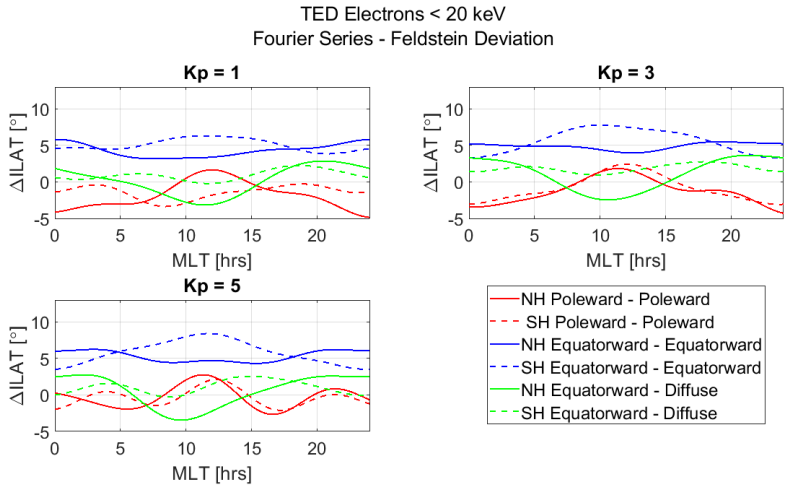

Figure 5.5: The difference in ILAT between the TED electron Fourier series fit boundaries and the Feldstein boundaries, for: Fourier series poleward and Feldstein poleward (red), Fourier series equatorward and Feldstein equatorward (blue) and Fourier series equatorward and Feldstein diffuse (green). Solid lines represent boundary comparisons in the Northern Hemisphere (NH) and dashed lines indicate comparisons in the Southern Hemisphere (SH).

Figure 5.3 shows similar boundary discrepancies in the Northern and Southern Hemispheres. The largest discrepancy may be observed for the equatorward-equatorward boundary comparison in the Southern Hemisphere, where the discrepancy at MLT 12 is almost 12° ILAT. The poleward-poleward and equatorward diffuse boundary comparisons mostly hover within the range of ±5° ILAT, although for $K_p = 5$, the poleward boundaries are very close to each other. Figures 5.4 and 5.5 show similar tendencies. The largest deviation is found in the equatorward-equatorward boundary comparison, while the other two boundaries remain within 5° ILAT of each other. However, for the comparison with the Fourier series model, the poleward-poleward deviation is marginally smaller compared to the other models.

A common characteristic of all the three models is that their respective equatorward boundaries are located significantly further equatorwards compared to the Feldstein equatorward boundary, as illustrated by the large deviations in Figures 5.3 5.4 and 5.5. Since the poleward boundaries correlate much better, the result is that the three models applied in this study estimate the auroral ovals to be significantly larger than does the Feldstein model. The equatorward boundaries seem to coincide with the Feldstein diffuse boundary on several occasions. Since diffuse aurora is associated with particles energies of the order 1 keV to 10 keV (Kivelson & Russell, 1995), which is well within the energy ranges measured by TED, the diffuse aurora is likely to be incorporated into the equatorward boundary detected by the satellites.

The reason why the new models estimate much larger boundaries has likely to do with the chosen flux values designating the edges of the auroral oval. The reason the four applied flux limits were chosen, was because these values were thought to give a realistic description of the expansion of the auroral ovals, given the specifications of the TED and MEPED instruments (Evans & Greer, 2004). Choosing higher boundary values may have yielded smaller ovals that corresponded more strongly with the Feldstein ovals. However, in such a case, the measured oval boundaries might not correspond to the actual auroral particle precipitation region.

Given that the data and techniques used to develop the models applied here and the Feldstein model are vastly different, it is to be expected that discrepancies are observed. One model is based on low-Earth orbit satellite particle detections, and the other on ground-based optical observations. In both cases, the data on which the models are based was collected over a period of roughly one year, and more than 50 years apart. Consequently, Feldstein's optical observations from 1957-58 and the POES/MetOp data set from 2012 are likely to be affected by the general level of magnetosphere activity during those years.

Figure 5.6 shows the average sunspot number and the point in the 11-year solar

cycle at which the respective data sets were collected. The sunspot number is a common measure of solar activity, and through the interaction between the solar wind and the magnetosphere, provides an indication of how much magnetic disturbance may be expected (Fortescue et al., 2011). Both data sets were collected close to solar maximum. However, between 1957 and 1958, the sunspot number was between 250 and 300, while the sunspot number was closer to 100 in 2012. This suggests that more geomagnetic disturbances might have occurred at the time Feldstein made his observations. Nevertheless, it is likely that the method by which the respective data was collected had the greatest effect on the predicted locations of the auroral oval boundaries, as this is the area where the models differ the most.

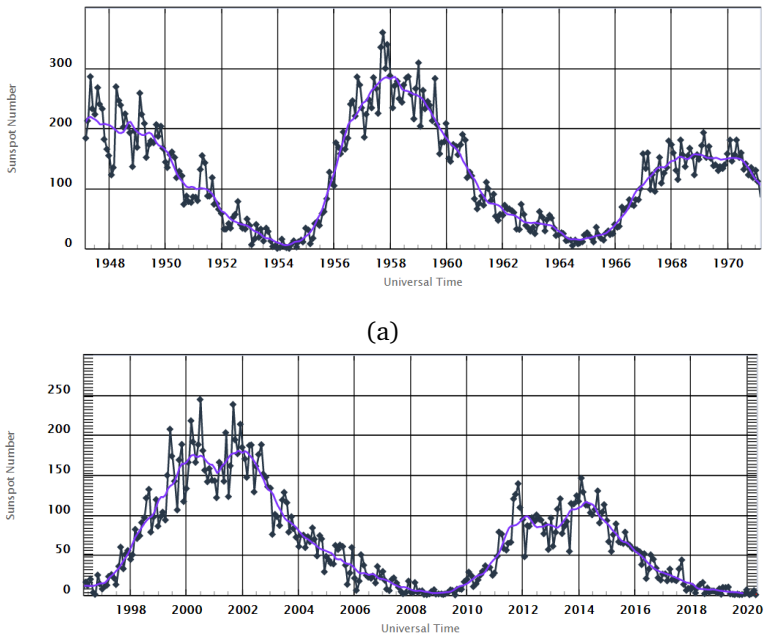

Figure 5.6: The sunspot numbers in (a) the 1950s and 1960s, and (b) in the 2000s and 2010s, illustrating the point in the solar cycle at which the data for the Feldstein model (1957-58) and the POES/MetOp data (2012) was collected. From NOAA (2020).

Which model is most suitable is ultimately a question of what the user is interested in. Although the Feldstein model has been around for a long time, it still provides a good indication of where auroras may be observed from the ground, which is manifested by its continued use. The models developed in this master's thesis provide ovals for four different types of auroral particles, separately in the Northern and Southern Hemispheres. Consequently, it provides a more detailed description of auroral particle precipitation zones, as well as

asymmetries between the auroral ovals in the two hemispheres. On the other hand, the new models provide no direct information on where the auroral ovals will be visible from the ground. The POES/MetOp satellites measure the particle precipitation between 800 km and 900 km in altitude. Consequently, these measurements provide no indication regarding the size or location of the auroral oval at altitudes of around 110 km where the peak auroral emissions occur (Brekke, 2013). Any process acting on the precipitating particles between these altitudes may affect the size and shape of the auroral oval. With respect to Aurora Forecast 3D, a translation of the particle precipitation measurements at low-Earth orbit altitudes to auroral altitudes would be beneficial, since the application aims to show where auroras may be observed from the ground.

5.5 Future Work

The 2012 POES/MetOp data set still has unused potential, which may be used to improve the auroral oval models presented in this thesis. For instance an alternative auroral oval model could be based on the distribution of particle and energy flux across the polar regions, rather than defining a fixed boundary for flux. Newell et al. (2009) established a model base on this method, using energy and particle flux measurements from the Defense Meteorological satellite Program (DMSP). While such a model would not directly yield the equatorward and poleward auroral oval boundaries, it would give a insight into the distribution and intensity of the energetic particle precipitation. This could be of interest for further auroral studies. However, in terms of Aurora Forecast 3D, it would be of less interest, since the application is based around discrete poleward and equatorward boundaries.

Rather than defining new models, future attempts may be made to improve and refine the three models introduced here. A first step may be to investigate how well the boundary detections correlate with optically observable aurora, for instance by conducting simultaneous particle and optical measurements using satellites and all-sky cameras. This would provide information on how well the auroral oval boundaries measured by POES and MetOp satellites corresponded to the aurora visible from the ground. Moreover, the issue of the altitude discrepancy between the orbit of the satellites and the aurora may be addressed by converting the boundary detections from the given MLT-ILAT coordinate system into a Magnetic Apex Coordinate system, such as Modified Apex coordinates. This coordinate system is based on the tracing of magnetic field lines (Richmond, 1995), allowing the precipitating particle regions to be mapped to auroral altitudes. Evaluating the auroral ovals as a characteristic auroral altitude (for instance 110 km) could provide a more

accurate comparison to the Feldstein ovals. This would be particularly useful when considering whether the models are applicable for implementation into the Aurora Forecast 3D application software.

6

Conclusion

Three new empirical models for the equatorward and poleward boundaries of the auroral ovals have been developed, utilizing three different fitting functions: a fourth-order polynomial fit, a direct least-squares ellipse fit and a second-order Fourier series fit. All models were based on particle precipitation data collected throughout 2012 by five NOAA-series POES satellites, in addition to EUMETSAT's MetOp-A satellite. All six satellites carried identical TED and MEPED instruments, which were used to measure the flux of four different types of auroral particles: electrons with energies < 20 keV (TED), protons with energies < 20 keV (TED), electrons with energies > 30 keV (MEPED) and protons with energies $30 - 80$ keV. For each of these four detectors, the locations of the equatorward and poleward boundaries of the auroral ovals in both the Northern and Southern Hemisphere were defined. In addition, the 0° and 90° MEPED detectors were used to determine the location of the isotropic boundary for electrons and protons. The auroral oval boundaries based on each of the four detectors, as well as the isotropic boundary were found to correlate well with heir respective locations described in the literature. Moreover, the electrons with energies < 20 keV, representing the majority of the particle population causing the visible aurora, displayed an asymmetry between the two hemispheres on the dayside.

For each of the four detectors, the equatorward and poleward boundary detection data was sorted into 15 K_p bins. Each K_p bin was in turn divided into 48 adjacent 0.5-hour wide MLT bins. The mean and standard deviation of the location of the boundary detection within each MLT bin was calculated.

The standard deviation was used as a measure of the spread in the boundary detection data. For each of the four detectors, the boundary detections were processed separately for the equatorward and poleward boundaries in the Northern and Southern Hemispheres. Using the average boundary detections as a basis, each of the three fitting methods used a common procedure: (1) Fitting a function to the data describing a given auroral oval boundary, expressing the ILAT in terms of MLT. (2) Correlating the function coefficients with K_p. (3) Calculating the function coefficients for an arbitrary K_p value and implement the coefficients in a function describing the ILAT in terms of MLT.

The polynomial fit method was found to be quick and simple to implement, but only provided a rough estimate of auroral oval boundaries, due to discontinuities in the boundaries around MLT 00. The ellipse fit model did not provide a good fit to the boundary detection data, and estimated overlapping poleward and equatorward boundaries for certain K_p values. The Fourier series fit proved to be the most promising model, despite also having issues with discontinuities around midnight local time. Among the three model, only the Fourier series models Incorporated the hemispherical differences observed in the TED electron boundary detections.

The poleward boundaries of the three models corresponded well with the poleward boundaries predicted by the Feldstein model, the boundaries being located within $\pm 5°$ of each other. The equatorward boundaries estimated by the new models deviated by as much as $\pm 10°$ from the equatorward boundary predicted by the Feldstein model. In fact, the equatorward boundaries of the new models showed stronger correlation with the Feldstein diffuse boundary. Consequently, the auroral ovals predicted by the new model were significantly larger than ovals predicted by the Feldstein model.

Compared to the Feldstein model, the new models had the advantage of incorporating hemispherical differences. Furthermore, the new models provided a more detailed overview of the precipitation zones of the different auroral particles. However, the models provided no information regarding the parts of the auroral oval that are visible from the ground. This problem is partly due to the fact that the new models define the auroral oval at the orbital altitudes of the satellites ($800 - 900$ km), whereas the Feldstein model is purely derived from ground-based optical observations. For auroral forecasting software such as Aurora Forecast 3D, it is of interest to provide a prediction for where the aurora may be visible from the ground. This issue may be addressed by mapping the particle precipitation-based ovals down to auroral altitudes. This may be a topic for future research.

A

Polynomial Fit Figures

A.1 Initial Fits to Data

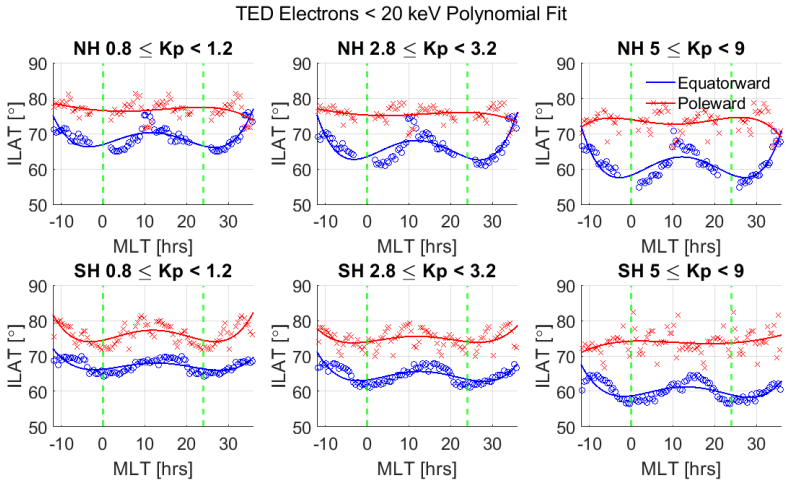

Figure A.1: Fourth order polynomials fitted to the averaged boundary detections from the TED electron detector, for three K_P ranges in the Northern (NH) and Southern (SH) Hemispheres. The vertical dashed line in green represents the region between MLT 00 and MLT 24 within which the polynomial fit is valid.

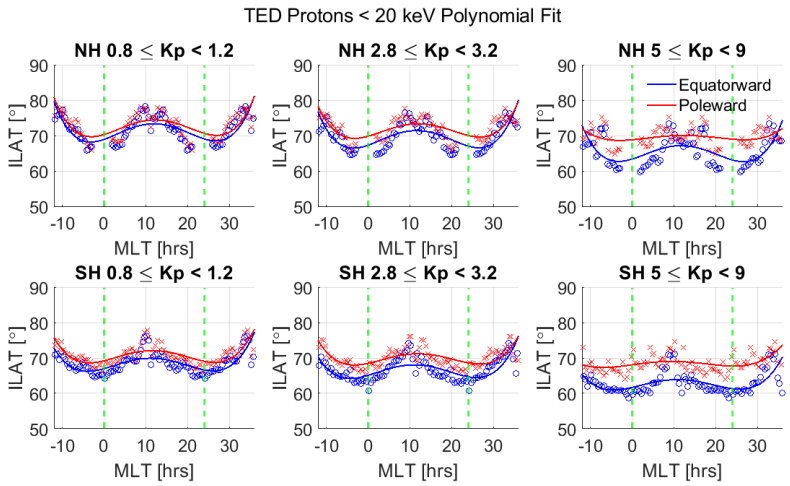

Figure A.2: Fourth order polynomials fitted to the averaged boundary detections from the TED proton detector, for three K_P ranges in the Northern (NH) and Southern (SH) Hemispheres. The vertical dashed line in green represents the region between MLT 00 and MLT 24 within which the polynomial fit is valid.

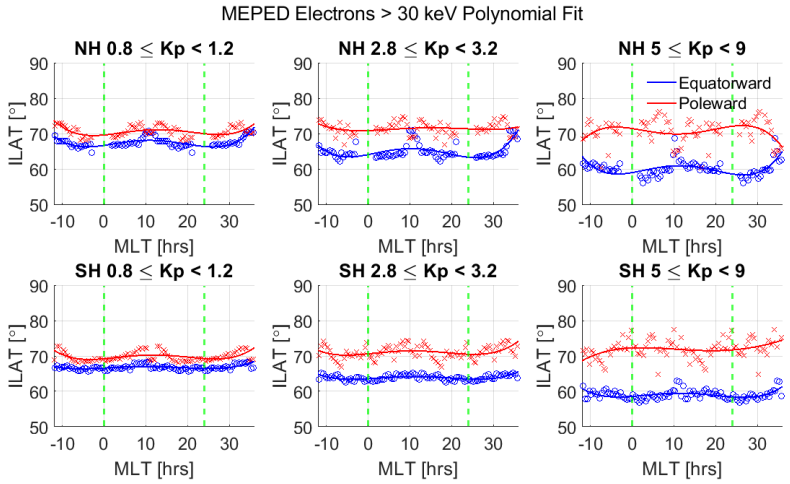

Figure A.3: Fourth order polynomials fitted to the averaged boundary detections from the MEPED electron detector, for three K_P ranges in the Northern (NH) and Southern (SH) Hemispheres. The vertical dashed line in green represents the region between MLT 00 and MLT 24 within which the polynomial fit is valid.

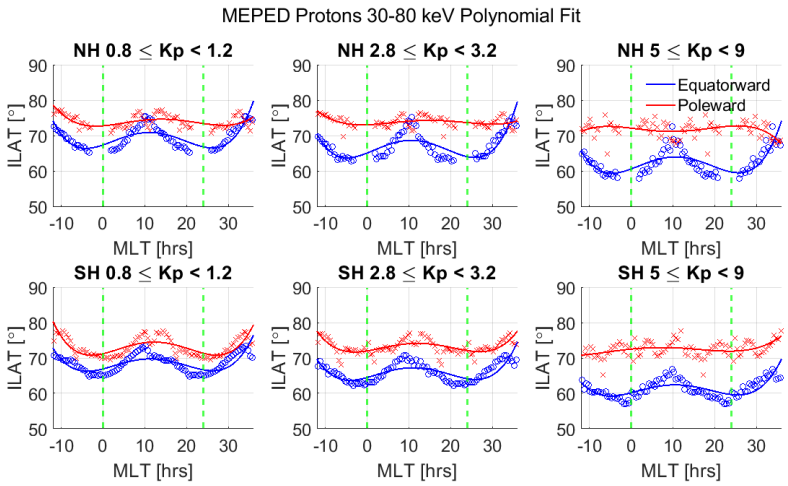

Figure A.4: Fourth order polynomials fitted to the averaged boundary detections from the MEPED proton detector, for three K_P ranges in the Northern (NH) and Southern (SH) Hemispheres. The vertical dashed line in green represents the region between MLT 00 and MLT 24 within which the polynomial fit is valid.

A.2 Correlation Figures

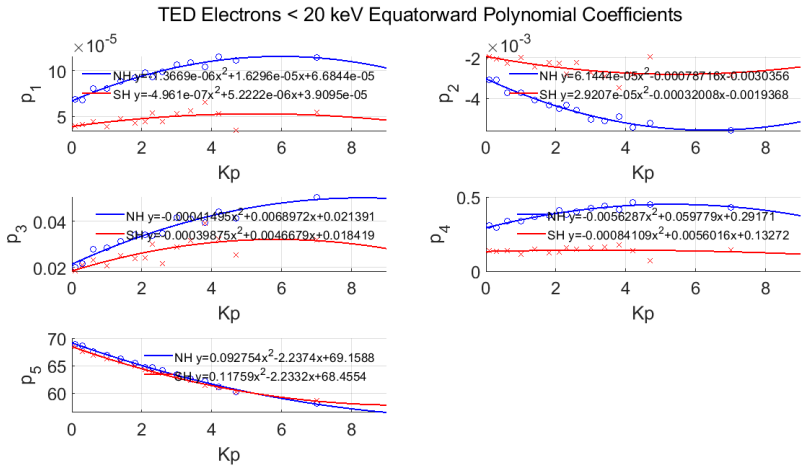

Figure A.5: Second order polynomials correlating the five polynomial coefficients of the TED electron equatorward boundary to K_p, in both the Northern (NH in blue) and Southern (SH in red) Hemisphere.

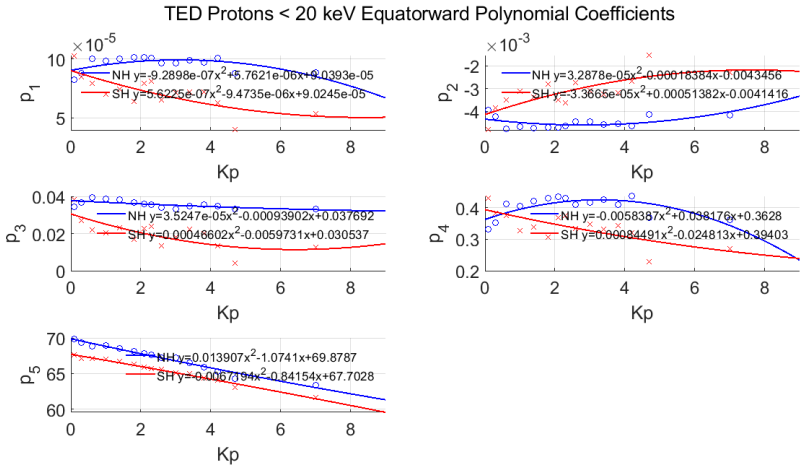

Figure A.6: Second order polynomials correlating the five polynomial coefficients of the TED proton equatorward boundary to K_p, in both the Northern (NH in blue) and Southern (SH in red) Hemisphere.

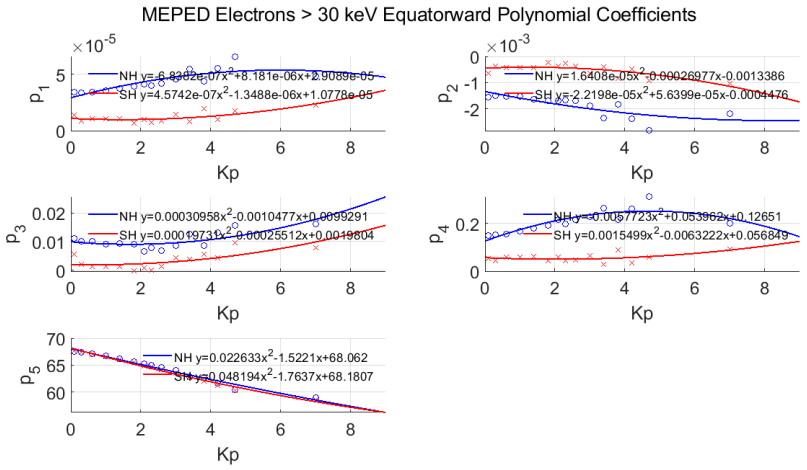

Figure A.7: Second order polynomials correlating the five polynomial coefficients of the MEPED electron equatorward boundary to K_p, in both the Northern (NH in blue) and Southern (SH in red) Hemisphere.

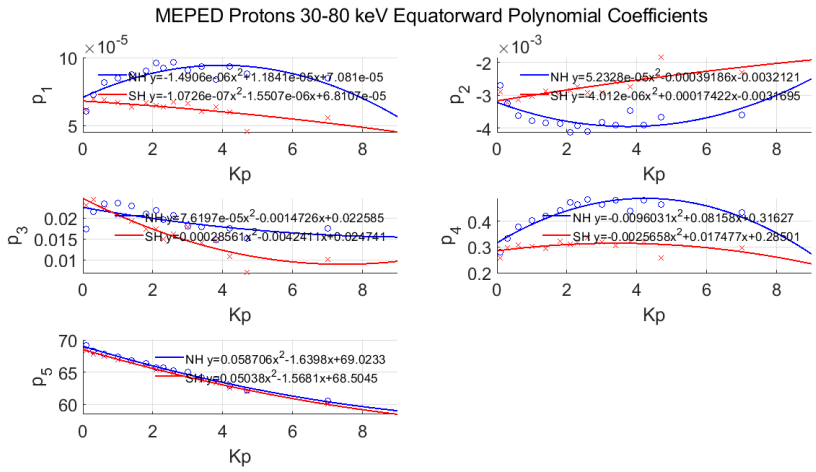

Figure A.8: Second order polynomials correlating the five polynomial coefficients of the MEPED proton equatorward boundary to K_p, in both the Northern (NH in blue) and Southern (SH in red) Hemisphere.

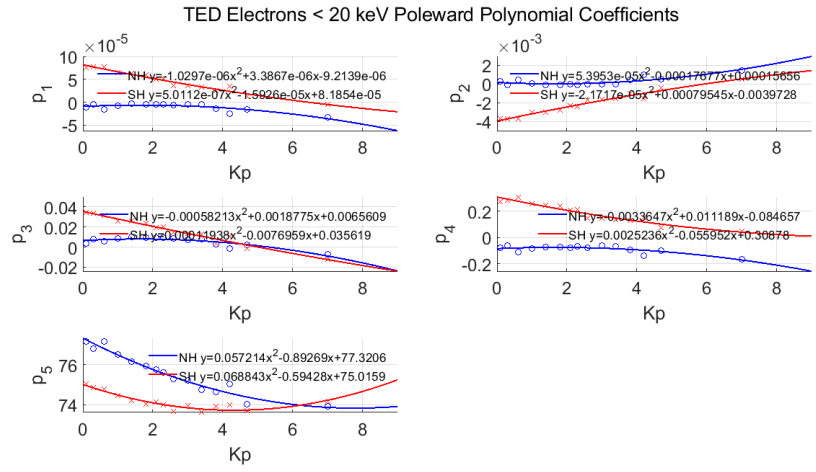

Figure A.9: Second order polynomials correlating the five polynomial coefficients of the TED electron poleward boundary to K_p, in both the Northern (NH in blue) and Southern (SH in red) Hemisphere.

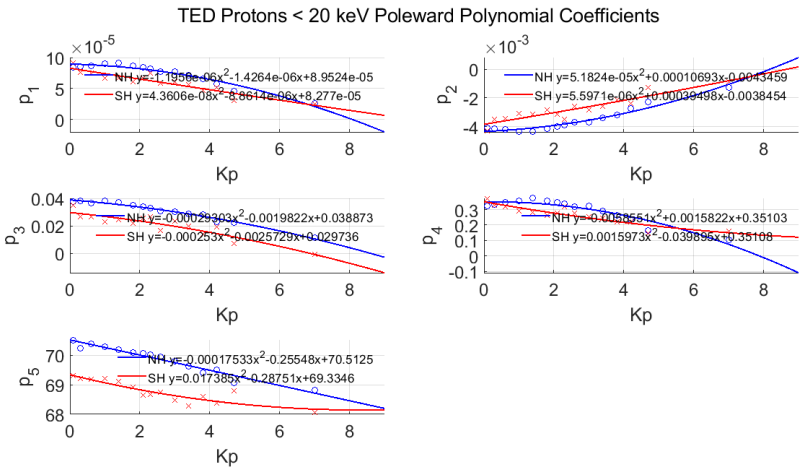

Figure A.10: Second order polynomials correlating the five polynomial coefficients of the TED proton poleward boundary to K_p, in both the Northern (NH in blue) and Southern (SH in red) Hemisphere.

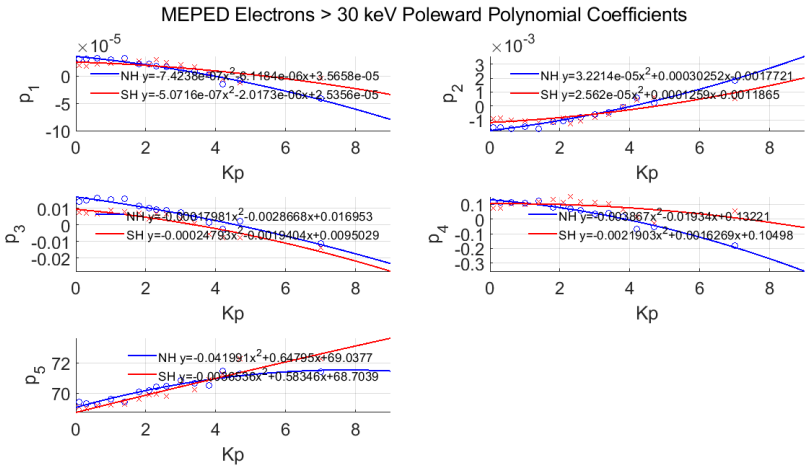

Figure A.11: Second order polynomials correlating the five polynomial coefficients of the MEPED electron poleward boundary to K_p, in both the Northern (NH in blue) and Southern (SH in red) Hemisphere.

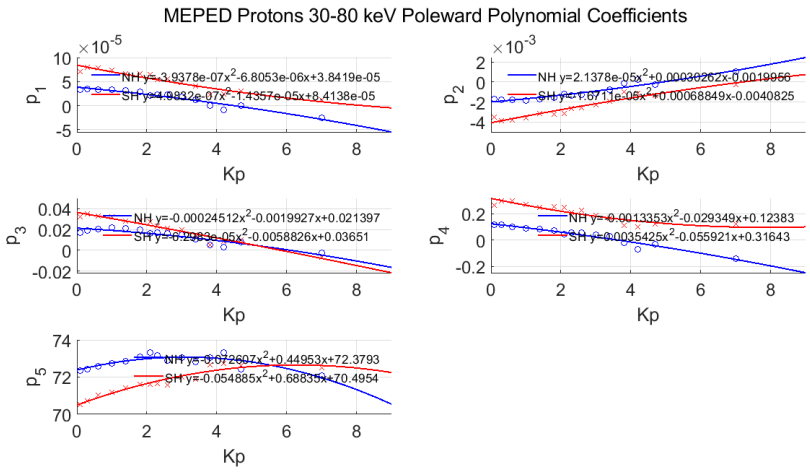

Figure A.12: Second order polynomials correlating the five polynomial coefficients of the MEPED proton poleward boundary to K_p, in both the Northern (NH in blue) and Southern (SH in red) Hemisphere.

A.3 Deviation from the Feldstein Model

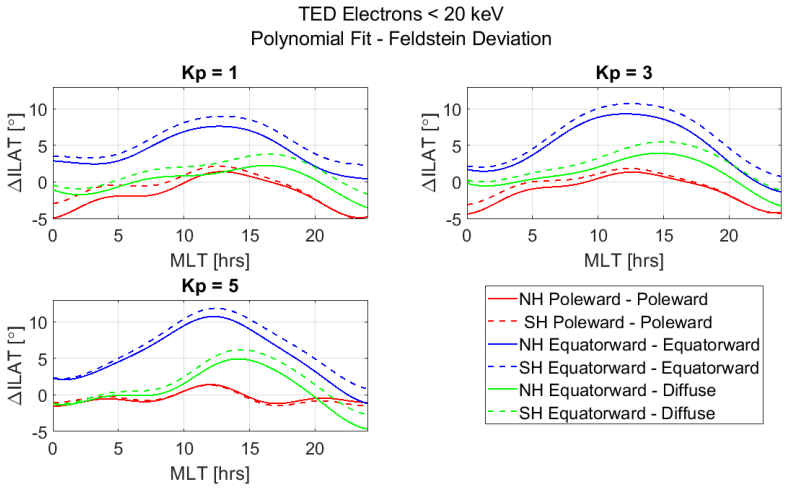

Figure A.13: The difference in ILAT between the TED electron polynomial fit boundaries and the Feldstein boundaries, for: polynomial poleward and Feldstein poleward (red), polynomial equatorward and Feldstein equatorward (blue) and polynomial equatorward and Feldstein diffuse (green). Solid lines represent boundary comparisons in the Northern Hemisphere (NH) and dashed lines indicate comparisons in the Southern Hemisphere (SH).

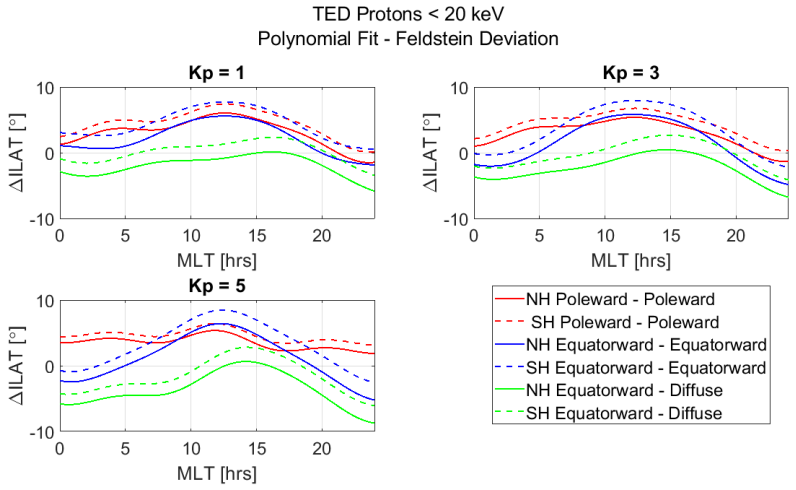

Figure A.14: The difference in ILAT between the TED proton polynomial fit boundaries and the Feldstein boundaries, for: polynomial poleward and Feldstein poleward (red), polynomial equatorward and Feldstein equatorward (blue) and polynomial equatorward and Feldstein diffuse (green). Solid lines represent boundary comparisons in the Northern Hemisphere (NH) and dashed lines indicate comparisons in the Southern Hemisphere (SH).

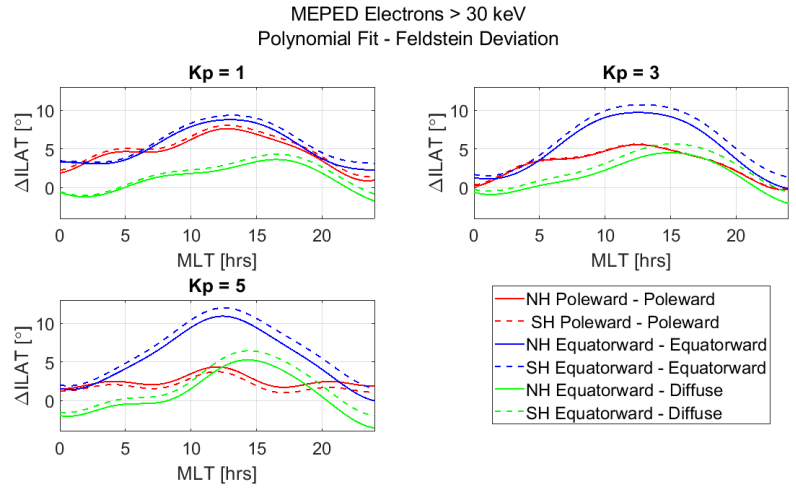

Figure A.15: The difference in ILAT between the MEPED electron polynomial fit boundaries and the Feldstein boundaries, for: polynomial poleward and Feldstein poleward (red), polynomial equatorward and Feldstein equatorward (blue) and polynomial equatorward and Feldstein diffuse (green). Solid lines represent boundary comparisons in the Northern Hemisphere (NH) and dashed lines indicate comparisons in the Southern Hemisphere (SH).

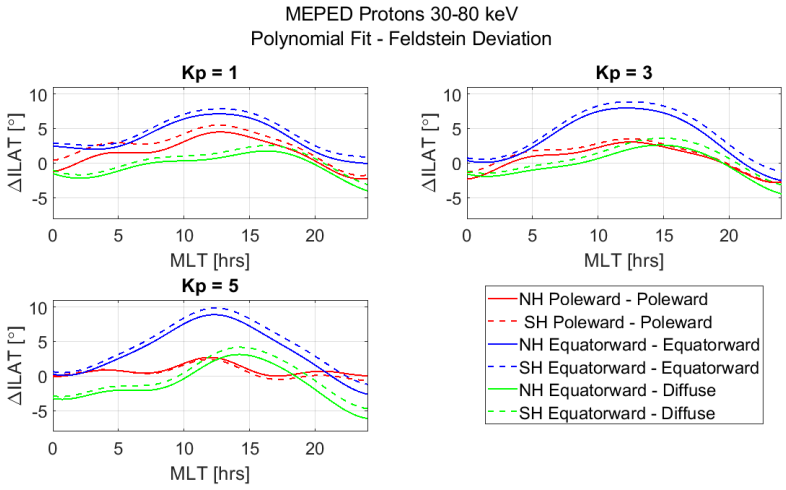

Figure A.16: The difference in ILAT between the MEPED proton polynomial fit boundaries and the Feldstein boundaries, for: polynomial poleward and Feldstein poleward (red), polynomial equatorward and Feldstein equatorward (blue) and polynomial equatorward and Feldstein diffuse (green). Solid lines represent boundary comparisons in the Northern Hemisphere (NH) and dashed lines indicate comparisons in the Southern Hemisphere (SH).

B

Ellipse Fit Figures

B.1 Initial Fits to Data

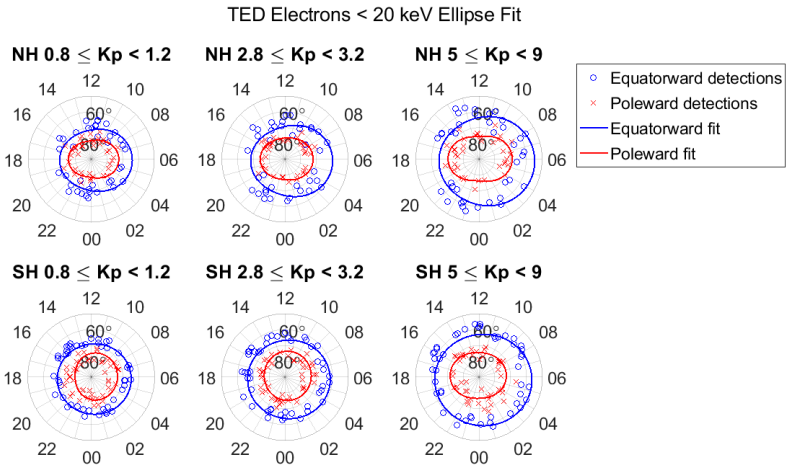

Figure B.1: Ellipses fitted to TED electron boundary detection events, for three K_p ranges in the Northern (NH) and Southern (SH) Hemispheres.

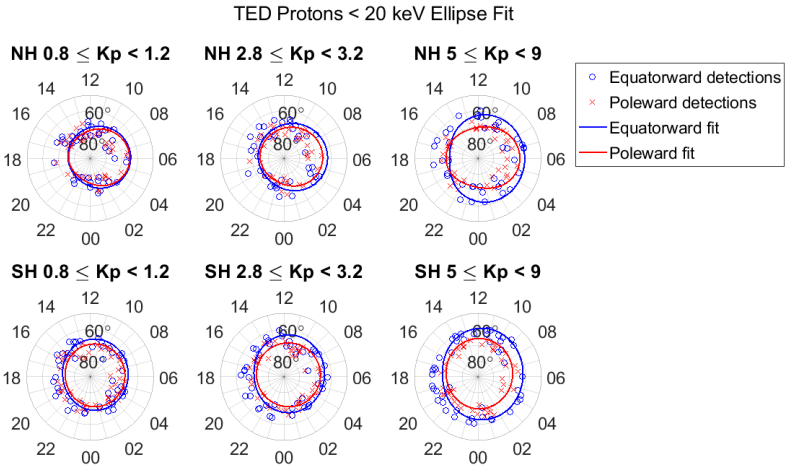

Figure B.2: Ellipses fitted to TED proton boundary detection events, for three K_p ranges in the Northern (NH) and Southern (SH) Hemispheres.

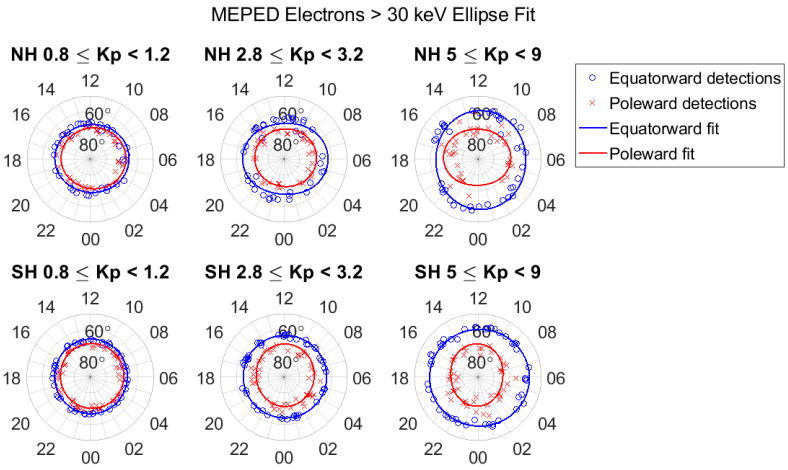

Figure B.3: Ellipses fitted to MEPED electron boundary detection events, for three K_p ranges in the Northern (NH) and Southern (SH) Hemispheres.

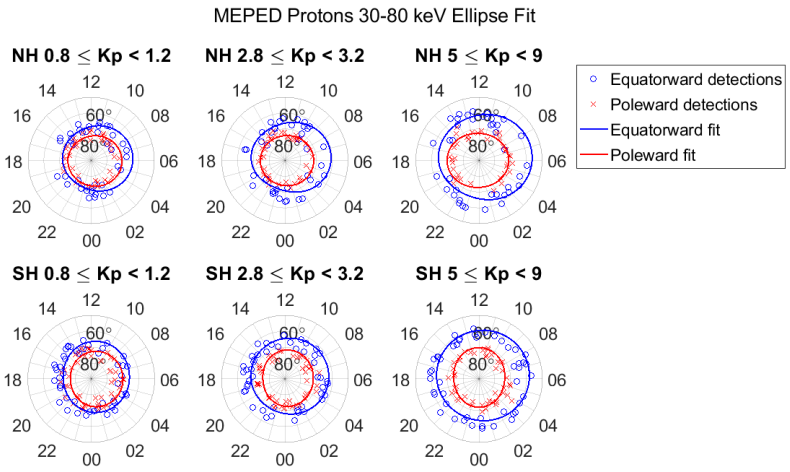

Figure B.4: Ellipses fitted to MEPED proton boundary detection events, for three K_p ranges in the Northern (NH) and Southern (SH) Hemispheres.

B.2 Correlation Figures

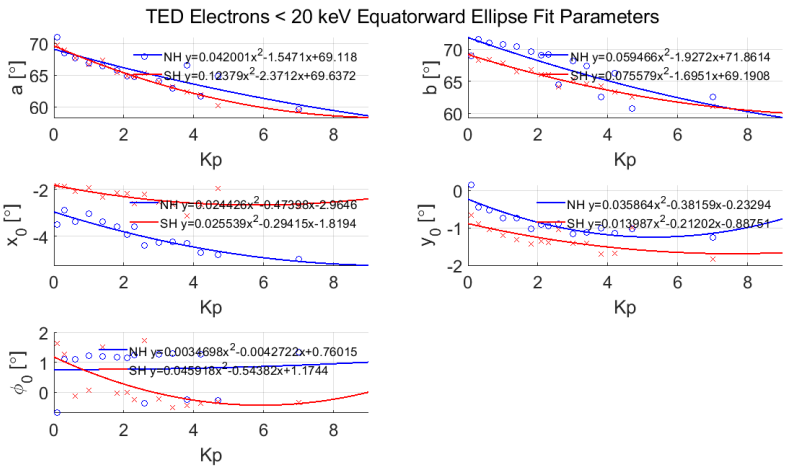

Figure B.5: Second order polynomials correlating the five ellipse parameters of the TED electron equatorward boundary to K_p, in both the Northern (NH in blue) and Southern (SH in red) Hemisphere.

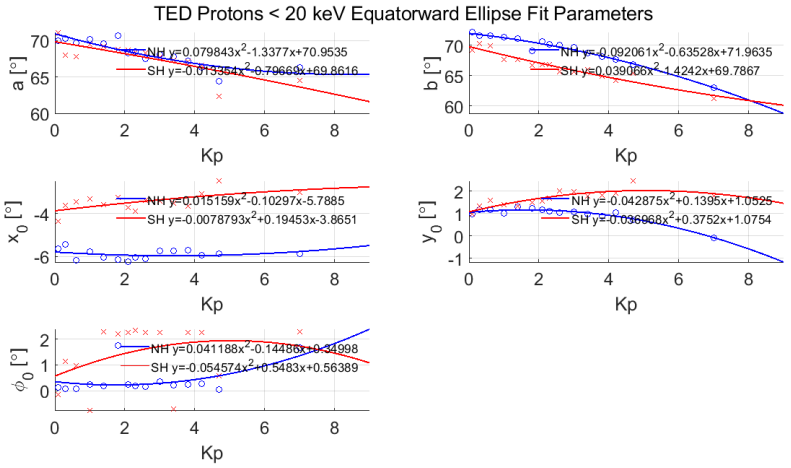

Figure B.6: Second order polynomials correlating the five ellipse parameters of the TED proton equatorward boundary to K_p, in both the Northern (NH in blue) and Southern (SH in red) Hemisphere.

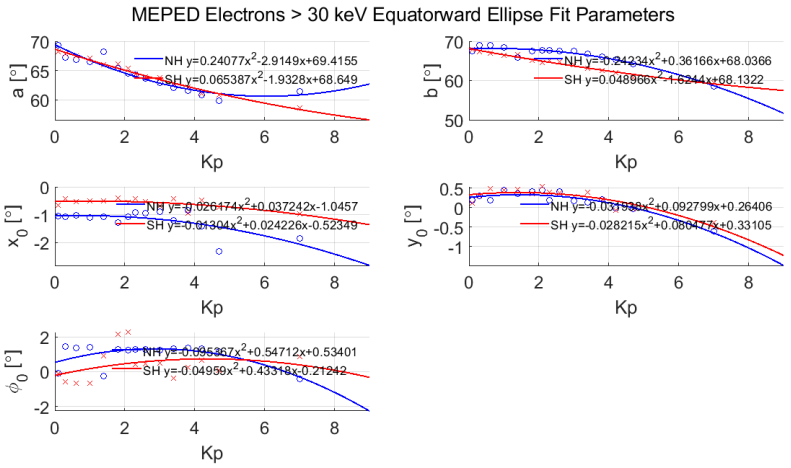

Figure B.7: Second order polynomials correlating the five ellipse parameters of the MEPED electron equatorward boundary to K_p, in both the Northern (NH in blue) and Southern (SH in red) Hemisphere.

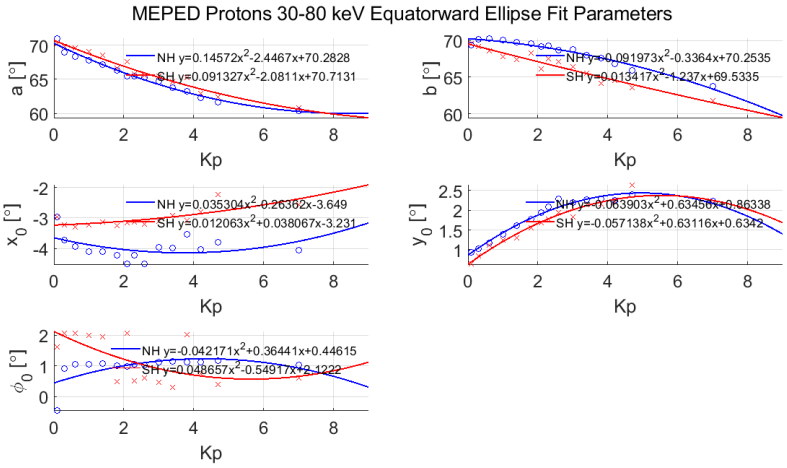

Figure B.8: Second order polynomials correlating the five ellipse parameters of the MEPED proton equatorward boundary to K_p, in both the Northern (NH in blue) and Southern (SH in red) Hemisphere.

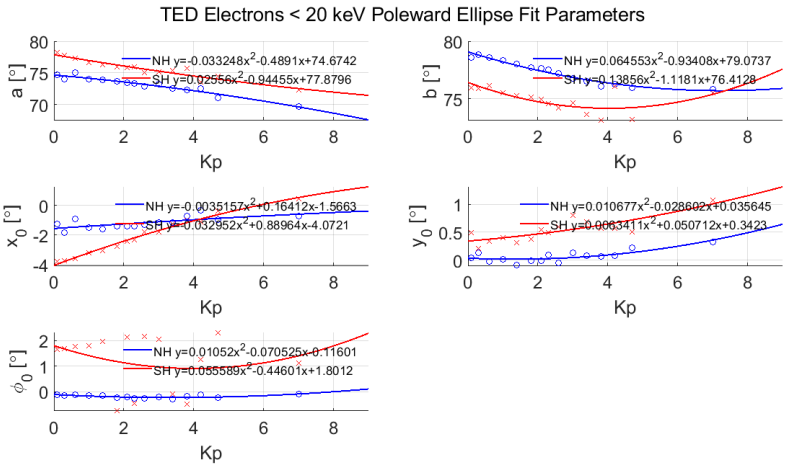

Figure B.9: Second order polynomials correlating the five ellipse parameters of the TED electron poleward boundary to K_p, in both the Northern (NH in blue) and Southern (SH in red) Hemisphere.

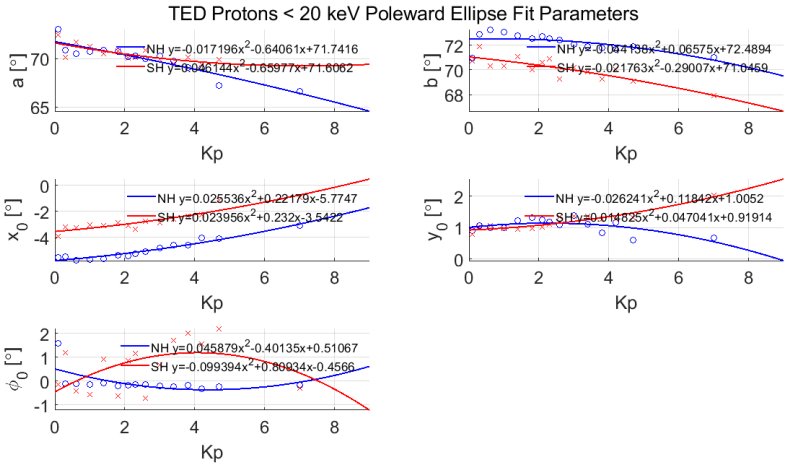

Figure B.10: Second order polynomials correlating the five ellipse parameters of the TED proton poleward boundary to K_p, in both the Northern (NH in blue) and Southern (SH in red) Hemisphere.

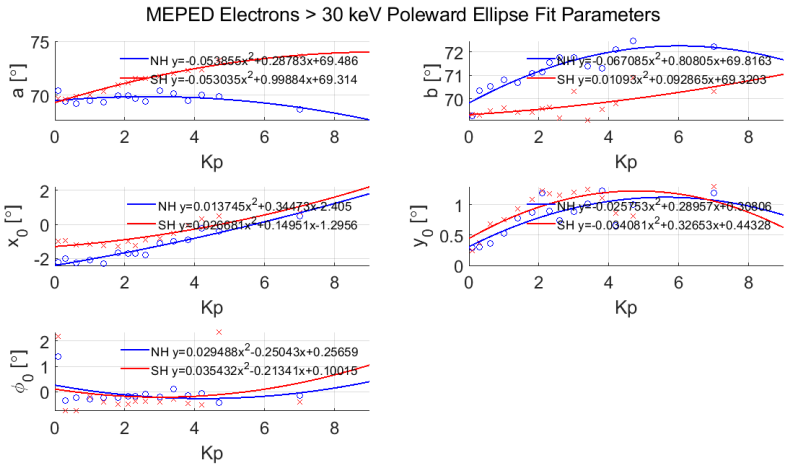

Figure B.11: Second order polynomials correlating the five ellipse parameters of the MEPED electron poleward boundary to K_p, in both the Northern (NH in blue) and Southern (SH in red) Hemisphere.

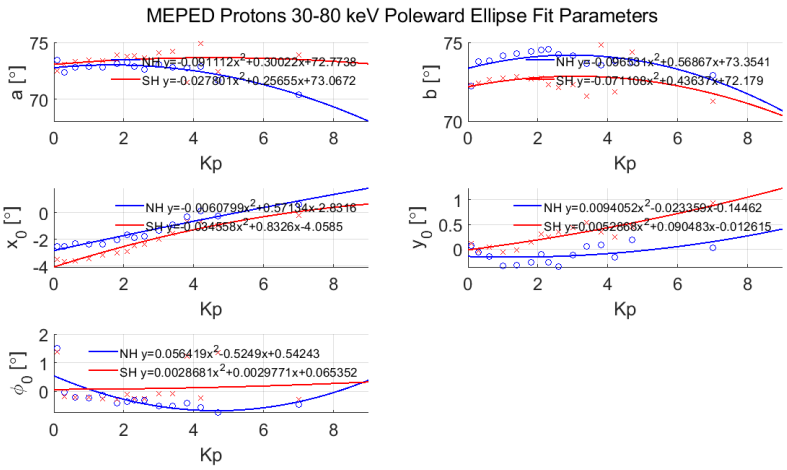

Figure B.12: Second order polynomials correlating the five ellipse parameters of the MEPED proton poleward boundary to K_p, in both the Northern (NH in blue) and Southern (SH in red) Hemisphere.

B.3 Deviation from the Feldstein Model

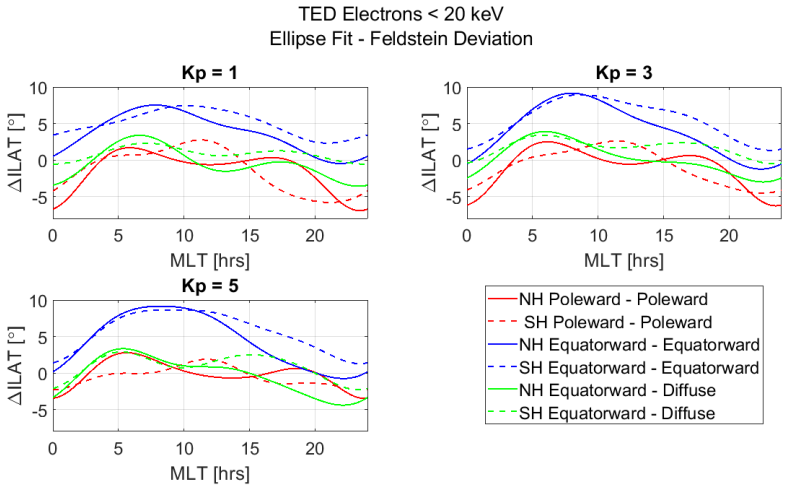

Figure B.13: The difference in ILAT between the TED electron polynomial fit boundaries and the Feldstein boundaries, for: ellipse poleward and Feldstein poleward (red), ellipse equatorward and Feldstein equatorward (blue) and ellipse equatorward and Feldstein diffuse (green). Solid lines represent boundary comparisons in the Northern Hemisphere (NH) and dashed lines indicate comparisons in the Southern Hemisphere (SH).

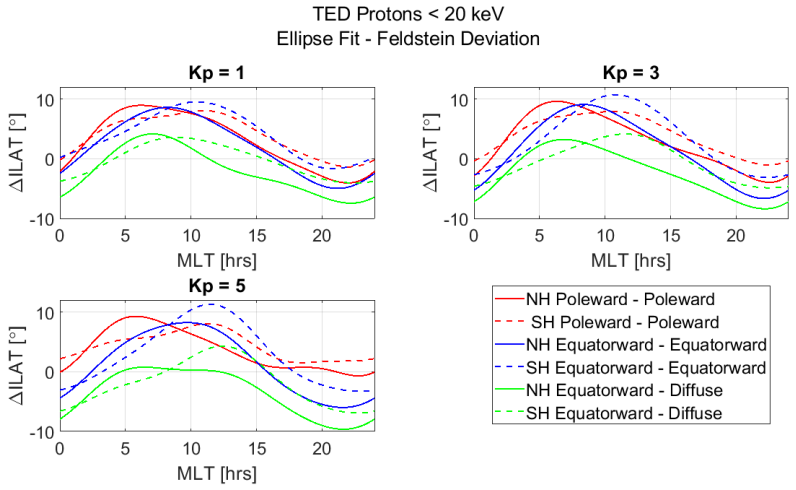

Figure B.14: The difference in ILAT between the TED proton ellipse fit boundaries and the Feldstein boundaries, for: ellipse poleward and Feldstein poleward (red), ellipse equatorward and Feldstein equatorward (blue) and ellipse equatorward and Feldstein diffuse (green). Solid lines represent boundary comparisons in the Northern Hemisphere (NH) and dashed lines indicate comparisons in the Southern Hemisphere (SH).

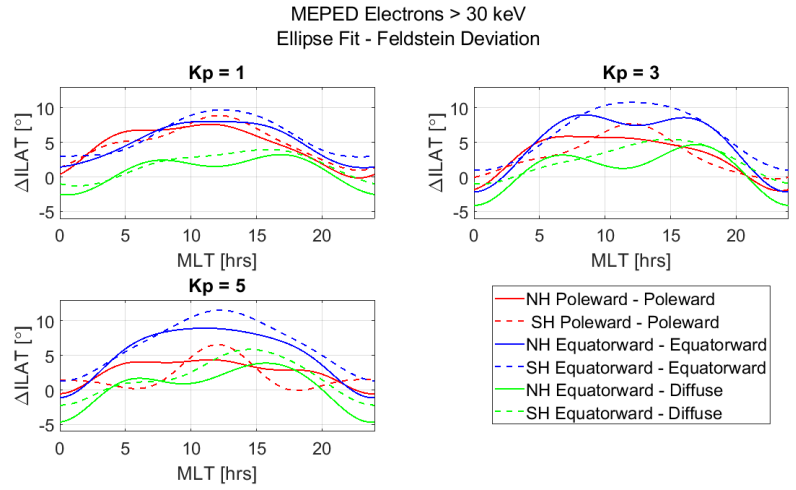

Figure B.15: The difference in ILAT between the MEPED electron ellipse fit boundaries and the Feldstein boundaries, for: ellipse poleward and Feldstein poleward (red), ellipse equatorward and Feldstein equatorward (blue) and ellipse equatorward and Feldstein diffuse (green). Solid lines represent boundary comparisons in the Northern Hemisphere (NH) and dashed lines indicate comparisons in the Southern Hemisphere (SH).

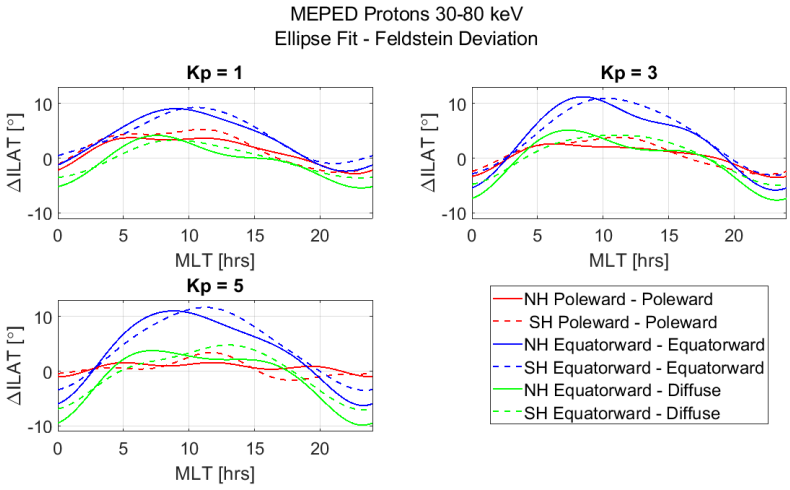

Figure B.16: The difference in ILAT between the MEPED proton ellipse fit boundaries and the Feldstein boundaries, for: ellipse poleward and Feldstein poleward (red), ellipse equatorward and Feldstein equatorward (blue) and ellipse equatorward and Feldstein diffuse (green). Solid lines represent boundary comparisons in the Northern Hemisphere (NH) and dashed lines indicate comparisons in the Southern Hemisphere (SH).

C

Fourier Series Fit Figures

C.1 Initial Fits to Data

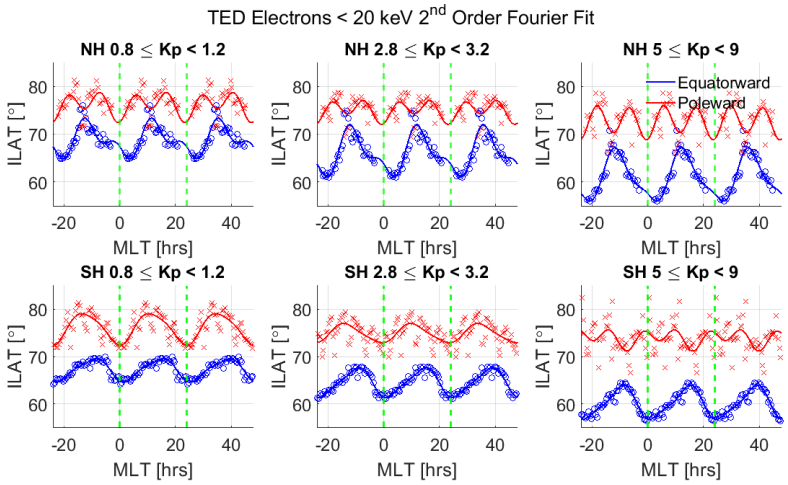

Figure C.1: Fourier series fitted to TED electron boundary detection events, for three K_p ranges in the Northern (NH) and Southern (SH) Hemispheres.

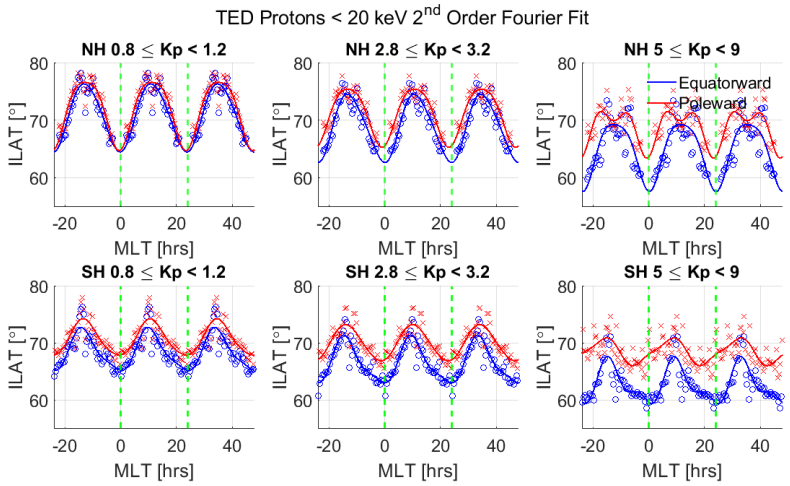

Figure C.2: Fourier series fitted to TED proton boundary detection events, for three K_p ranges in the Northern (NH) and Southern (SH) Hemispheres.

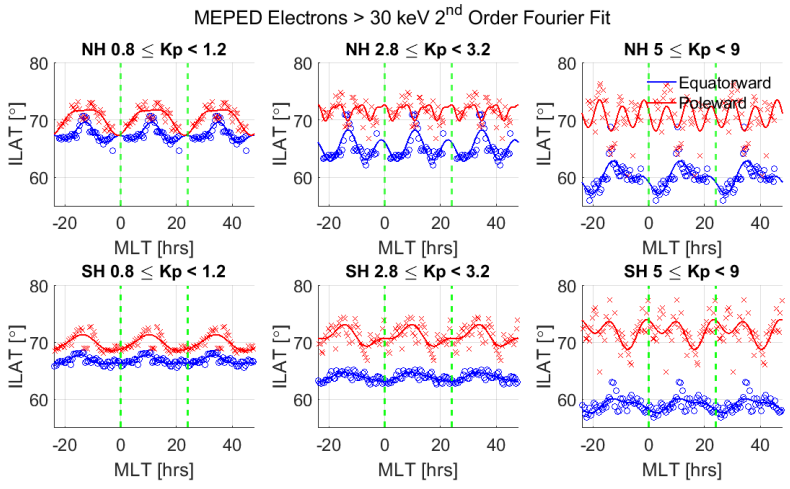

Figure C.3: Fourier series fitted to MEPED electron boundary detection events, for three K_p ranges in the Northern (NH) and Southern (SH) Hemispheres.

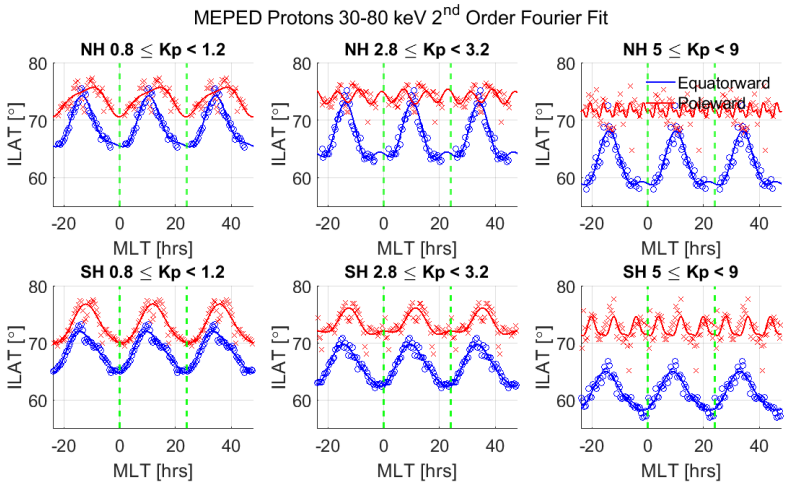

Figure C.4: Fourier series fitted to MEPED proton boundary detection events, for three K_p ranges in the Northern (NH) and Southern (SH) Hemispheres.

C.2 Correlation Figures

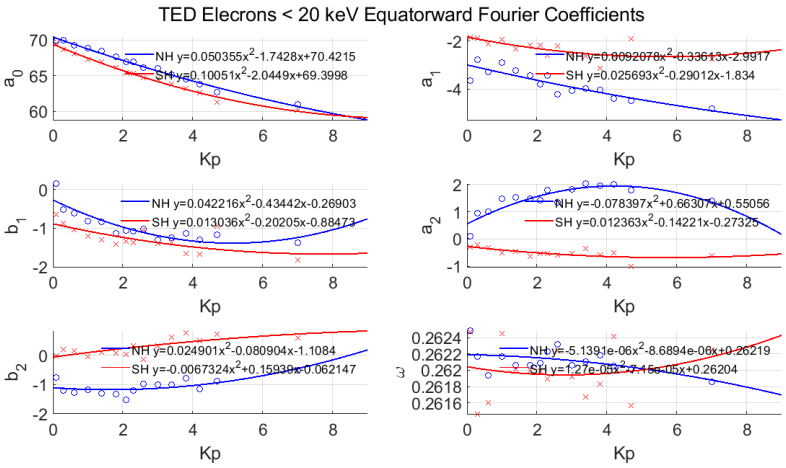

Figure C.5: Second order polynomials correlating the six Fourier series coefficients of the TED electron equatorward boundary to K_p, in both the Northern (NH in blue) and Southern (SH in red) Hemisphere.

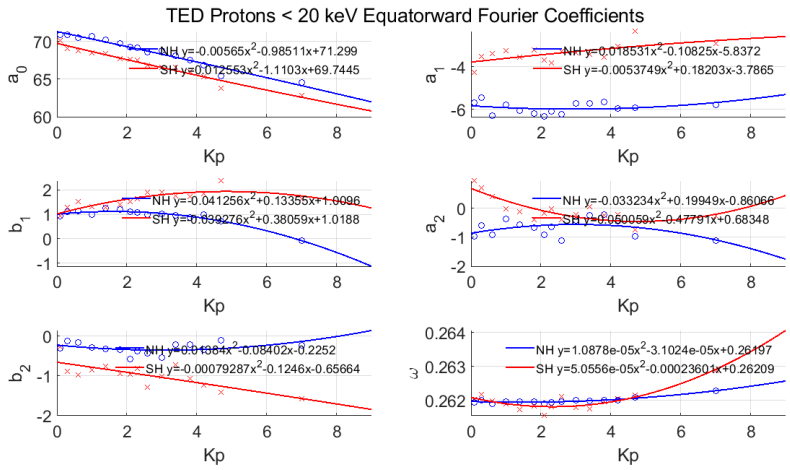

Figure C.6: Second order polynomials correlating the six Fourier series coefficients of the TED proton equatorward boundary to K_p, in both the Northern (NH in blue) and Southern (SH in red) Hemisphere.

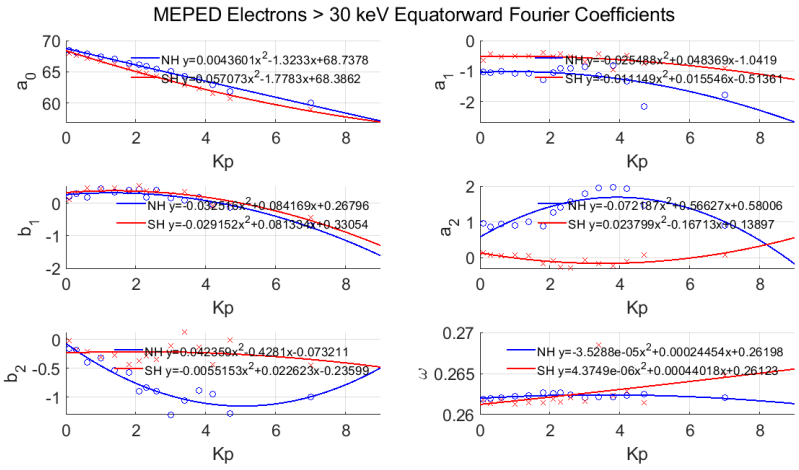

Figure C.7: Second order polynomials correlating the six Fourier series coefficients of the MEPED electron equatorward boundary to K_p, in both the Northern (NH in blue) and Southern (SH in red) Hemisphere.

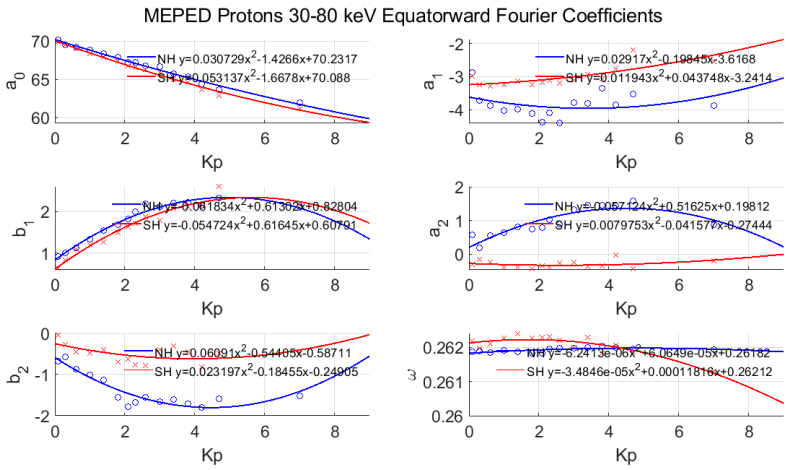

Figure C.8: Second order polynomials correlating the six Fourier series coefficients of the MEPED proton equatorward boundary to K_p, in both the Northern (NH in blue) and Southern (SH in red) Hemisphere.

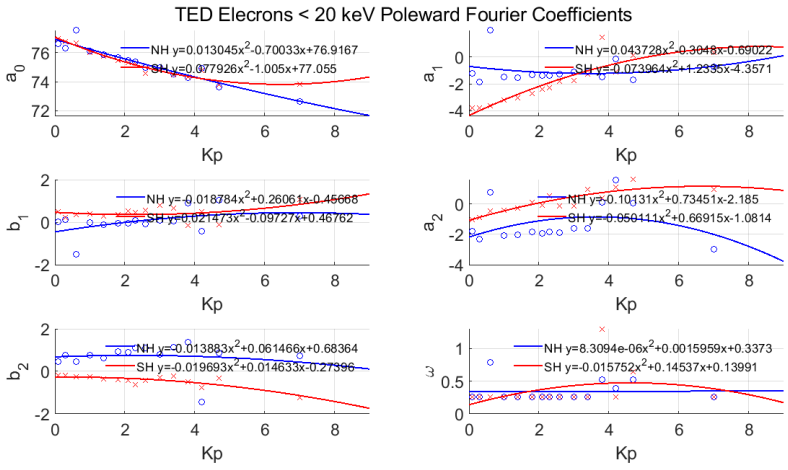

Figure C.9: Second order polynomials correlating the six Fourier series coefficients of the TED electron poleward boundary to K_p, in both the Northern (NH in blue) and Southern (SH in red) Hemisphere.

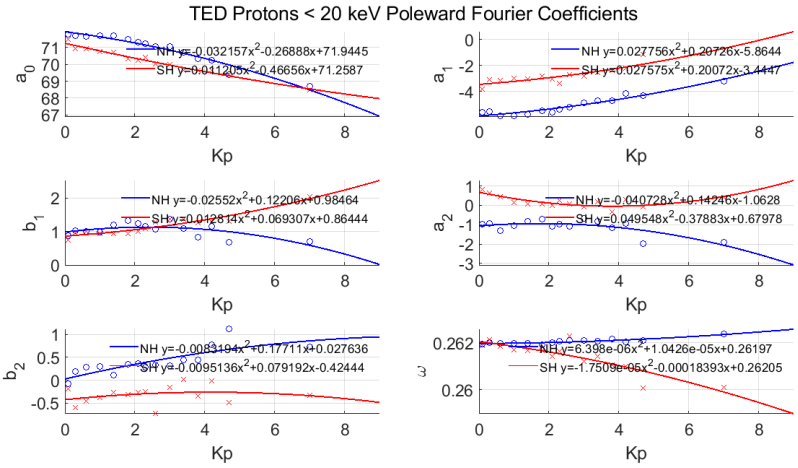

Figure C.10: Second order polynomials correlating the six Fourier series coefficients of the TED proton poleward boundary to K_p, in both the Northern (NH in blue) and Southern (SH in red) Hemisphere.

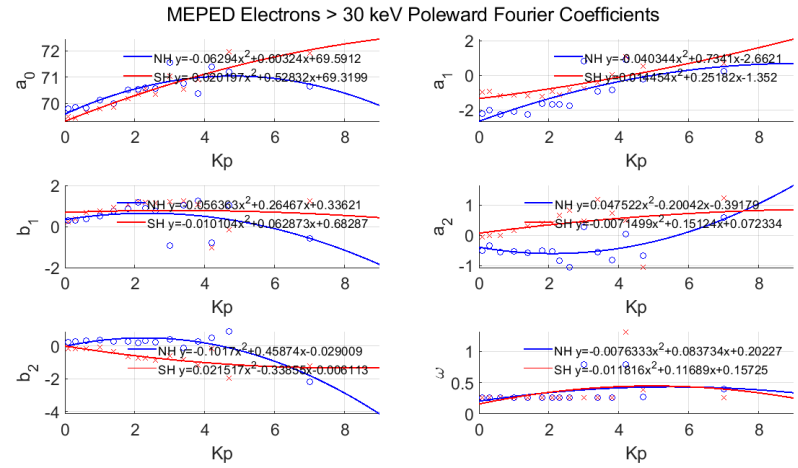

Figure C.11: Second order polynomials correlating the six Fourier series coefficients of the MEPED electron poleward boundary to K_p, in both the Northern (NH in blue) and Southern (SH in red) Hemisphere.

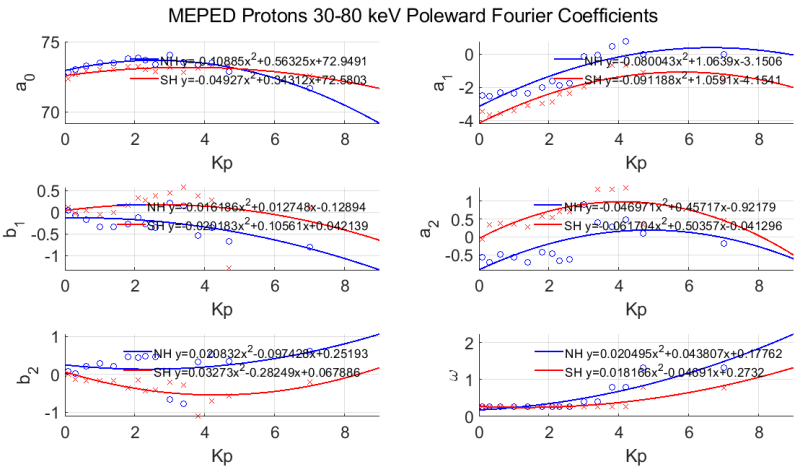

Figure C.12: Second order polynomials correlating the six Fourier series coefficients of the MEPED proton poleward boundary to K_p, in both the Northern (NH in blue) and Southern (SH in red) Hemisphere.

C.3 Deviation from the Feldstein Model

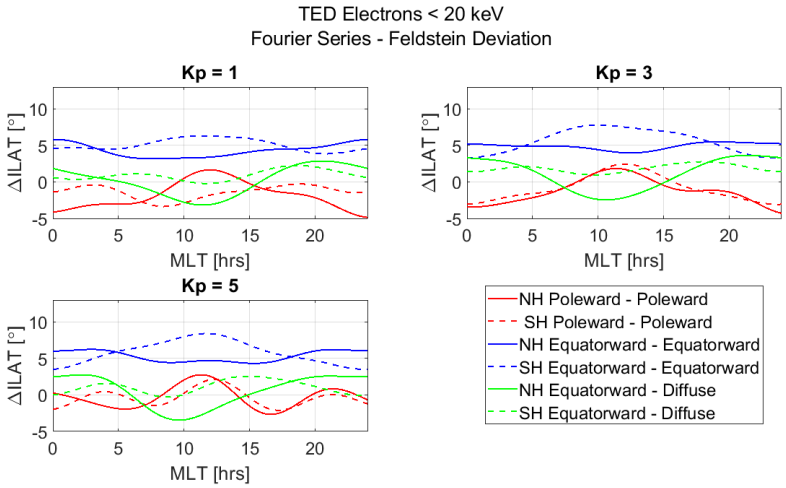

Figure C.13: The difference in ILAT between the TED electron polynomial fit boundaries and the Feldstein boundaries, for: Fourier series poleward and Feldstein poleward (red), Fourier series equatorward and Feldstein equatorward (blue) and Fourier series equatorward and Feldstein diffuse (green). Solid lines represent boundary comparisons in the Northern Hemisphere (NH) and dashed lines indicate comparisons in the Southern Hemisphere (SH).

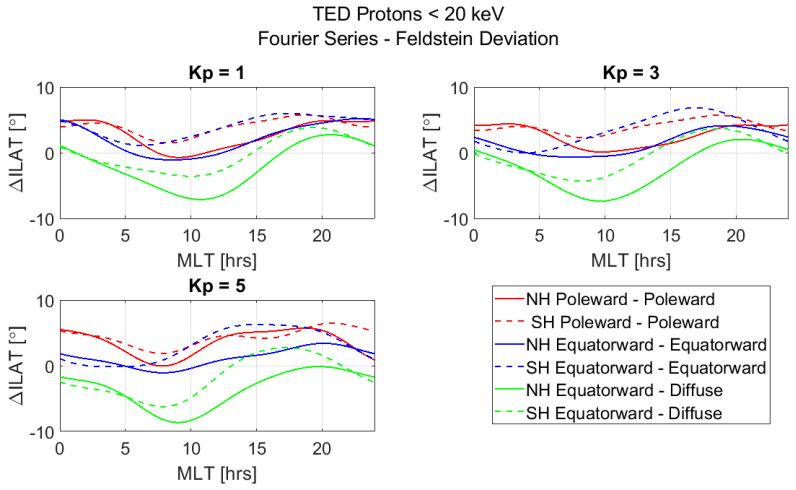

Figure C.14: The difference in ILAT between the TED proton Fourier series fit boundaries and the Feldstein boundaries, for: Fourier series poleward and Feldstein poleward (red), Fourier series equatorward and Feldstein equatorward (blue) and Fourier series equatorward and Feldstein diffuse (green). Solid lines represent boundary comparisons in the Northern Hemisphere (NH) and dashed lines indicate comparisons in the Southern Hemisphere (SH).

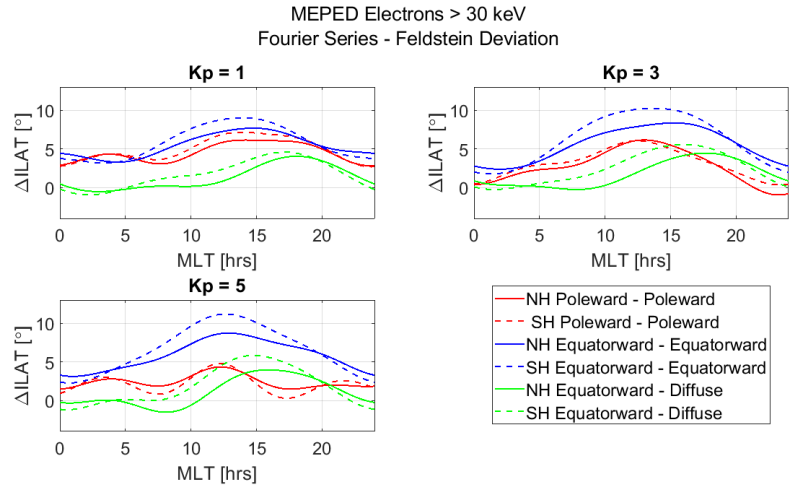

Figure C.15: The difference in ILAT between the MEPED electron Fourier series fit boundaries and the Feldstein boundaries, for: Fourier series poleward and Feldstein poleward (red), Fourier series equatorward and Feldstein equatorward (blue) and Fourier series equatorward and Feldstein diffuse (green). Solid lines represent boundary comparisons in the Northern Hemisphere (NH) and dashed lines indicate comparisons in the Southern Hemisphere (SH).

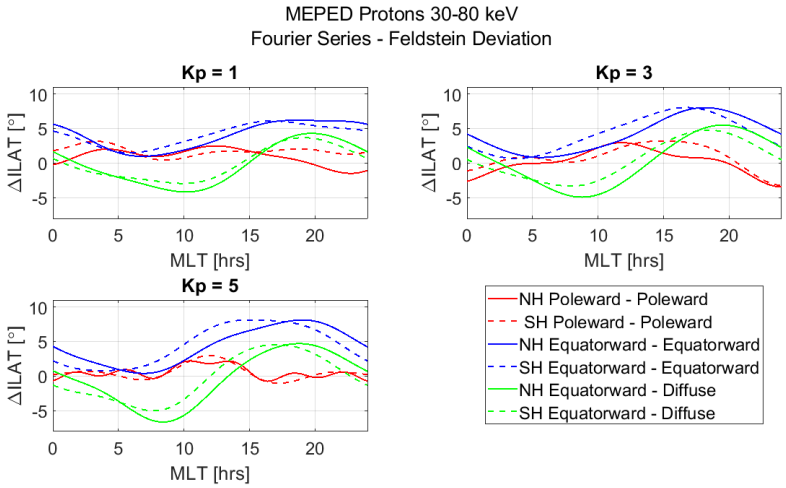

Figure C.16: The difference in ILAT between the MEPED proton Fourier series fit boundaries and the Feldstein boundaries, for: Fourier series poleward and Feldstein poleward (red), Fourier series equatorward and Feldstein equatorward (blue) and Fourier series equatorward and Feldstein diffuse (green). Solid lines represent boundary comparisons in the Northern Hemisphere (NH) and dashed lines indicate comparisons in the Southern Hemisphere (SH).

Bibliography

Akasofu, S. (1968). *Polar and Magnetospheric Substorms*. Springer Netherlands. doi: 10.1007/978-94-010-3461-6

Akasofu, S. (1978). Upper Atmosphere Research in Antarctica. In L. J. Lanzerotti & C. G. Park (Eds.), (Vol. 29, pp. 157–199). 1909 K Street, N. W. Washington, D. C. 20006: American Geophysicsl Union.

Akasofu, S. (1999). Auroral spectra as a tool for detecting extraterrestrial life. *Eos, Transactions American Geophysical Union*, *80*(35), 397. doi: 10.1029/e00801035p00397-01

Alken, P. (2019, December). *International Geomagnetic Reference Field.* Retrieved from `https://www.ngdc.noaa.gov/IAGA/vmod/igrf.html` (Accessed June 3, 2020)

Baker, K. B., & Wing, S. (1989). A new magnetic coordinate system for conjugate studies at high latitudes. *Journal of Geophysical Research*, *94*(A7), 9139. doi: 10.1029/ja094ia07p09139

Bartels, J. (1957a). The geomagnetic measures for the time-variations of solar corpuscular radiation, described for use in correlation studies in other geophysical fields. *Ann. Intern. Geophys. Year 4,*, 227–236.

Bartels, J. (1957b). The technique of scaling indices K and Q of geomagnetic activity. *Ann. Intern. Geophys. Year 4,*, 215–226.

Bartels, J., Heck, N. H., & Johnston, H. F. (1939). The three-hour-range index measuring geomagnetic activity. *Journal of Geophysical Research*, *44*(4), 411. doi: 10.1029/te044i004p00411

Brekke, A. (2013). *Physics of the Upper Polar Atmosphere* (Second ed.). Springer Berlin Heidelberg. Retrieved from `https://www.ebook.de/de/product/17039584/asgeir_brekke_physics_of_the_upper_polar_atmosphere.html`

Carbary, J. F. (2005, oct). A Kp-based model of auroral boundaries. *Space Weather*, *3*(10). doi: 10.1029/2005sw000162

Chen, F. (2015). *Introduction to Plasma Physics and Controlled Fusion*. Springer-Verlag GmbH. Retrieved from `https://www.ebook.de/de/product/24427075/francis_chen_introduction_to_plasma_physics_and_controlled_fusion.html`

Chernov, N. (2020). *Ellipse Fit (Direct method)*. Retrieved from `https://se.mathworks.com/matlabcentral/fileexchange/`

22684-ellipse-fit-direct-method (Accessed June 24, 2020)

Dubyagin, S., Ganushkina, N. Y., & Sergeev, V. (2018, may). Formation of 30 KeV proton isotropic boundaries during geomagnetic storms. *Journal of Geophysical Research: Space Physics*, *123*(5), 3436–3459. doi: 10.1002/2017ja024587

EUMETSAT. (2020). *The Space Environmental Monitor (SEM-2) provides information on solar activity and space weather which may affect the satellites and instruments.* Retrieved from https://www.eumetsat.int/website/home/Satellites/CurrentSatellites/Metop/MetopDesign/SEM/index.html (Accessed June 19, 2020)

Evans, D. S., & Greer, M. S. (2004). Polar orbiting environmental satellite space environment monitor - 2: Instrument descriptions and archive data documentation [Computer software manual]. (NOAA Technical Memorandum)

Feldstein, Y. I. (1964). Auroral morphology, I. The location of the auroral zone. *Tellus*, *16*(2), 252–257.

Feldstein, Y. I., & Starkov, G. V. (1967). Dynamics of auroral belt and polar geomagnetic disturbances. *Planetary and Space Science*, *15*(2), 209–229. doi: 10.1016/0032-0633(67)90190-0

Fitzgibbon, A., Pilu, M., & Fisher, R. (1999, may). Direct least square fitting of ellipses. *IEEE Transactions on Pattern Analysis and Machine Intelligence*, *21*(5), 476–480. doi: 10.1109/34.765658

Fortescue, P., Swinerd, G., & Stark, J. (Eds.). (2011). *Spacecraft Systems Engineering*. Wiley John John Wiley Sons, Ltd. Retrieved from https://www.ebook.de/de/product/14751207/spacecraft_systems_engineering.html

Fritz, H. (1881). *Das Polarlicht*. Leipzig.

Ganushkina, N. Y., Pulkkinen, T. I., Kubyshkina, M. V., Sergeev, V. A., Lvova, E. A., Yahnina, T. A., ... Fritz, T. (2005, jul). Proton isotropy boundaries as measured on mid- and low-altitude satellites. *Annales Geophysicae*, *23*(5), 1839–1847. doi: 10.5194/angeo-23-1839-2005

Hartz, T. R. (1971). Particle precipitation patterns. In B. M. McCormac (Ed.), *The Radiating Atmosphere* (pp. 225–238). Doordrecht: Reidel.

Holzworth, R. H., & Meng, C.-I. (1975). Mathematical representation of the auroral oval. *Geophysical Research Letters*, *2*(9), 377–380. doi: 10.1029/gl002i009p00377

ISGI. (2013). *Geomagnetic Indices.* Retrieved from http://isgi.unistra.fr/geomagnetic_indices.php (Accessed December 14, 2019)

Johnsen, M. G. (2013). Real-time determination and monitoring of the auroral electrojet boundaries. *Journal of Space Weather and Space Climate*, *3*, A28. doi: 10.1051/swsc/2013050

Kivelson, M. G., & Russell, C. T. (1995). *Introduction to Space Physics*. Cambridge University Press. Retrieved from

https://www.amazon.com/Introduction-Physics-Cambridge-Atmospheric-Science/dp/0521451043?SubscriptionId=AKIAIOBINVZYXZQZ2U3A&tag=chimbori05-20&linkCode=xm2&camp=2025&creative=165953&creativeASIN=0521451043

Laundal, K. M., & Østgaard, N. (2009). Asymmetric auroral intensities in the earth's northern and southern hemispheres. *Nature*, *460*(7254), 491–493. doi: 10.1038/nature08154

Laundal, K. M., & Richmond, A. D. (2016). Magnetic Coordinate Systems. *Space Science Reviews*, *206*(1-4), 27–59. doi: 10.1007/s11214-016-0275-y

Matzka, J. (2020). *Indices of Global Geomagnetic Activity.* Retrieved from https://www.gfz-potsdam.de/en/kp-index/ (Accessed June 15, 2020)

McIlwain, C. E. (1961). Coordinates for mapping the distribution of magnetically trapped particles. *Journal of Geophysical Research*, *66*(11), 3681–3691. doi: 10.1029/jz066i011p03681

NASA. (2019). *POES.* Retrieved from https://poes.gsfc.nasa.gov/index.html (Accessed October 29, 2019)

NASA. (2020, March). *OMNIWeb Data Explorer.* Retrieved from https://omniweb.gsfc.nasa.gov/form/dx1.html (Accessed February 18, 2020)

Newell, P. T., Sotirelis, T., Liou, K., Meng, C.-I., & Rich, F. J. (2007). A nearly universal solar wind-magnetosphere coupling function inferred from 10 magnetospheric state variables. *Journal of Geophysical Research: Space Physics*, *112*(A1). doi: 10.1029/2006ja012015

Newell, P. T., Sotirelis, T., & Wing, S. (2009). Diffuse, monoenergetic, and broadband aurora: The global precipitation budget. *Journal of Geophysical Research: Space Physics*, *114*(A9). doi: 10.1029/2009ja014326

NOAA. (2015, June). *POES Decommissioned Satellites.* Retrieved from https://www.ospo.noaa.gov/Operations/POES/decommissioned.html (Accessed June 19, 2020)

NOAA. (2016). *DSCOVR: Deep Space Climate Observatory.* Retrieved from https://www.nesdis.noaa.gov/content/dscovr-deep-space-climate-observatory (Accessed December 15, 2019)

NOAA. (2019, March). *POES Operational Status.* Retrieved from https://www.ospo.noaa.gov/Operations/POES/status.html (Accessed June 19, 2020)

NOAA. (2020). *Polar Operational Environmental Satellites (POES).* Retrieved from https://www.ospo.noaa.gov/Operations/POES/index.html (Accessed June 19, 2020)

NOAA. (2020). *Solar Cycle Progression.* Retrieved from https://www.swpc.noaa.gov/products/solar-cycle-progression (Accessed June 20, 2020)

O'Brien, B. J., Laughlin, C. D., Allen, J. A. V., & Frank, L. A. (1962). Measurements of the intensity and spectrum of electrons at 1000-kilometer altitude and

high latitudes. *Journal of Geophysical Research*, *67*(4), 1209–1225. doi: 10.1029/jz067i004p01209

Richmond, A. D. (1995). Ionospheric Electrodynamics Using Magnetic Apex Coordinates. *Journal of geomagnetism and geoelectricity*, *47*(2), 191–212. doi: 10.5636/jgg.47.191

Sigernes, F. (2016). *Aurora Forecast 3D Quick look guide.* Retrieved from `http://kho.unis.no/Software/AuroraForecast3D/help/Info.html` (Accessed March 1, 2020)

Sigernes, F., Dyrland, M., Brekke, P., Chernouss, S., Lorentzen, D. A., Oksavik, K., & Deehr, C. S. (2011). Two methods to forecast auroral displays. *Journal of Space Weather and Space Climate*, *1*(1), A03. doi: 10.1051/swsc/2011003

Søraas, F., Sandanger, M. I., & Smith-Johnsen, C. (2018). NOAA POES and MetOp particle observations during the 17 March 2013 storm. *Journal of Atmospheric and Solar-Terrestrial Physics*, *177*, 115–124. doi: 10.1016/j.jastp.2017.09.004

Starkov, G. V. (1994a). Mathematical model of the auroral boundaries. *Geomagnetism and Aeronomy*, *34*(3), 331–336.

Starkov, G. V. (1994b). Statistical dependences between the magnetic activity indices. *Geomagnetism and Aeronomy*, *34*(1), 101-103.

Thébault, E., Finlay, C. C., Beggan, C. D., Alken, P., Aubert, J., Barrois, O., ... Zvereva, T. (2015). International geomagnetic reference field: the 12th generation. *Earth, Planets and Space*, *67*(1). doi: 10.1186/s40623-015-0228-9

Thomsen, M. F. (2004). Why Kp is such a good measure of magnetospheric convection. *Space Weather*, *2*(11). doi: 10.1029/2004sw000089

Tohmatsu, T. (1990). *Compendium of aeronomy*. Terra Sci. Publ. Co., Tokyo, Japan. Retrieved from `https://www.ebook.de/de/product/2577116/t_tohmatsu_compendium_of_aeronomy.html`

Vestine, E. H. (1944). The Geographic Incidence of Aurora and Magnetic Disturbance, Northern Hemisphere. *Journal of Geophysical Research*, *49*(2), 77. doi: 10.1029/te049i002p00077

Wagner, D., & Neuhäuser, R. (2019). Variation of the auroral oval size and offset for different magnetic activity levels described by the Kp-index. *Astronomische Nachrichten*. doi: 10.1002/asna.201913601

Weiss, L. A., Reiff, P. H., Hilmer, R. V., Winningham, J. D., & Lu, G. (1992). Mapping the Auroral Oval into the Magnetotail Using Dynamics Explorer Plasma Data. *Journal of geomagnetism and geoelectricity*, *44*(12), 1121–1144. doi: 10.5636/jgg.44.1121

Weisstein, E. W. (2020a). *Ellipse.* Retrieved from `https://mathworld.wolfram.com/Ellipse.html` (Accessed May 18, 2020)

Weisstein, E. W. (2020b). *Least Squares Fitting.* Retrieved from `https://mathworld.wolfram.com/LeastSquaresFitting.html` (Accessed June 2, 2020)

Williams, I. K. (2019, February). *Viewing the Northern Lights: 'It's Almost Like*

Heavenly Visual Music'. Retrieved from https://www.nytimes.com/2019/02/11/travel/northern-lights-tourism-in-sweden.html (Accessed October 30, 2019)

Xiong, C., & Lühr, H. (2014). An empirical model of the auroral oval derived from CHAMP field-aligned current signatures - Part 2. *Annales Geophysicae*, *32*(6), 623–631. doi: 10.5194/angeo-32-623-2014

Xiong, C., Lühr, H., Wang, H., & Johnsen, M. G. (2014). Determining the boundaries of the auroral oval from CHAMP field-aligned current signatures - Part 1. *Annales Geophysicae*, *32*(6), 609–622. doi: 10.5194/angeo-32-609-2014

Zhang, Y., & Paxton, L. J. (2008). An empirical Kp-dependent global auroral model based on TIMED/GUVI FUV data. *Journal of Atmospheric and Solar-Terrestrial Physics*, *70*(8-9), 1231–1242. doi: 10.1016/j.jastp.2008.03.008